Electronic Transport of a 2D Quantum Material WTe_2

Wenjin Zhao

A dissertation
submitted in partial fulfillment of the
requirements for the degree of

Doctor of Philosophy

University of Washington

2020

Reading Committee:
David H. Cobden, Chair
Xiaodong Xu
Andreas Karch

Program Authorized to Offer Degree:
Department of Physics

University of Washington

Abstract

Electronic Transport of a 2D Quantum Material WTe_2

Wenjin Zhao

Chair of the Supervisory Committee:
Professor David H. Cobden
Department of Physics

Quantum materials, such as superconductors, topological insulators, magnets, and Weyl semimetals, are materials whose properties cannot be explained without quantum mechanics. Strong correlation and band topology play very important roles in quantum materials. The study of two-dimensional (2D) quantum materials was triggered by the discovery of graphene, the first atomically thin crystal wherein electrons are confined in a single 2D sheet. In this regime, critical material parameters such as carrier density, electron correlation strength and topology can be modified by electrostatic gate, screening effect and magnetic field, respectively. Moreover, the stacking of different 2D quantum materials enables creation of novel structures which can host new electronic phenomena and realize new device functionalities. All of these make 2D quantum materials a perfect platform to study the physics of strong correlation, magnetism, and topology.

This thesis focuses on electronic properties of a 2D quantum material WTe_2. In the first part, I will discuss the discovery of the first ferroelectric metal in few-layer WTe_2. As WTe_2 is thinned

down to trilayer and bilayer, it exhibits coexistence of ferroelectric and metallic phases. Then, I will discuss the quantum spin Hall (QSH) edge state of a monolayer WTe_2 in three aspects. The spin axis is first established by study of the anisotropy of conductance in an external magnetic field. Then I will show the magnetic proximity effect between the QSH edge and a 2D magnet CrI_3. Finally, I will summarize the experiment of spin current injection into the QSH edge.

Table of Contents

List of Figures

List of Tables

ACKNOWLEDGMENTS

Earning a PhD is always a long journey. It is also a great time to learn from and work with many great individuals. I especially thank my PhD advisor, Prof. David Cobden. He is not only a mentor for my research, but also for my life. I am so impressed by his enthusiasm for physics, serious attitude to experiment and excellent taste of science. He is very kind, encouraging and responsive. Whenever I have a question, I can find him very soon and discuss with him in details. He has great logic and is a master of using a white board to illustrate and simplify the question and find the key to solve it. At the end of the talk, I always use my phone to take a picture of the white board and digest physics behind it for a while. I feel so lucky to work in his lab and learn from him.

I thank Prof. Xiaodong Xu, who gave me lots of advice during my PhD life. Just like Dave, Xiaodong is also a great scientist with enthusiasm and exceptional intuition in physics. We have lots of successful collaboration with his team. Whenever I need to measure a device by optical techniques, I will contact Xiaodong and get a plan very quickly. I really enjoy collaborating with him and his team. One motto he told me is “be more efficient”. I always remember this when I do experiment or write.

I thank Prof. Jiun-Haw Chu. My research is not possible without beautiful WTe_2 crystals from his lab. When I was studying the spin-orbit coupling of monolayer WTe_2, I needed to perform experiments in a cryostat with a vector magnetic field, where only his lab has such a system in the Physics epartment. Dave and I asked him for permission to use his cryostat and he readily agreed and let me use it in the coming week. I greatly enjoy doing measurements in his lab.

I thank my committee members, Prof. Anton Andreev, Prof. Andreas Karch and Prof. Christine Luscombe. They are the most responsible committee members and always respond to me very quickly.

I thank Prof. Dmytro Pesin, Prof. Cenke Xu, Prof. Di Xiao and Prof. Justin Song. I had a great time and learned a lot when I discussed models for quantum spin Hall insulator with them.

I thank Prof. Yongtao Cui and Xiong Huang, who did great scanning microwave impedance microscopy measurements on monolayer WTe_2 devices. I got very useful information from the images they provided.

I would like to thank all lab mates, past and present. I thank Dr. Zaiyao Fei, who is like my big brother, for training me on every detail of experiment, including searching, transferring, electron beam lithography, electron beam evaporation, atomic force microscopy, wire bonding, cryostat maintenance, electronic measurements, and data analysis. I thank Dr. Tauno Palomaki, who told me "do WTe_2 instead of other things" at the beginning of my PhD. I thank Prof. Sanfeng Wu, who taught me what the important things are during PhD. I thank Elliott Runburg, Bosong Sun, Paul Nguyen, Arnab Manna, Joshua Kahn, Han Kyou Choi, Yingqiu Feng, Matthew Adams, Dr. Boris Dzyubenko, Tiancheng Song, Prof. Xinghan Cai, Dr. Ding Zhong, Jiaqi Cai, Dr. Dmitry Ovchinnikov, Dr. Zhong Lin, Dr. Xi Wang, Dr. Qi Zhang, Dr. Yingqi Wang, Nathan Wilson, Bevin Huang, Minhao He, John Cenker, Kyle Hwangbo, Jiayi Zhu, Paul Malinowski, Joshua Mutch, Joshua Sanchez, Qianni Jiang, Yue Shi, Dr. Zhaoyu Liu. Without these people, my life and research would not be fun.

I thank my friends in Seattle. I have had lots of fun with them when we played basketball, computer games, table games and went outdoor for hiking and camping.

I thank my wife and my parents. They are always supporting me with their endless love at anytime and anywhere. I and my wife have had a wonderful life in Seattle. I will definitely miss this enjoying life as a PhD student.

DEDICATION

To my wife Chen Li and my parents Rangyuan Zhao and Zongmin Zhao

Chapter 1. Introduction to 2D electron systems

One of the focuses of condensed matter physics is the behavior of electrons in crystals. In an ideal crystal, atoms are arranged periodically; in other words, it has a long-range order. The behavior of a single electron in some periodic lattice potential then can be solved analytically, which is called band theory. By comparison with experimental results, both deeper understanding of physics and development of technology are achieved. The behavior of electrons also depends strongly on the dimensionality. When the movement of electrons is frozen in one dimension and free in another two dimensions, more interesting phenomena appear. For example, the quantum Hall effect (QHE) which was discovered in 1980 requires electrons to move in a two-dimensional plane. Such new phenomena require consideration of more effects, such as topology and electron-electron interaction, which attract both theoretical and experimental research in the two-dimensional electron systems. The successful exfoliation of graphene from bulk graphite in 2004 (*1*) drew renewed attention to layered materials as a platform to study two-dimensional physics.

In this chapter, I will review the conventional 2D electronic systems and layered two-dimensional materials. At last, the topology in quantum mechanics is covered.

1.1 Conventional 2D electronic systems

A two-dimensional electron gas (2DEG) is a model to describe electrons which are free to move in two dimensions, but strongly confined in the third dimension. Due to quantum mechanics, the confinement in the third dimension produces a series of quantized energy levels. Electrons stay in

ground state of this direction. So, electron motion is frozen in the third direction, while it is free in the 2D sheet.

The metal-oxide-semiconductor field-effect transistor (MOSFET) and high-electron-mobility transistor (HEMT) are two technologically important realizations of 2DEG. The schematic structure of a MOSFET is shown in the Fig. 1.1a. When the semiconductor is grounded and a gate voltage V_g is applied on the metal layer, charges will accumulate on the surface of the semiconductor. For a p-type semiconductor, the transistor can be in inversion mode when a positive V_g is applied. As shown in Fig. 1.1b, a positive electric field from the gate can bend the band down. When the conduction band minimum E_c is lower than the Fermi energy E_F near the oxide insulator and semiconductor interface, electrons start to accumulate and form 2DEG.

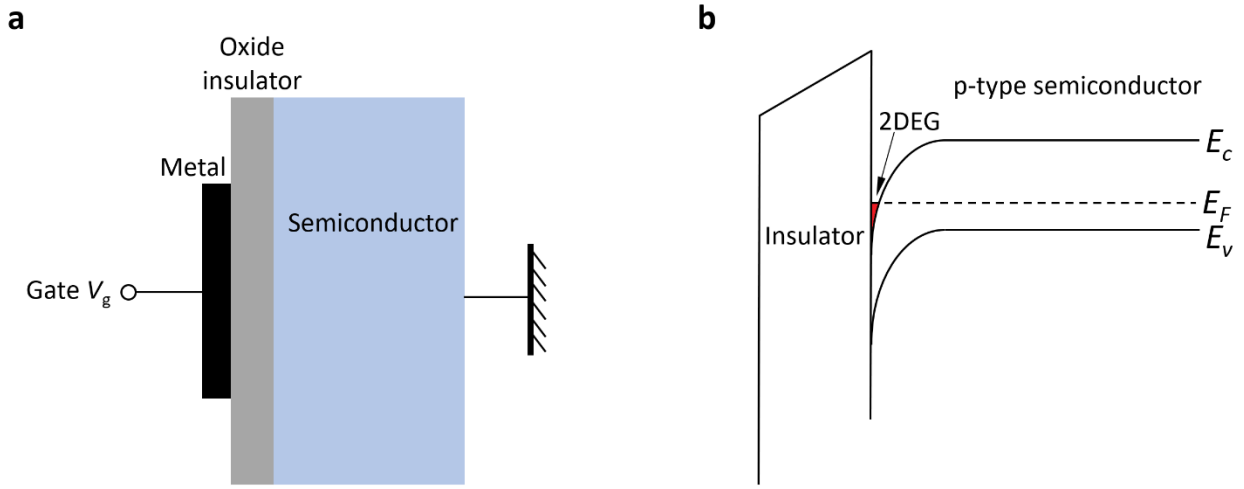

Figure 1.1. 2DEG in MOSFET. **a**, Cross section of a MOSFET. **b**, Band diagram of p-type semiconductor in inversion mode with positive V_g. The red area shows the formation of 2DEG.

In the second case (HEMT), one example is the GaAs/AlGaAs heterostructure, in which GaAs is left undoped and AlGaAs is n-type doped. The band gap of GaAs is narrower than AlGaAs as shown in Fig 1.2b. When the E_F in the AlGaAs is doped higher than the GaAs, charges are transferred to form a PN junction barrier. Because the electron affinities of the two semiconductors

are different, the band is discontinuous at the interface, a spike appears on one side of the barrier and a valley appears on the other side. The electrons at the GaAs surface are confined in a narrow well and then form 2DEG which moves freely at the GaAs surface. The carrier concentration of 2DEG for HEMT typically ranges from $2 \times 10^{11}/\mathrm{cm}^2$ to $2 \times 10^{12}/\mathrm{cm}^2$. Due to separation of electrons and donors, the scattering of electrons by ionized impurities is greatly reduced, so that the mobility of carriers is much improved at low temperature.

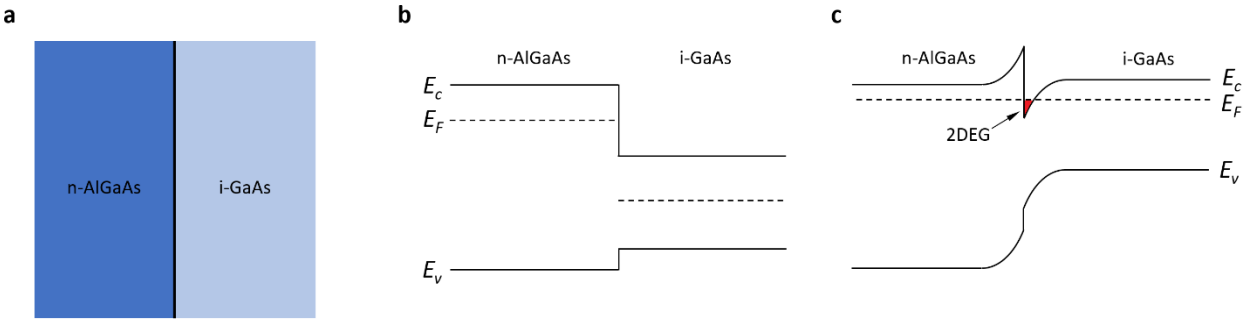

Figure 1.2. Band diagrams of HEMT. **a**, Cross-section view of n-type AlGaAs and intrinsic GaAs heterostructure. **b** and **c**, Band diagram at the junction, (**b**) before and (**c**) after charge transfer has taken place. The red area shows the formation of 2DEG.

1.2 Graphene: the simplest 2D crystal

The discovery of graphene introduced new, accessible ways to study and utilize 2D electronic systems. Graphene is a 2D material made of a single layer of carbon atoms. In 2004, graphene was first successfully isolated, using micromechanical exfoliation onto a SiO_2 substrate (*1*). Later, both integer QHE (*2*, *3*) and fractional QHE (*4*) have been observed in graphene, which shows graphene is a fantastic platform to study 2DEG.

The carbon atoms in graphene are arranged in a honeycomb lattice (*5*, *6*), as depicted in Fig. 1.3a. A unit cell contains two carbon atoms labeled as A and B sublattices. Each sublattice

forms a trigonal lattice. If we choose a (≈ 1.42 Å) as the distance between nearest neighbors, the primitive lattice vectors are

$$\begin{cases} \boldsymbol{a_1} = \frac{a}{2}(3, \sqrt{3}) \\ \boldsymbol{a_2} = \frac{a}{2}(3, -\sqrt{3}) \end{cases} \quad (1)$$

and the reciprocal lattice vectors are

$$\begin{cases} \boldsymbol{b_1} = \frac{2\pi}{3a}(1, \sqrt{3}) \\ \boldsymbol{b_2} = \frac{2\pi}{3a}(1, -\sqrt{3}) \end{cases} \quad (2)$$

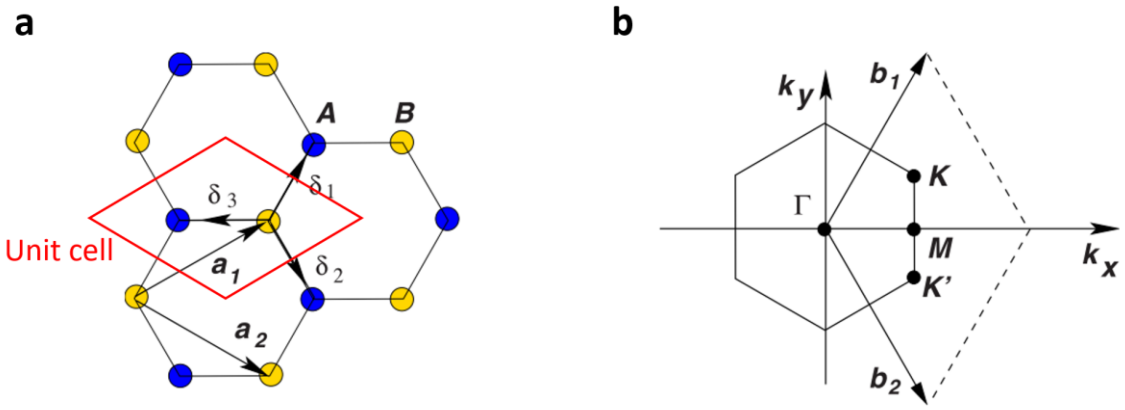

Figure 1.3. Graphene lattice and reciprocal lattice. **a**, Honeycomb lattice structure of graphene. Blue/yellow circles represent the A/B sublattices. $\boldsymbol{a_1}$ and $\boldsymbol{a_2}$ are the primitive lattice vectors. $\boldsymbol{\delta_1}$, $\boldsymbol{\delta_2}$ and $\boldsymbol{\delta_3}$ are the nearest-neighbor vectors. The unit cell is drawn by red rhombus. **b**, Hexagonal first Brillouin zone of graphene. $\boldsymbol{b_1}$ and $\boldsymbol{b_2}$ are the reciprocal lattice vectors. (Figure taken from Ref. (5))

Tight-binding model is a good approximate method to describe the behavior of low energy physics of electrons. For the simplest tight-binding model, only the nearest neighbor hopping is considered. $A(\boldsymbol{R})$ and $B(\boldsymbol{R})$ are the annihilation operators of an electron centered around sublattice A and B. The tight-binding Hamiltonian can be written as

$$H = -t\sum_{\boldsymbol{R},\boldsymbol{R}'} A^{\dagger}(\boldsymbol{R})B(\boldsymbol{R}') + h.c. = -t\sum_{\boldsymbol{R},\boldsymbol{\delta}} A^{\dagger}(\boldsymbol{R})B(\boldsymbol{R}+\boldsymbol{\delta}) + h.c. \tag{3}$$

where t is the nearest hopping energy.

To diagonalize the Hamiltonian, we can go Fourier space (momentum space) (*6*):

$$\begin{cases} A(\boldsymbol{R}) = \dfrac{1}{\sqrt{N}}\displaystyle\sum_{\boldsymbol{k}\in BZ} A(k)e^{i\boldsymbol{k}\cdot\boldsymbol{R}} \\ B(\boldsymbol{R}) = \dfrac{1}{\sqrt{N}}\displaystyle\sum_{\boldsymbol{k}\in BZ} B(k)e^{i\boldsymbol{k}\cdot\boldsymbol{R}} \end{cases} \tag{4}$$

Then, we can rewrite Hamiltonian as

$$H = -t\sum_{\boldsymbol{k},\boldsymbol{\delta}} e^{i\boldsymbol{k}\cdot\boldsymbol{\delta}}A^{\dagger}(\boldsymbol{k})B(\boldsymbol{k}) + h.c. = \sum_{\boldsymbol{k}} \varphi^{\dagger}(\boldsymbol{k})h(\boldsymbol{k})\varphi(\boldsymbol{k}) \tag{5}$$

where $\varphi(\boldsymbol{k}) = (A(\boldsymbol{k}), B(\boldsymbol{k}))^T$ and Bloch Hamiltonian $h(\boldsymbol{k}) = \begin{pmatrix} 0 & f(\boldsymbol{k}) \\ f^*(\boldsymbol{k}) & 0 \end{pmatrix}$ with

$$f(\boldsymbol{k}) = -t\sum_{\boldsymbol{\delta}} e^{i\boldsymbol{k}\cdot\boldsymbol{\delta}} = -t(e^{-ik_x a} + 2e^{\frac{ik_x a}{2}}\cos\left(\frac{k_y a\sqrt{3}}{2}\right)) \tag{6}$$

$A(\boldsymbol{k})$ and $B(\boldsymbol{k})$ are the annihilation operators of an electron centered around sublattice A and B with momentum $\boldsymbol{k}$. The eigenenergies of the tight-binding Hamiltonian are the eigenvalues of the Bloch Hamiltonian, which are

$$\varepsilon_{\pm}(\boldsymbol{k}) = \pm t\sqrt{3 + 2\cos\left(\sqrt{3}k_y a\right) + 4\cos\left(\frac{\sqrt{3}k_y a}{2}\right)\cos\left(\frac{3k_x a}{2}\right)} \tag{7}$$

After consideration of the second-nearest hoping, the band shifts a value as function of $\boldsymbol{k}$. But the gap size is not changed by the second-nearest hoping (*5*). The band diagram is plotted in Fig. 1.4. The band gap is zero at the six corners of the first Brillouin zone, which are conventionally labeled the K- and K'-points.

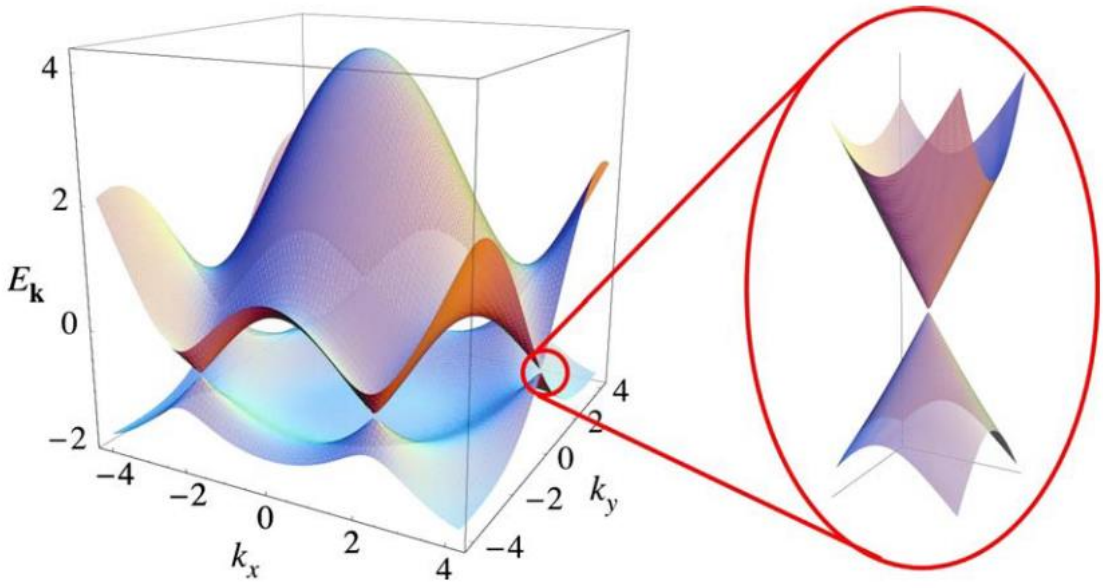

Figure 1.4. Band diagram of single layer graphene. The band gap is zero at the six corners of the first Brillouin zone as shown on left. The linear dispersion near the Dirac point is shown on the right. (Figure taken from Ref. (*5*))

$f(\boldsymbol{k})$ can be expanded around these points. Around K', for example, we can get

$$h(\boldsymbol{K}' + \boldsymbol{q}) \approx -\frac{3ta}{2}\begin{pmatrix} 0 & e^{-\frac{2\pi i}{3}}(q_y + iq_x) \\ e^{\frac{2\pi i}{3}}(q_y - iq_x) & 0 \end{pmatrix} \tag{8}$$

Upon changing the phases of wavefunctions centered at A and B sublattices, the Bloch Hamiltonian takes the now-famous linear form,

$$h(\boldsymbol{K}' + \boldsymbol{q}) = \hbar v_F \boldsymbol{q} \cdot \boldsymbol{\sigma} \tag{9}$$

where $\boldsymbol{\sigma}$ is the vector of Pauli-matrices for sublattice and $v_F = \frac{3ta}{2\hbar}$. $\sigma_z = \pm 1$ describes states on the $A(B)$ sublattice. This dispersion is the massless Dirac dispersion, and so these points ($\boldsymbol{q} = 0$) are known as the Dirac points of graphene.

1.3 Layered 2D materials

Graphene is mechanically exfoliated from layered graphite using Scotch tape. Following the same procedure, more and more 2D materials have been obtained and studied. The properties of 2D materials spread over a broad range including semimetal (graphene, etc.), semiconductor (WSe_2, etc.), insulator (hBN, etc.), charge density wave material (TaS_2, etc.), magnet (CrI_3, etc.) and superconductor ($NbSe_2$, etc.). Perhaps the greatest advantage of 2D materials is that the doping level can be adjusted by a local gate voltage as the electric field penetration length through an atomically thin sample is longer than its thickness. That makes for a rich phase diagram which can be accessed by varying gate voltage, magnetic field, and temperature in a single device. A second advantage is the ability to stack the layers of different 2D materials into heterostructures with perfect interfaces, even when the lattices match poorly. Proximity effect could be realized by putting two different 2D materials together. A third advantage is that strong correlated physics can emerge in twisted double layers, wherein a Moiré superpotential can be formed by twisting two layers of matching lattice constants by a small angle. For example, both correlated insulating states and an unconventional superconductivity have been observed in twisted bilayer graphene (*7*, *8*).

1.4 Concept of topology in quantum mechanics

Symmetry and topology are two fundamental properties of crystals. Symmetry describes operations under which that the crystal is not changed, such as time reversal, inversion, rotation, and mirror reflection. In mathematics, topology describes properties that change stepwise. For electrons in crystals, topological order is encoded in the electronic bands. Some functions of the band are not changed by a continuous deformation. For example, as shown in Fig. 1.5, the topological order of a sphere is the same with that of a bowl. From a bowl to a cup, topological

order is different since a hole needs to be created. The number of holes in a solid can be the index for its topological order. Note that the number of holes can only be integers and changes stepwise.

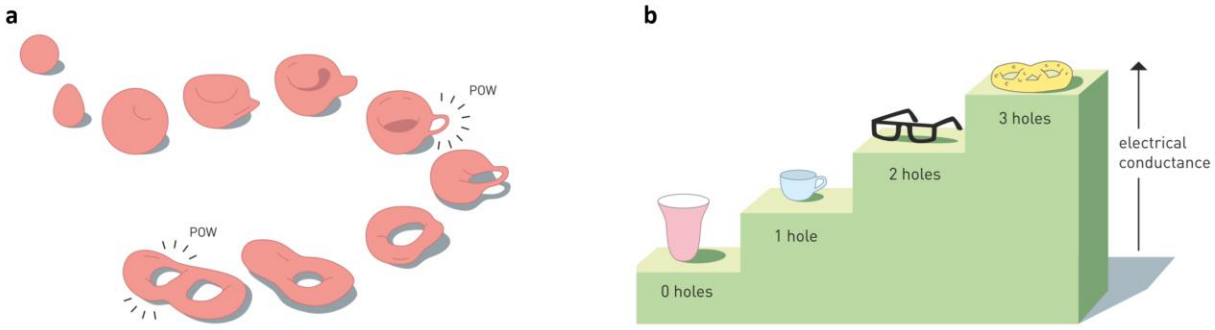

Figure 1.5. Topology order classified by number of holes. **a**, Topological order changed by creating a hole. **b**, Solids categorized by number of holes as topological index. (Figure taken from Ref. (*9*))

The study of topology of bands in condensed matter physics started from interpretation of quantum Hall effect (QHE) (*10–12*). Here, we discuss those concepts in a simple way as shown in Ref. (*13*). In band theory, an insulator can be described by Bloch Hamiltonian $H(\boldsymbol{k})$ where k is the crystal momentum. The eigenstate can be solved from Bloch equation,

$$H(\boldsymbol{k})|u_n(\boldsymbol{k})\rangle = E_n(\boldsymbol{k})|u_n(\boldsymbol{k})\rangle \tag{10}$$

The Berry connection is defined by

$$A^{(n)}(\boldsymbol{k}) = i\langle u_n(\boldsymbol{k})|\partial_{\boldsymbol{k}} u_n(\boldsymbol{k})\rangle \tag{11}$$

where $|u_n(\boldsymbol{k})\rangle$ has a gauge degree of freedom. Under gauge transformation,

$$|u_n(\boldsymbol{k})\rangle \rightarrow e^{i\,\phi_n(\boldsymbol{k})}|u_n(\boldsymbol{k})\rangle \tag{12}$$

$$A^{(n)}(\boldsymbol{k}) \rightarrow A^{(n)}(\boldsymbol{k}) - \partial_{\boldsymbol{k}}\,\phi_n(\boldsymbol{k}) \tag{13}$$

Any physical quantity should be gauge invariant so we need to construct other variables from the Berry connection. One of them is the Berry curvature which is the field strength of Berry connection defined by

$$F_{ij}^{(n)}(\boldsymbol{k}) = \partial_{k_i} A_{k_j}^{(n)}(\boldsymbol{k}) - \partial_{k_j} A_{k_i}^{(n)}(\boldsymbol{k}) \tag{14}$$

Another variable is the Berry phase defined by

$$\gamma_n = i \oint_c d\boldsymbol{k} \cdot \boldsymbol{A}^{(n)}(\boldsymbol{k}) \tag{15}$$

where c is a closed path in momentum space.

For a 2D system, the Brillouin zone is also extended in two dimensions. The total Chern number is defined as

$$Ch = \sum_{E_n<E_F} Ch^{(n)} = \frac{1}{2\pi} \sum_{E_n<E_F} \int_{2dBZ} dk_x dk_y F_{ij}^{(n)}(\boldsymbol{k}) \tag{16}$$

Chern number must be an integer and can categorize crystals into different topological orders.

A special case is a system with time-reversal symmetry. Under time-reversal operation, Berry connection and Berry curvature are transformed in the following way,

$$\begin{cases} \sum_{E_n<E_F} A^{(n)}(\boldsymbol{k}) \to \sum_{E_n<E_F} A^{(n)}(-\boldsymbol{k}) \\ \sum_{E_n<E_F} F_{ij}^{(n)}(\boldsymbol{k}) \to -\sum_{E_n<E_F} F_{ij}^{(n)}(-\boldsymbol{k}) \end{cases} \tag{17}$$

Therefore, for a system with time-reversal symmetry,

$$Ch = \frac{1}{2\pi} \int_{2dBZ} dk_x dk_y \sum_{E_n<E_F} F_{ij}^{(n)}(\boldsymbol{k}) \tag{18}$$

$$= -\frac{1}{2\pi} \int_{2dBZ} dk_x dk_y \sum_{E_n<E_F} F_{ij}^{(n)}(-\boldsymbol{k}) = -Ch$$

which leads to $Ch = 0$. Hence, another topological index is needed to classify the topological class in time-reversal symmetric systems. First, let us see the property of the time reversal operator T for spin $-\frac{1}{2}$ electrons. T obeys

$$T^2 = -1 \tag{19}$$

and the anti-unitarity of T yields

$$\langle Tu|Tv\rangle = \langle v|u\rangle \tag{20}$$

Then, let us examine the inner product of $|u\rangle$ and $T|u\rangle$,

$$\langle u|Tu\rangle = \langle TTu|Tu\rangle = -\langle u|Tu\rangle \tag{21}$$

which means $|u\rangle$ and $T|u\rangle$ are orthogonal and have the same energy in time-reversal symmetric systems. We call this a Kramers degeneracy and $|u\rangle$ and $T|u\rangle$ as a Kramers pair. In general, we can relabel the band indices of the Kramers pair by $|u_n^{\mathrm{I}}(\boldsymbol{k})\rangle$ and $|u_n^{\mathrm{II}}(\boldsymbol{k})\rangle$, which are related by

$$|u_n^{II}(\boldsymbol{k})\rangle = e^{i\,\phi_n(\boldsymbol{k})} T|u_n^{I}(-\boldsymbol{k})\rangle \tag{22}$$

In a general 2D time-reversal symmetric system, we can use Kramers pairs to divide the Hilbert space into two subspaces. Then the Chern number of each subspace can be defined as

$$\begin{cases} Ch_I = \dfrac{1}{2\pi}\displaystyle\int_{2dBZ} dk_x dk_y F_{ij}^{I(-)}(\boldsymbol{k}) \\ Ch_{II} = \dfrac{1}{2\pi}\displaystyle\int_{2dBZ} dk_x dk_y F_{ij}^{II(-)}(\boldsymbol{k}) \end{cases} \tag{23}$$

Even though $Ch_{\mathrm{I}} + Ch_{\mathrm{II}} = 0$, the parity of Ch_{I} and Ch_{II} must be same and gauge invariant. A new topological index Z_2 (ν_{2d}) is introduced (*14*, *15*) as

$$(-1)^{\nu_{2d}} \equiv (-1)^{Ch_I} = (-1)^{Ch_{II}} \tag{24}$$

By this Z_2 classification, a topological trivial state such as vacuum with $\nu_{2d} = 0$ is distinct from a topological nontrivial state with $\nu_{2d} = 1$, which is called two dimensional topological insulator.

1.5 The focus of this thesis

This thesis focuses on the electronic properties of one of the layered transition metal dichalcogenides: tungsten ditelluride (WTe_2). The quantum behavior of WTe_2 varies significantly with its thickness. Bulk WTe_2 as a Weyl semimetal exhibits an extremely non-saturating magnetoresistance which is related to the nearly balanced electron and hole densities (*16*, *17*). When WTe_2 is thinned down to a few layers, it possesses low symmetry and thus provides a new platform to study the spin-torque effect when in contact with Permalloy (*18*). Moreover, the nonlinear anomalous Hall effect was also observed in few-layer WTe_2, related to a nonzero Berry curvature dipole (*19, 20*). When WTe_2 is thinned down further to trilayer and bilayer, ferroelectric switching coexists with its metallic phase, making it the first ferroelectric metal (*21*). More dramatic changes happen when WTe_2 is thinned down to the monolayer limit. It is the only monolayer 2D topological insulator to date, possessing helical edge states at low doping levels (*22–24*). The helical edge states can be proximitized by a 2D magnet and show nonreciprocal quantum magneto-transport (*25*). Furthermore, monolayer WTe_2 is a superconductor at mild electron doping below 1 K (*26*, *27*). In summary, topological semimetal WTe_2 hosts rich phases and physics phenomena.

Chapter 2. Ferroelectric switching of a two-dimensional metal

2.1 Ferroelectricity and metallicity

The structure of a polar material contains a special axis, which is called its polar axis. The physical property, such as electric polarization, of it can be distinguished along the two directions of its polar axis. This is necessary for the existence of a spontaneous electric polarization, which is a vector quantity. Ten of the thirty-two three-dimensional crystal classes have a polar axis, and can be called the pyroelectric classes, because polarization is changed along this axis by heating. A ferroelectric material has a built-in polarization whose direction can be changed by applying an electric field along the polar axis. The relationship between the displacement field $\boldsymbol{D}$ and the electric field $\boldsymbol{E}$ is hysteretic, due to this switch-ability of the spontaneous polarization. This also makes it possible to engineer ferroelectric memory, cheap room-temperature magnetic-field detectors and piezoelectric nanotubes (*28, 29*).

A metal is a material that conducts electricity well by free charge carriers. When the temperature decreases, the resistance of a metal should also decrease due to suppression of phonon scattering. Back to 1965, Anderson and Blount introduced the term ferroelectric metal, referring to the possibility of a phase transition from a nonpolar to a polar structure in certain metallic crystals (*30*), now referred to as polar metals. However, it was naturally assumed that, due to screening, there would be no net electric polarization and hence no pyroelectric effect, and that the polar vector would not be switchable, contrary to the normal definition of a ferroelectric. The first convincing examples of polar metals have just recently been identified (*31–34*).

2.2 Sample fabrication process

To make monolayer or few-layer WTe_2 devices, a standard exfoliation and fabrication process were taken with care. Very high quality bulk single crystals of WTe_2 were grown by the tellurium flux method (*35*). The schematic device fabrication process is shown in Fig. 2.1a. The top part (stamp/graphite/hexagonal boron nitride (hBN)/WTe_2) and bottom part (Pt/hBN/graphite/SiO_2/Si) were prepared separately. For the bottom part, a stamp with PC/PDMS on glass slide was made first (*36*, *37*). A piece of hBN was transferred on top of a graphite by the stamp, with the PC/hBN melted down on top of the graphite by heating the stamp up to 180 ℃. The stack was usually stored overnight before removing the PC by placing the entire substrate in a chloroform bath for at least 6 hours followed by another 2-hour long chloroform bath. The hBN/graphite stack was then annealed in a 95%Ar/5%H_2 atmosphere at 400 ℃ for 2 hours. Next, double resists PMMA-495/PMMA-950 were spin-coated on the stack followed by standard electron beam lithography to define the contact geometry. After that, Pt contacts were deposited by an electron beam evaporator. The thickness of Pt contact is about 6 nm, which is thick enough to be a good metal and not too thick to apply too much strain for 2D materials on it. After dissolving PMMA in an acetone bath at room temperature, to clean the surface of hBN and eliminate spikes on the Pt contacts, a half hour of dichloromethane bath was taken. At last, a one-hour anneal for the bottom part at 200℃ was taken. For the top part, another PC/PDMS stamp was made first. A piece of graphite and hBN were picked up. Since atomically thin WTe_2 is very sensitive to air, searching and transferring for WTe_2 were performed in a glove box with both O_2 and $H_2O < 0.5$ ppm. After identification of WTe_2 by optical contrast, it was picked up by the top graphite/hBN and melted down on the Pt contacts of the bottom part. The whole stack was stored overnight, and then the PC was cleaned by a chloroform bath. Another step of electron beam lithography and evaporation of 60/6nm Au/V

were done to define electrical bonding pads. An optical image was taken as shown in Fig 2.1b. The device is scanned by atomic force microscopy (AFM) as shown in Fig 2.1c. The top boundary of WTe_2 can be clearly seen. The white areas are bubbles formed during the transfer processes.

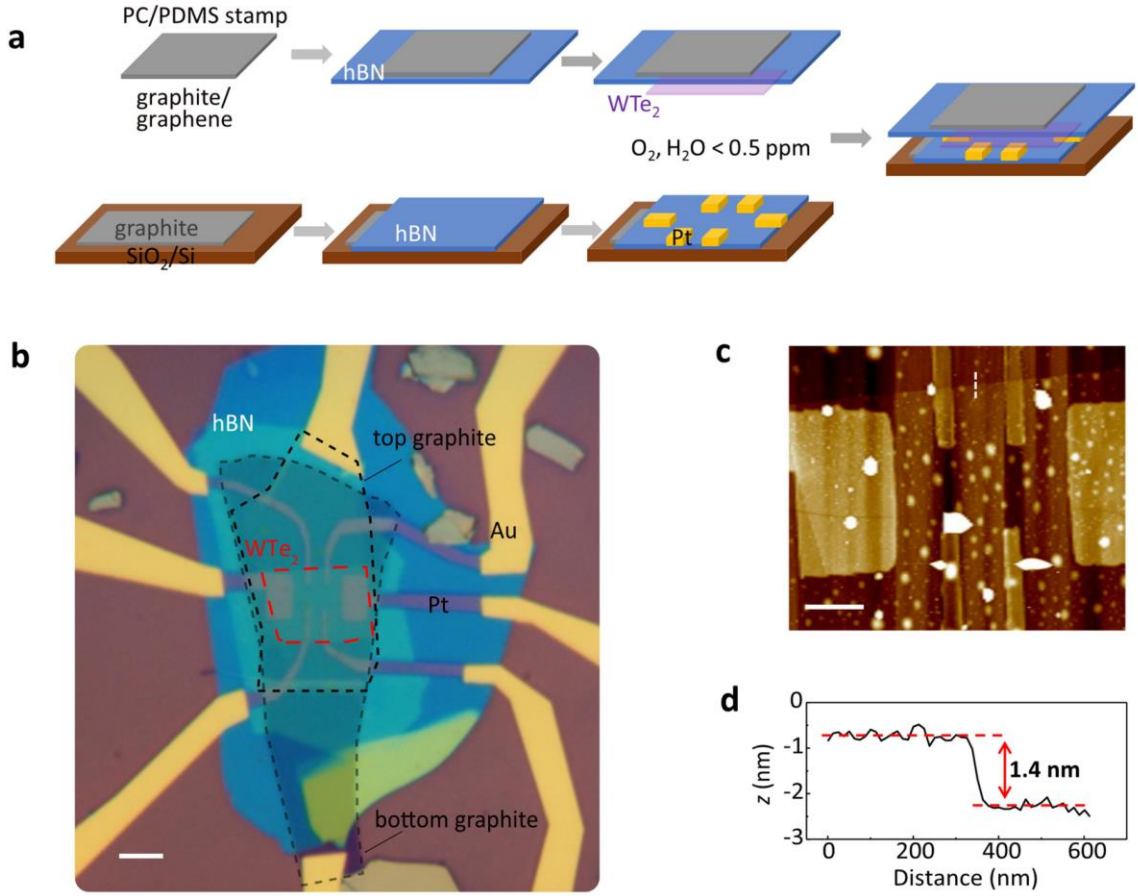

Figure 2.1. Fabrication processes. **a**, Schematic processes. **b**, Optical image to a dual-gated WTe_2 device. Boundaries of graphite and WTe_2 are drawn as black and red dashed lines, respectively. Scale bar, 5μm. **c**, AFM topology image of the center region in **b**. Scale bar, 2μm. **d**, Line cut along dashed write line in **c**. (Figure taken from Ref. (*21*))

For all devices included in this thesis, the device fabrication process is similar as described above. Devices could have a silicon gate instead of a graphite gate or have only one bottom gate. WTe_2 encapsulated by two pieces of hBN can be mono-, bi-, tri-layer. Another 2D material, such

as CrI_3, can be inserted on top of WTe_2 to study the magnetic proximity effect. The thickness of WTe_2 and hBN of devices used in this chapter are listed in table 2.1.

Device label	WTe_2	Top hBN (nm)	Bottom hBN (nm)
MW1	Monolayer	6	28
BW2	Bilayer	8	25
BW3	Bilayer	NA	24
BW5	Bilayer	12	20
BW6	Bilayer	16	18
TW1	Trilayer	5.5	23

Table 2.1. Thickness of WTe_2 and hBN dielectrics for devices.

2.3 Ferroelectric switching in WTe_2

The three-dimensional $1T' - WTe_2$ stacks in T_d order, which is orthorhombic and has a polar space group $Pmn2_1$ (*34*). It remains metallic down to three layers when undoped (*38*), or to a monolayer when electrostatically doped (*22*). I will show that in this limit it constitutes the first ferroelectric metal, with interesting consequences.

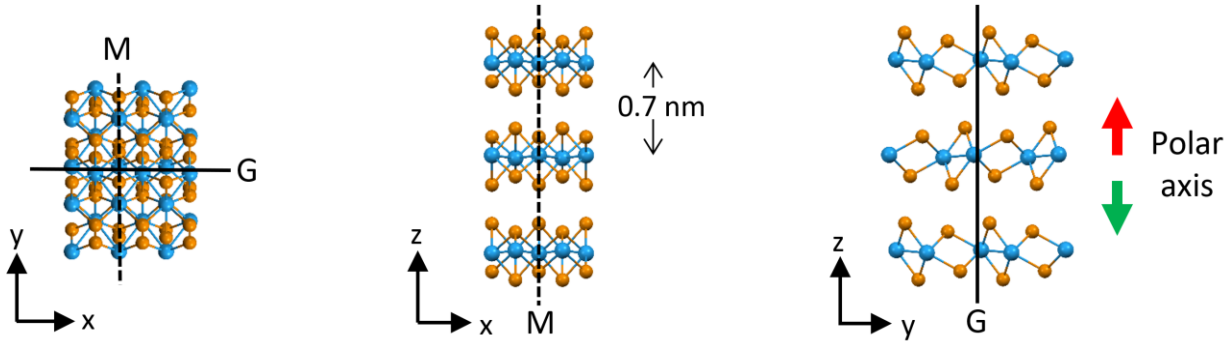

Figure 2.2. Crystal structure and symmetries of T_d WTe_2. M and G are (y-z) mirror plane and (x-z) glide plane, respectively. Orange balls, Te atoms; blue balls, W atoms. Polar axis is shown by a green or red arrow.

As shown in Fig. 2.2, the 1T′ structure with T_d stacking contains a y-z mirror (M) plane and an x-z glide plane. Because a polar axis must be parallel to two symmetry planes, the only allowed axis is the z-axis which is perpendicular to the layers (*34*). An electric field along the polar axis can be applied by using the device geometry indicated in Fig. 2.3. A thin WTe_2 flake contacted by Pt electrodes is sandwiched between two hBN dielectric sheets, with the thickness d_t (top hBN) and d_b (bottom hBN). Above and below the hBN are gate electrodes, to which gate voltages V_t and V_b can be applied. We define the average electric flux density passing upwards through the WTe_2 flake when it is grounded by

$$E_\perp = (-V_t/d_t + V_b/d_b)/2 \qquad (25)$$

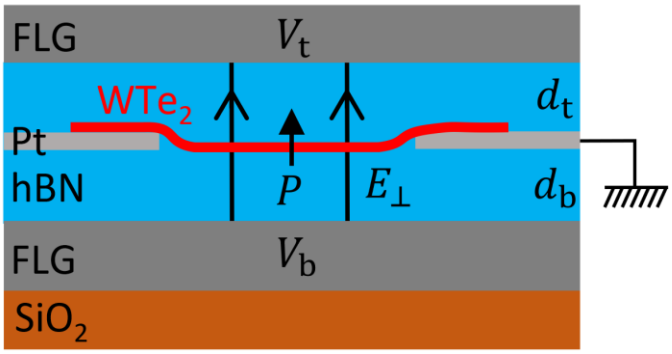

Figure 2.3. Cross-section of a device with dual graphite gates. Perpendicular electric field is applied to a thin WTe_2 flake by changing top gate voltage (V_t) and bottom gate voltage (V_b).

Measurements of four-terminal conductance G as a function of $E_\perp$ in tri-, bi- and mono-layer WTe_2 devices are shown in Fig. 2.4. WTe_2 flakes are undoped by setting $V_t/d_t = -V_b/d_b$. Bistability of G is only observed in trilayer (Fig. 2.4a) and bilayer (Fig. 2.4b) devices near $E_\perp = 0$ at all temperature T from room temperature to 4 K, but not in monolayer (Fig. 2.4c) device. The reason is that the monolayer WTe_2 has a center of symmetry (Fig. 2.4c inset) and is hence non-polar. This is not only evidence of ferroelectric switching in bilayer and trilayer WTe_2, but it also rules out instabilities involving charge injection into the hBN. Note that a larger field is required to switch the trilayer than the bilayer WTe_2.

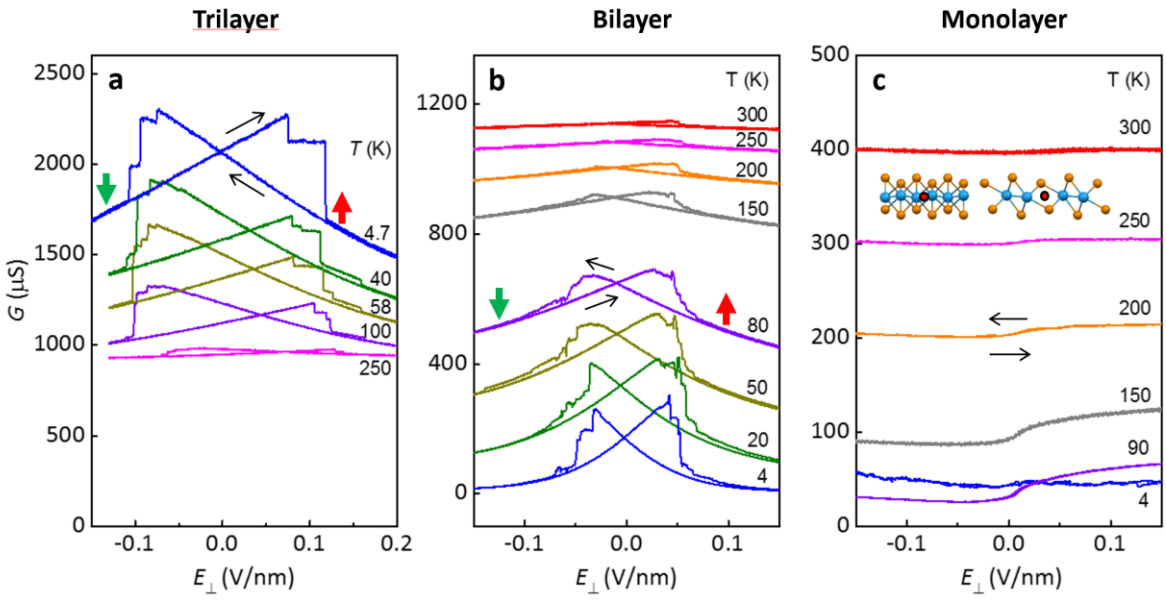

Figure 2.4. Conductance G of undoped tri-, bi- and mono-layer WTe_2 as $E_\perp$ is swept in both directions. Black arrows show sweeping direction of $E_\perp$ and green and red arrows show the direction of polarization. **a**, Bistability of trilayer WTe_2 device TW1. G of the trilayer WTe_2 increases with cooling down which shows a metallic temperature dependence. While $E_\perp$ is swept, G shows bistability associated with electrical polarization up and down, which occurs at all temperatures from 300 K to 4 K. The directions of polarization are shown by red and green arrows. **b**, Bistability of bilayer WTe_2 device BW5. Although G of the undoped bilayer WTe_2 shows an insulating temperature dependence, the bistability still preserves. **c**, The same measurement on monolayer WTe_2 device MW1, showing no bistability. Insets: red circle is the center of symmetry in the monolayer WTe_2.

2.4 Detecting the out-of-plane polarization

The conventional ways to detect polarization switching in insulating ferroelectrics are measurements of either $P-E$ curves or displacement current. But these conventional

measurements are very hard to be carried out for few-layer WTe_2, since the polarization density is very small, and the device area is small too. So, we developed a technique with a graphene electric field sensor on top. Figure 2.5 shows optical image and cross-section of this type device BW2. The conductivity of graphene G_{gr}, which can be measured by top gold contacts directly, is sensitive to the electric field E_t beneath it.

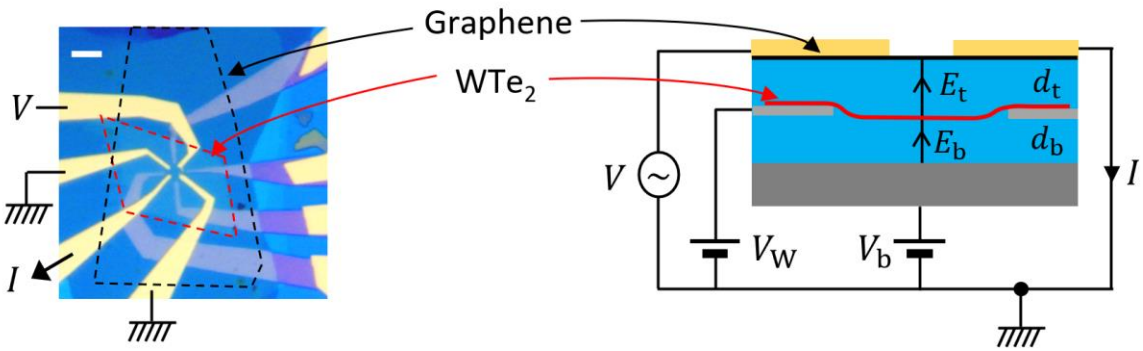

Figure 2.5. Optical image and schematic cross-section of a bilayer device BW2.This device has a separately contacted graphene top gate. Scale bar: 5 μm.

Figure 2.6 presents measurements on a bilayer WTe_2 device BW2 with multiple gold contacts to the top graphene. When the top graphene is grounded, the conductance of bilayer WTe_2 shows a bistability as the bottom gate voltage V_b is swept up and down. Because V_b changes both the perpendicular electric field and doping of the bilayer WTe_2, G changes in a bigger range as compared with Fig. 2.4b. The bilayer WTe_2 can also be used as a gate for the graphene. As shown in the inset to Fig. 2.6b, graphene conductance G_{gr} shows a minimum near WTe_2 voltage $V_W = 129$ mV. In another way, measurement of G_{gr} versus V_b can be done by fixing the voltage of bilayer WTe_2 (V_w), as presented in Fig. 2.6b. G_{gr} is measured by passing current through opposite contacts while the two side contacts are grounded to prevent the parallel current that flows through the part of the top graphene, which is not screened from the bottom gate by the bilayer WTe_2. The

blue curve shows the hysteresis of G_{gr} at $V_W = 0$ mV with the same range of V_b as it does in the bilayer WTe_2 conductance. The red curve shows the same measurement at $V_W = 129$ mV. When $V_W = 129$ mV, G_{gr} is not sensitive to electric field as the minimum is quite broad so no hysteresis is shown. The change of G_{gr} is mainly due to the parallel conductance. So, we can remove this parallel conductance by subtracting the blue curve by the red curve as shown by black curve.

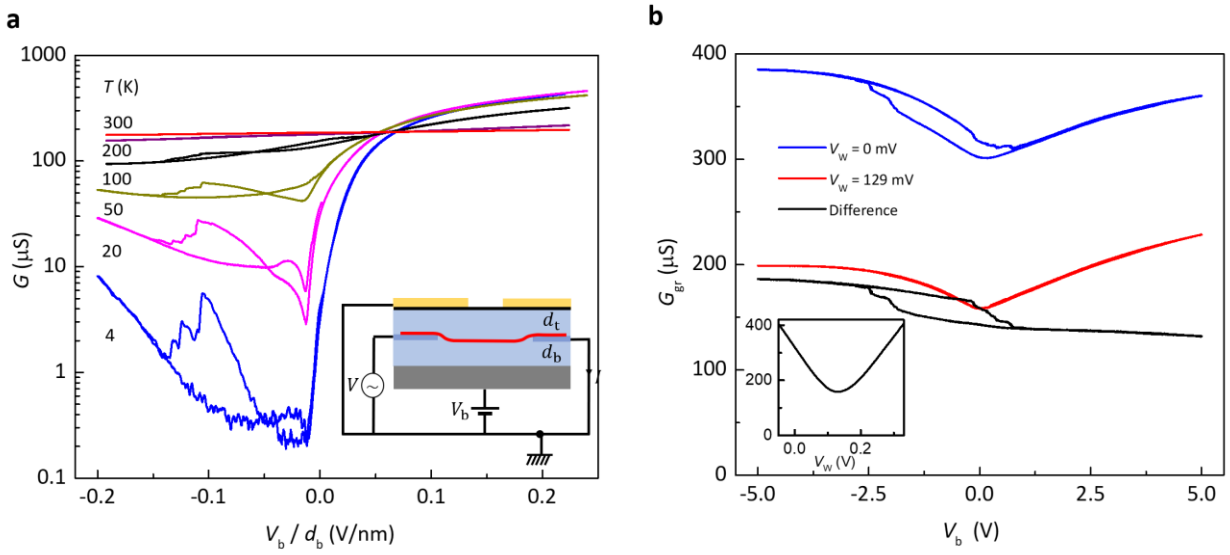

Figure 2.6. Bistability of bilayer WTe_2 in device BW2 and removal of parallel conduction. **a**, Conductance of the bilayer WTe_2 (G) as a function of V_b/d_b. Inset shows a schematic configuration of measurement. **b**, Graphene conductance (G_{gr}) as a function of V_b at 220 K. Inset shows that G_{gr} has a minimum around WTe_2 voltage $V_W = 129$ mV. (Figure taken from Ref. (*21*))

To illustrate the effect of out-of-plane polarization in the WTe_2 on G_{gr}, a sketch of the potential landscape is drawn in Fig. 2.7d for the simplified case of $d_t = d_b$, and the bottom gate, bilayer WTe_2 and graphene are all grounded. Red and green curves show the electrical potential for polarization up and down, respectively. Even though the potential at the center of bilayer WTe_2 must be zero, the two layers of bilayer WTe_2 have opposite potential due to the spontaneous polarization. For the up polarization, a positive electric field is applied to the graphene, which

changes to negative for down polarization. δE_t is the change of electric field to the graphene when the polarization is switched. To measure δE_t, a bias V_w is applied to the bilayer WTe_2 and the change $\delta V = d_t \delta E_t$ is measured. The same value of G_{gr} is changed by changing δV of V_w with switching of polarization. From 4 K to 300 K, clear hysteresis loops are seen in G_{gr} while V_b is swept up and down. Then we can convert the difference of G_{gr} between the two bistable states in Fig. 2.7a to approximate δV. The result is plotted as a function of temperature T in Fig. 2.7e. It decreases roughly linearly with T between 60 K to 300 K, extrapolating to zero at roughly 450 K, which provides a rough estimate for Curie temperature of bilayer WTe_2.

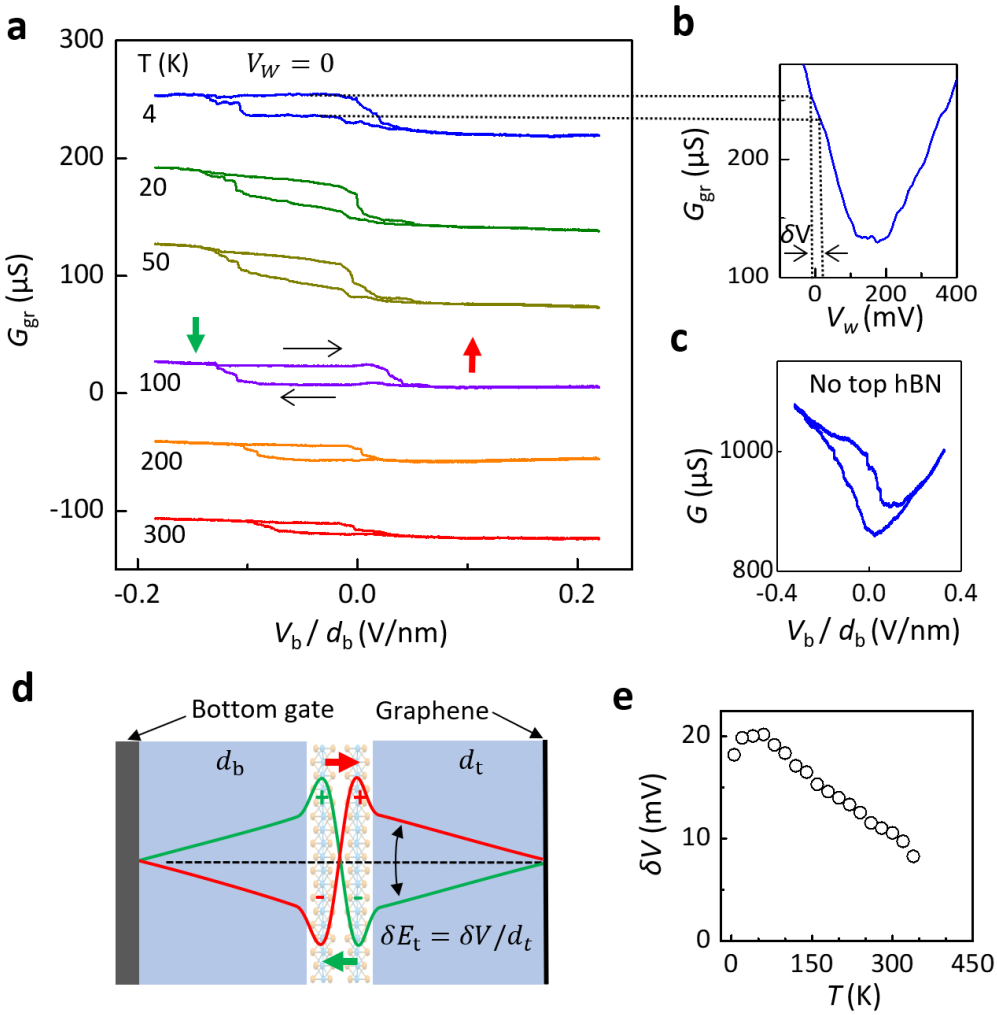

Figure 2.7. Temperature dependence of polarization in bilayer WTe_2. **a**, G_{gr} as a function of V_b after removing parallel conductance at $V_W = 0$ and different temperatures. Black arrows show sweeping direction of V_b. The two conductance states seen for sweeping up and down are associated with different out-of-plane polarization (red and green arrows). **b**, G_{gr} versus V_W with y-axis having the same scale with panel **a**. The difference of two states of G_{gr} can by mapped out to δV. **c**, Characteristic of a simple device BW3 with no top hBN between graphene and bilayer WTe_2. **d**, Sketch showing how switching polarization of bilayer WTe_2 changes E_t. **e**, δV mapped out by panel **a** and **b** as a function of temperature.

A simplified model is used to estimate the spontaneous polarization of the bilayer WTe_2 from δV. In the model, we assume $d_t = d_b \gg d$, where d is the thickness of the bilayer WTe_2; all conductors (bottom graphite gate, top graphene and the middle of bilayer WTe_2) are grounded with infinite electronic compressibility, and that the polarization charge can be modelled as delta functions separated by d. Under these assumptions, the electric field in the bottom and top hBN would be the same, i.e E_t. Using Gauss's law,

$$\varepsilon_o \varepsilon_{hBN} E_t = \varepsilon_0 E_i + P/d \tag{26}$$

Here, E_i is the electric field between the two layers of WTe_2, and P is the areal polarization density of the bilayer WTe_2. Since the top graphene is also grounded, the potential drops between the middle of the bilayer WTe_2 and the top graphene (or the bottom graphite) is

$$E_t d_t + E_i d/2 = 0 \tag{27}$$

From (26) and (27), we have

$$E_t = \frac{P}{\varepsilon_0 (2d_t + \varepsilon_{hBN} d)} \tag{28}$$

Thus, the difference between the two polarizations is $\delta E_{\mathrm{t}} = \frac{2P}{\varepsilon_0(2d_{\mathrm{t}}+\varepsilon_{\mathrm{hBN}}d)}$. With $2d_{\mathrm{t}} \gg \varepsilon_{\mathrm{hBN}}d$, $P \approx \varepsilon_0 d_{\mathrm{t}} \delta E_{\mathrm{t}} = \varepsilon_0 \delta \mathrm{V}$. At 20 K, this estimation gives $P \approx 1 \times 10^4\ e$ per cm. This is equivalent to transferring $\sim 2 \times 10^{11}$ cm^{-2} electrons from one layer to the other layer which are spaced by 0.7 nm.

We also made a similar but much simpler device with no top hBN and monolayer graphene directly encapsulating bilayer WTe_2 (Fig. 2.7c). It exhibited substantial, highly reproducible hysteresis in the conductance from 4 K to 300 K, showing that the ferroelectric switching is robust enough for practical purposes in combination with other 2D materials, even at room temperature.

Recently, nanoscale piezo-response measurements (*39*) were done on thicker WTe_2 (about 10 nm), where bistable spontaneous ferroelectric polarization state was observed and switched under external electrical bias.

2.5 Gate tuning of the ferroelectric behavior

We have already discussed the perpendicular electric field dependence of ferroelectricity. In this section, let us see the effect of gates in another way. We define the gate-induced areal density of added electrons as

$$n_e = \varepsilon_{hBN}\varepsilon_0(V_t/d_t + V_b/d_b)/e \qquad (29)$$

In Fig. 2.8a&b we plot the 2D map of conductance G of a bilayer WTe_2 of device BW5 at $T = 7$ K as a joint function of V_t and V_b. V_t is stepped and V_b swept up for Fig. 2.8a or down for Fig. 2.8b, respectively. The black dashed line denotes $E_\perp = 0$ and the white dashed line denotes $n_e = 0$. For

each sweep, we always start from the same polarization state. The two plots are different in the central hysteretic region.

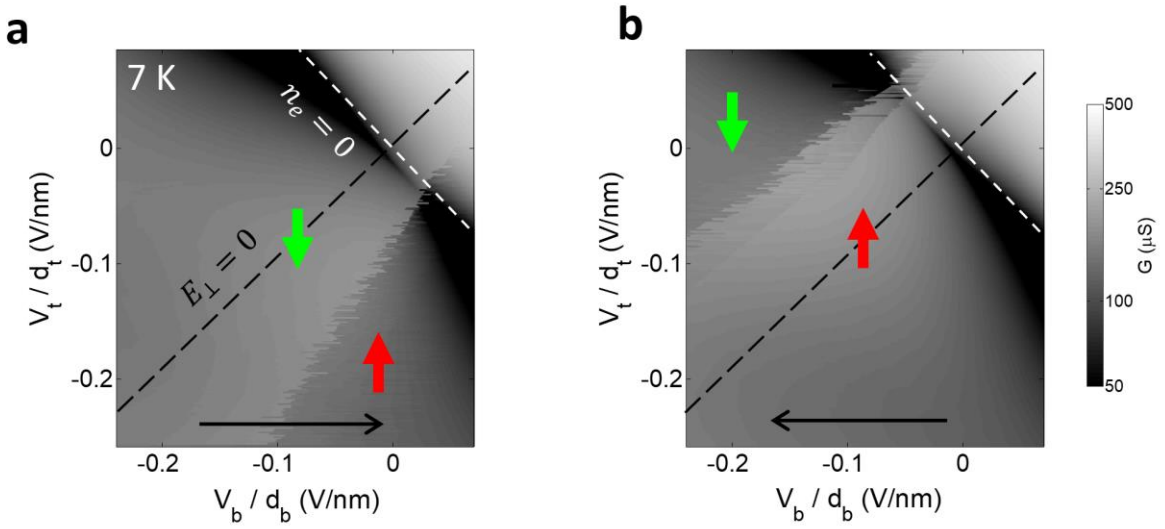

Figure 2.8. Conductance G of a bilayer WTe_2 of device BW5 at 7 K as a function of both gate voltages. G is plotted as a function of top and bottom electric field E_t and E_b as E_b is swept up (**a**), and down (**b**), as indicated by black arrows. The red and green arrows represent the direction of polarization. Dashed lines indicate zero perpendicular field $E_\perp$ and zero charge density n_e.

The difference between two plots in Fig. 2.8 are plotted in Fig. 2.9a. G is the same for two sweeping directions in the white regions. G is also a similar function of n_e for both up polarization (P↑) and down polarization (P↓) at $E_\perp = 0$. As shown in Fig. 2.9c, bilayer WTe_2 is metallic above a certain density, $n_e > n_c \sim 2 \times 10^{12} \mathrm{cm}^{-2}$ (*22*). At low temperatures, such as 7 K, an increase in the width of the hysteresis loop for increasing negative n_e is observed. Whereas at 200 K, the width of the hysteresis loop is almost independent with n_e as shown in Fig. 2.9b.

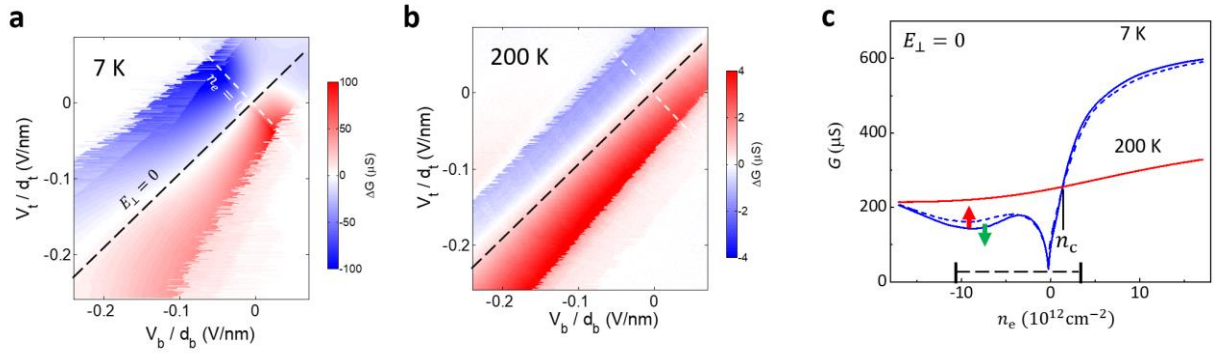

Figure 2.9. Comparison of G at polarization up and down. **a**, The difference between the two plots in Fig. 2.8. **b**, Same measurements as in panel **a**, but at 200 K. **c**, Variation of G with n_e at $E_\perp = 0$ for both polarization states at 7 and 200 K.. The black dashed line shows the range of n_e in **a** and **b**.

Figure 2.10 shows traces obtained by sweeping $E_\perp$ repeatedly up and down at selected values of n_e. In each case, a single conductance level was seen at large $E_\perp$. By sweeping $E_\perp$, G changes smoothly and reproducibly into one of the two stable levels as $E_\perp$ is reduced to zero, which implies no domain formation at $E_\perp = 0$. Then G changes rapidly by several steps near the coercive field. The details of transition between two polarization states vary among with different sweeps. For small or negative n_e, the effect of $E_\perp$ and polarization is large, which produces bowtie-shaped hysteresis loops. For n_e well above n_c, $E_\perp$ has less effect and the hysteresis is smaller but it is still observable. Hence, just like trilayer WTe_2, the doped bilayer WTe_2 is simultaneously ferroelectric and metallic.

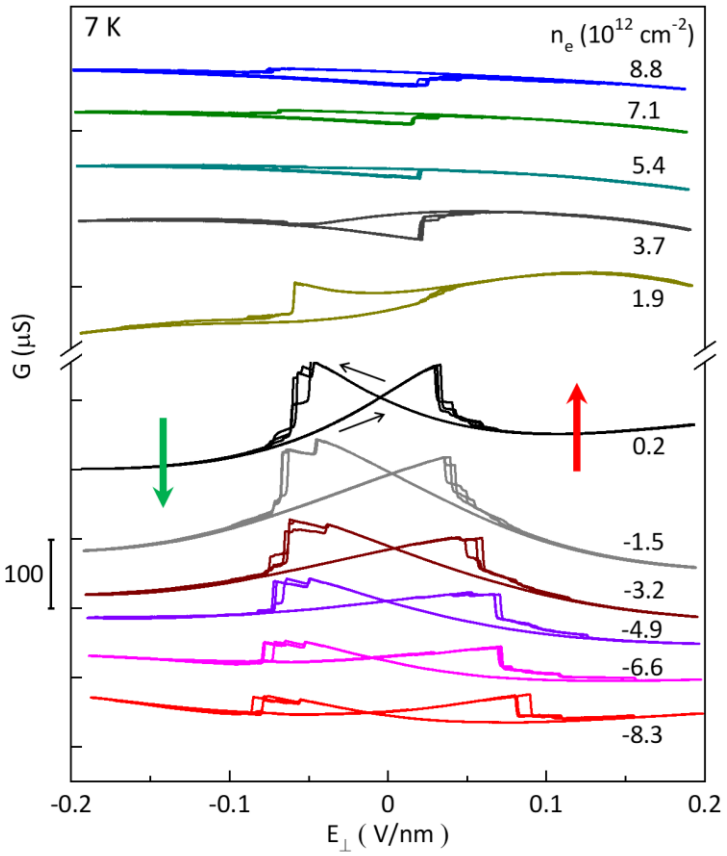

Figure 2.10. Sweep of $E_\perp$ at different n_e at 7 K. Black arrows show sweeping direction of $E_\perp$ and green and red arrows show the direction of polarization. The traces are shifted vertical for clarity.

We also measured gate dependence for channels with different length in a trilayer WTe_2 device TW1. The bottom gate is always grounded, and the top gate is swept. We found that the metal contacts prevent the polarization from switching when the length is reduced to a few hundred nanometers. When the length is more than 480 nm, all channels show the similar hysteric behavior.

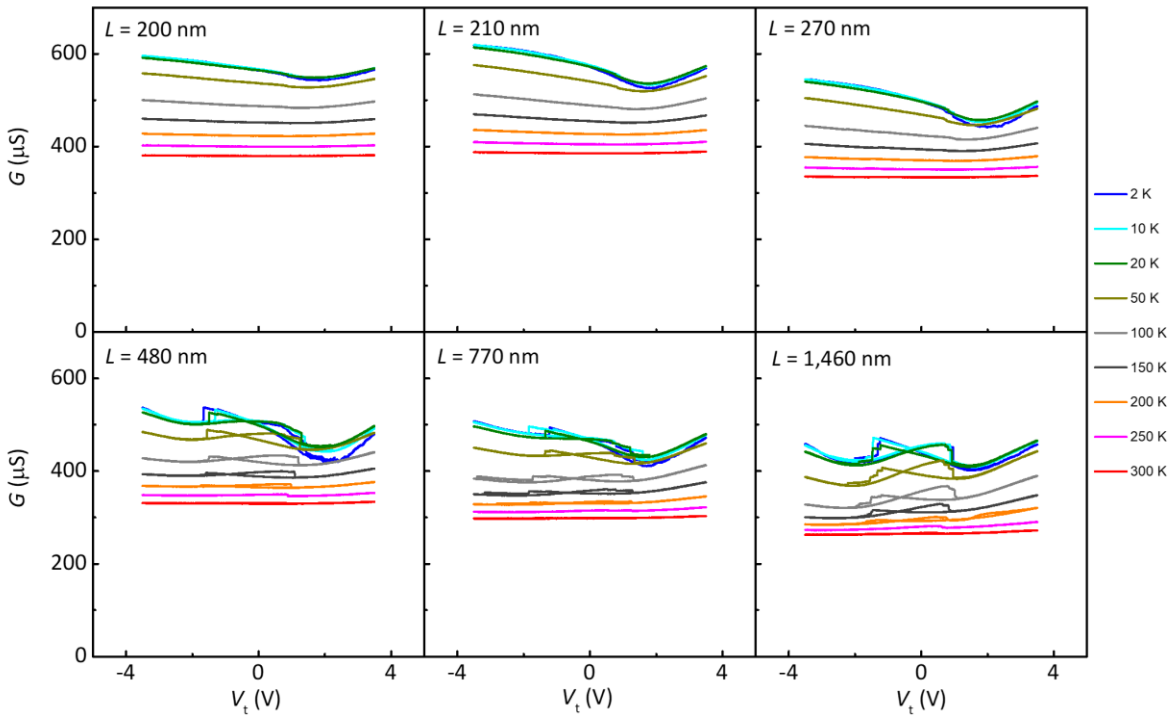

Figure 2.11. Gate dependence for different channel length in device TW1. The length of channel is labelled on the right top of each panel. (Figure taken from Ref. (*21*))

2.6 Magnetic field dependence of bilayer WTe_2 devices

We first examine the ferroelectricity at different out-of-plane magnetic fields (B). As shown in Fig. 2.12, hysteresis does not change with the magnitude of B.

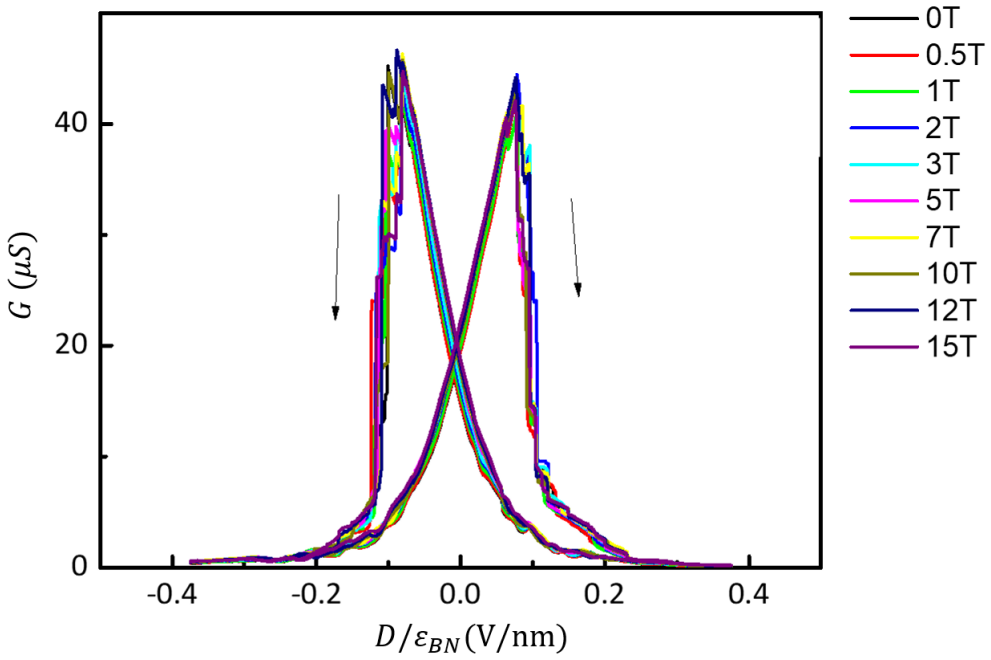

Figure 2.12. Sweep of $E_\perp$ at different B at 1.6 K for device BW5. n_e is set to $-1.5 \times 10^{12}\text{cm}^{-2}$. Black arrows indicate the sweeping direction.

At higher doping levels, a Shubnikov-de Hass (SdH) oscillation is observed as shown in Fig. 2.13. A single frequency about 20 T appears below 8 K with $V_\text{t} = 4.5$ V and $V_\text{b} = 7.8$ V. A 2D map of ΔR_xy as a function of B and V_b at $V_\text{t} = 4.5$ V is obtained. The 2D map shows a fan diagram which indicates a single electron pocket at high electron doping.

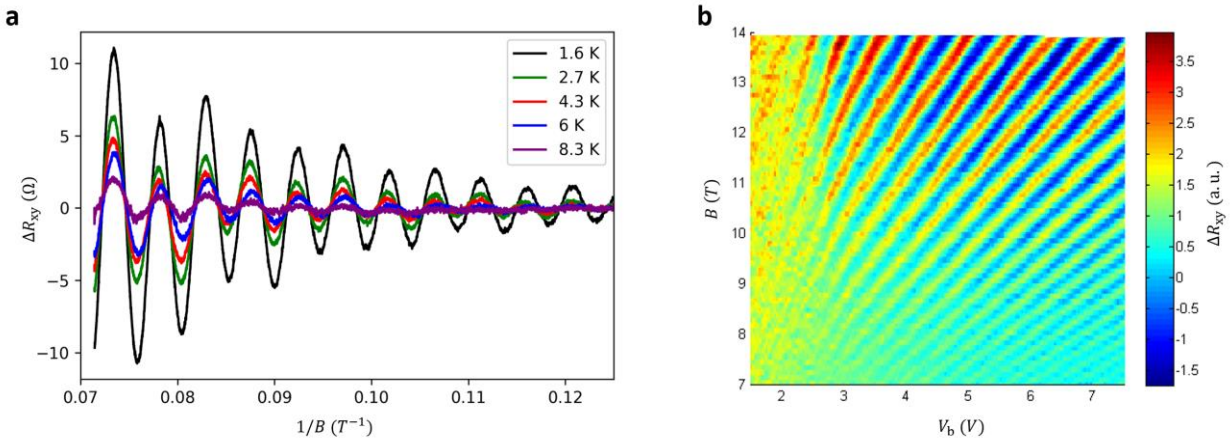

Figure 2.13. Shubnikov-de Hass (SdH) oscillation in bilayer WTe_2 device BW5. **a**, Change of Hall resistance ΔR_{xy} as a function of $1/B$ at different temperatures with $V_t = 4.5$ V and $V_b = 7.8$ V. **b**, ΔR_{xy} as a function of B and V_b at $V_t = 4.5$ V and $T = 1.6$ K.

The oscillation disappears for moderate doping level. But strangely, an oscillation comes back for low doping level as shown in Fig. 2.14. A 2D map of longitudinal conductance G_{xx} as a function of V_t and V_b is shown in Fig. 2.14a. A ferroelectric switching is seen when $E_\perp$ is around 0. With the $V_t = 2.2$ V and $V_b = -2.7$ V as indicated by the red dot in Fig. 2.14a, an oscillation with more than one frequency was observed as shown in Fig. 2.14b. This oscillation can be seen up to 30 K.

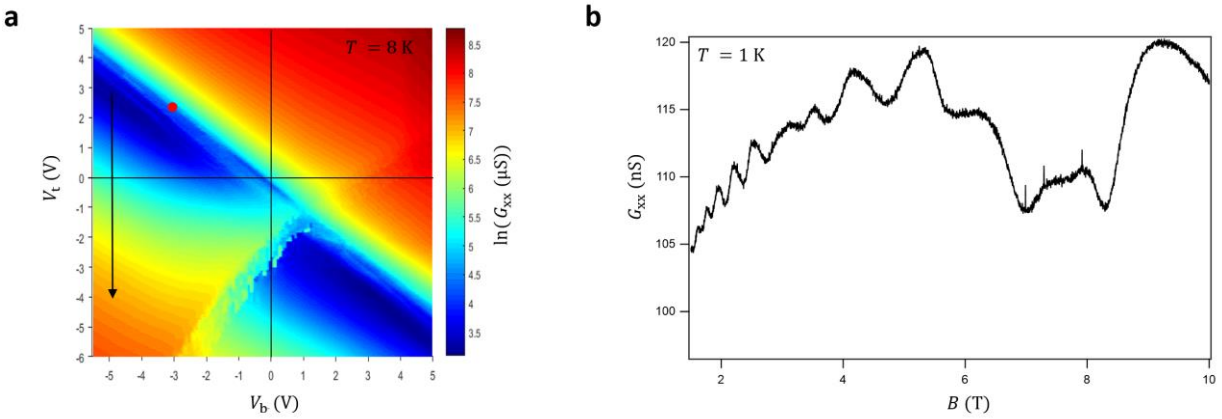

Figure 2.14. Oscillation in the longitudinal conductance G_{xx} of a bilayer WTe_2 at low doping in device BW6. **a**, A conductance as a function of V_t and V_b while V_b is stepped and V_t is scanned in the direction pointed by the black arrow at 8 K. **b**, G_{xx} as a function of an out-of-plane magnetic field at 1 K and $V_t = 2.2$ V, $V_b = -2.7$ V shown by the red dot in panel **a**. The onset of the oscillation is as low as 1.5 T.

The fan diagram is obtained by fixing $E_\perp$ and scanning B and n_e as plotted in Fig. 2.15. Two sets of fans can be seen. One frequency is increased and another one is decreased by adding

electrons to the bilayer WTe_2. And both frequencies increase with the magnitude of $E_\perp$. It suggests that one frequency is controlled by a conduction band and another by a valence band.

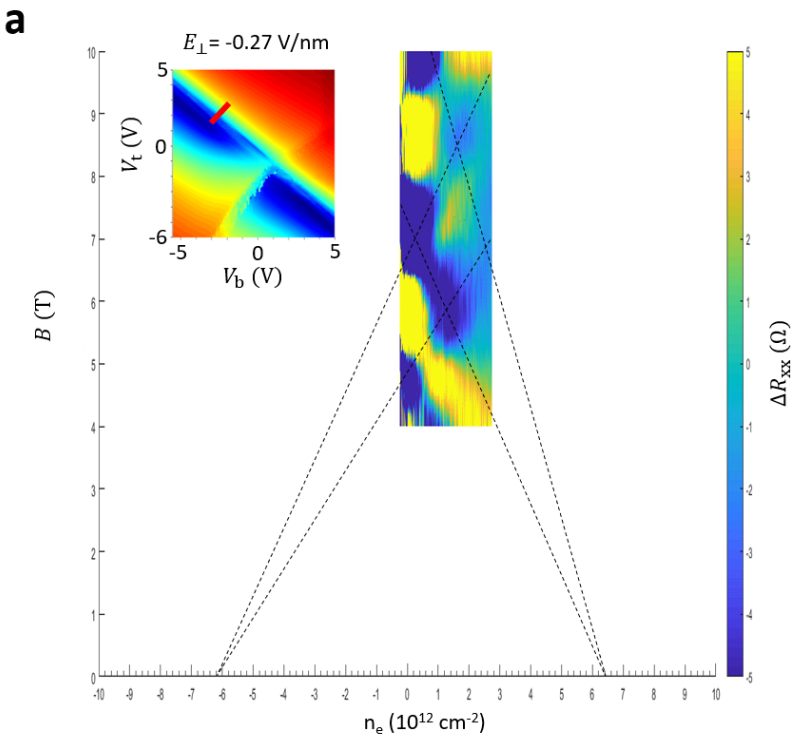

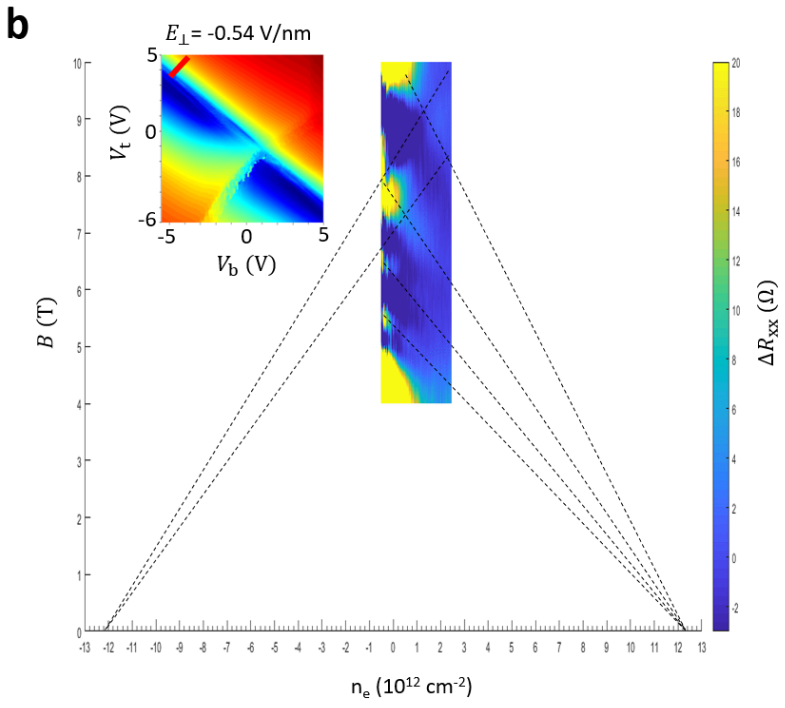

Figure 2.15. Fan diagrams for two different perpendicular electric fields at $8\,\mathrm{K}$. **a**, $E_\perp = -0.27\,\mathrm{V/nm}$. **b**, $E_\perp = -0.54\,\mathrm{V/nm}$. The carrier density is scanned along the red line in inset. Dashed black lines are guide for eyes.

To find the nature of the oscillations, we also measured longitudinal R_{xx} as a function of B and either V_t or V_b with another gate voltage fixed, as shown in Fig. 2.16. When the V_t is fixed to $3.6\,\mathrm{V}$, the frequency of oscillation is tuned by the V_b. But the frequency of oscillation is not changed by the V_t when V_b is fixed to $-3.4\,\mathrm{V}$.

In conclusion, we observed two oscillating frequencies at low doping of bilayer WTe_2. Each frequency is controlled by one of the gates. There are two possible explanations. The first one is that the perpendicular field can penetrate graphite gate to introduce 2DEG on its surface. Then the chemical potential of this 2DEG will oscillate with B and the carrier density of the bilayer WTe_2 follows the oscillation. The second one is that perpendicular electric field separate electrons and holes of the bilayer WTe_2. Each layer WTe_2 can screen the adjacent gate and the frequency of oscillation depends on the carrier density of separated carriers.

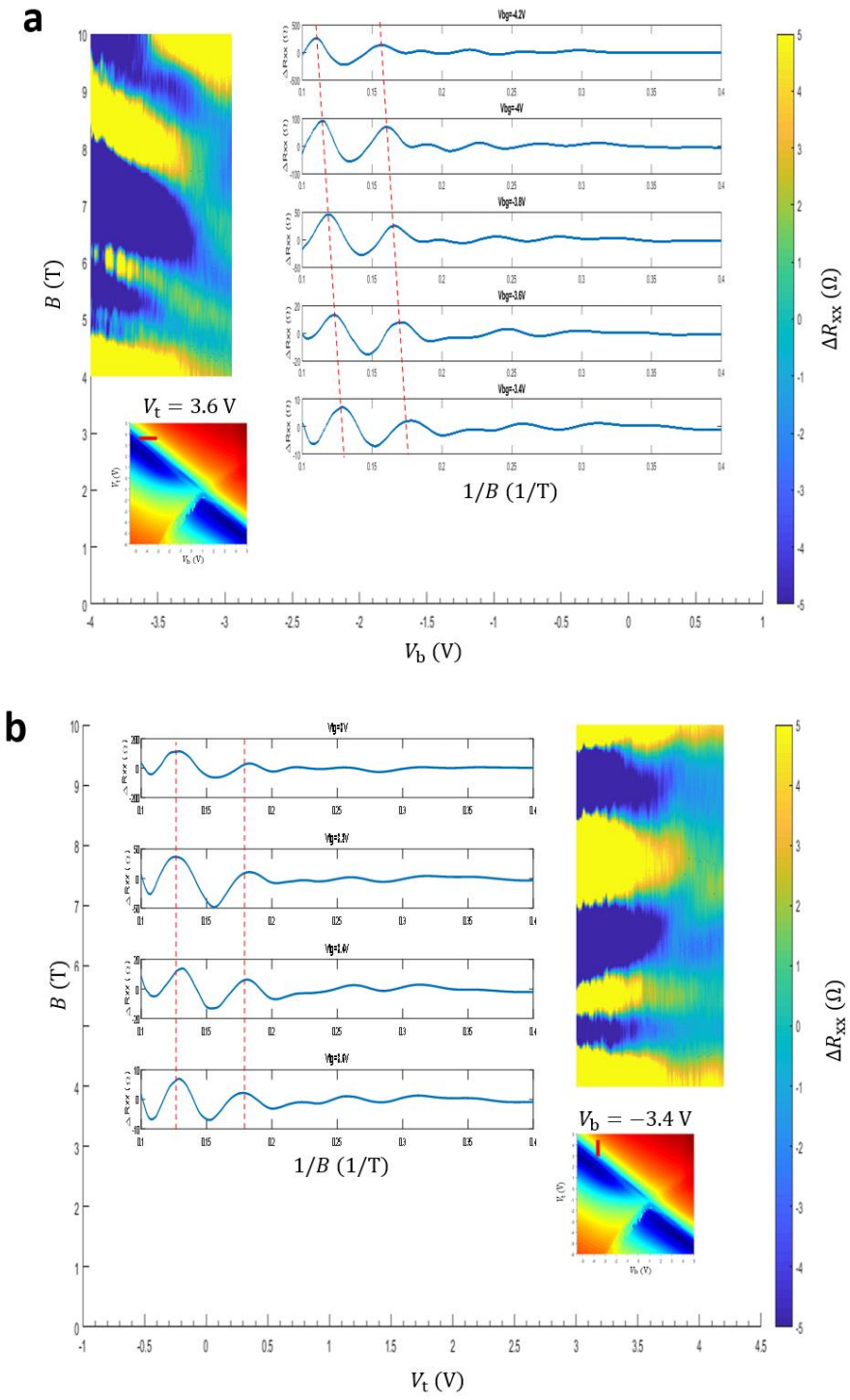

Figure 2.16. Fan diagrams when one gate voltage is fixed at 6 K. **a**, $V_t = 3.6$ V. **b**, $V_b = -3.4$ V. The bottom or top gate voltage is scanned along the red line in the small inset. The line cuts of the fan diagram are drawn in the big inset. The dashed red lines track the same peak.

2.7 Possible theoretical explanation of ferroelectric switching

Recently, a theory for the ferroelectric switching in bilayer and multilayer WTe_2 was proposed (*40*). By first-principle calculations, they show that the polarization is the result of uncompensated interlayer vertical charge transfer. When the polarization is switched, the layers of WTe_2 slide in the x-y plane.

In the case of bilayer WTe_2, the top layer is moved by 0.072 nm along the y-axis as shown in Fig. 2.17. We also can test it by performing a horizontal mirror reflection. The operation will slide the top layer and flip the polarization.

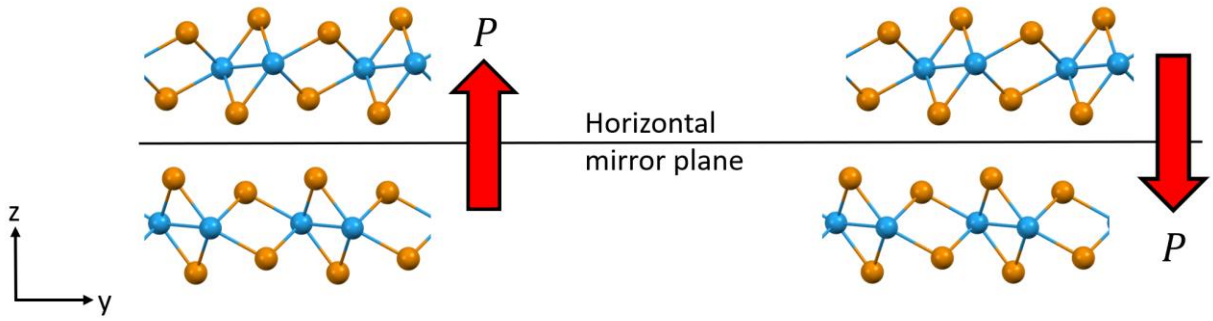

Figure 2.17. Geometric structure of bilayer WTe_2 for two polarization states. The polarization is indicated by red arrows.

2.8 Conclusion and future outlooks

In this chapter, we investigated the coexistence of ferroelectricity and metallicity in trilayer WTe_2 and doped bilayer WTe_2. Polarization can be switched by a perpendicular electric field even in combination with other 2D materials and at room temperature. We developed a technique with a graphene electric field sensor which can be used in the future to detect tiny electric field change in nanoscale.

In addition, both normal and unexpected quantum oscillations were observed in bilayer WTe_2. To clarify the origin of the latter, experiments on metal gated device needs to be done in the future. Because the perpendicular electric field cannot penetrate a metal gate to introduce a 2DEG on its surface, if the unexpected oscillation is still observed in such a device, the explanation that electrons and holes separated in two layers WTe_2 by perpendicular electric field would be favored.

Chapter 3. Monolayer WTe_2: 2D topological insulator

3.1 Introduction of 2D topological insulator

Chern number and Z_2 index, discussed in section 1.4, describe the topological property of a system. When the Z_2 index of a 2D system equals 1, it is called a 2D topological insulator or quantum spin Hall insulator. In 2005, Kane and Mele introduced the Z_2 index as a topological invariant and used it to discuss the quantum spin Hall (QSH) effect in graphene (*14*, *15*).

The low energy $\boldsymbol{k}\cdot\boldsymbol{p}$ model for graphene around the K' point is shown by equation (9). Near K and K' points, the Hamiltonian can be written as

$$H_0 = v_F(\sigma_x\tau_z q_x + \sigma_y q_y) \tag{30}$$

where $\sigma_z = \pm 1$ describes states on the A(B) sublattice, $\tau_z = \pm 1$ describes states at $K(K')$ and q is the momentum relative to $K(K')$. Equation (30) describes a gapless linear dispersion with two Dirac points located at K and K'. To drive the Dirac dispersion to a dispersion of an insulator, a gap needs to be opened by an extra term. The term needs to satisfy the symmetries of graphene, including time-reversal, inversion, and in-plane mirror symmetries. The possible terms are staggered sublattice potential (σ_z), Haldane's term ($\sigma_z\tau_z$) (*41*), the Rashba effect ($\sigma_x\tau_z s_y - \sigma_y s_x$) and spin-orbit interaction ($\sigma_z\tau_z s_z$) (*14*). Among the four possible terms, only the spin-orbit interaction term does not violate any symmetry. After introducing the spin-orbit interaction term, the insulating state of graphene becomes topologically nontrivial and Z_2 index was invented to classify the topological order in time-reversal invariant systems.

Here, I will just show a very simple view of the consequence of the spin-orbit interaction term. The Hamiltonian of graphene is then written as

$$H = v_F\left(\sigma_x\tau_z q_x + \sigma_y q_y\right) + \Delta_{so}\sigma_z\tau_z s_z \tag{31}$$

H near the K point for spin up then can be written as

$$H(\tau_z = 1, s_z = 1) = \begin{pmatrix} \Delta_{so} & q_x - iq_y \\ q_x + iq_y & -\Delta_{so} \end{pmatrix} \tag{32}$$

When the momentum is very small, $H(\tau_z = 1, s_z = 1)$ becomes

$$\lim_{q_x, q_y \to 0} H(\tau_z = 1, s_z = 1) = \begin{pmatrix} \Delta_{so} & 0 \\ 0 & -\Delta_{so} \end{pmatrix} \tag{33}$$

That means the states for the conduction and valence bands at the K point are $|A,\uparrow\rangle$ and $|B,\uparrow\rangle$, respectively. $|A,\uparrow\rangle$ represents the wave function centered at A sublattice with spin up. We can do the same thing for the other three combinations of spin and Dirac point, summarized in Fig. 3.1. Spin is conserved in the Hamiltonian which means s_z is a good quantum number. We then can use spin up and down (Kramers pairs) to divide the Hilbert space into two subspaces. For the valence band, the state changes from $|B,\uparrow\rangle$ to $|A,\uparrow\rangle$ when the momentum moves from K to K'. The sign of the band gap is different at K and K'. The Chern number for the valence band with spin up or down is 1 or -1. Thus the Z_2 index is 1 for graphene gapped by spin-orbit interaction.

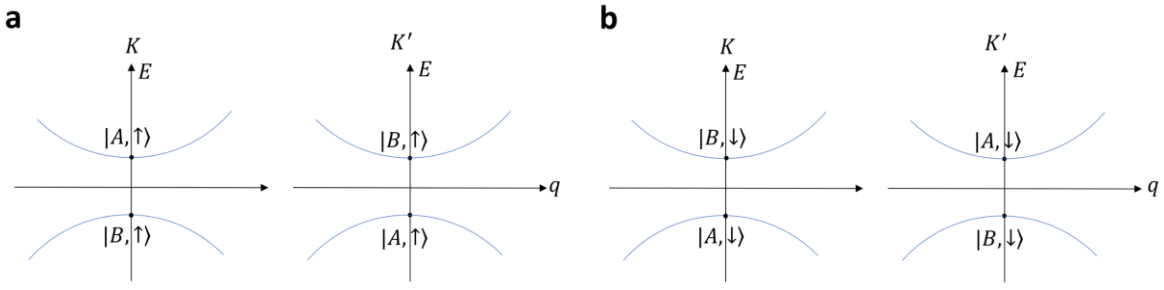

Figure 3.1. Dispersion near K and K' after consideration of the spin-orbital interaction. **a**, Spin up states. **b**, Spin down states. The states at the band edge are labeled nearby.

Vacuum is a topological trivial insulator with Z_2 index of 0. At the physical edge of a system with Z_2 index of 1, topological order changes. A gapless state thus is guaranteed to localize at the physical edge. This edge state only has two channels, where the state with spin up moves to one direction and another state with spin down moves to the opposite direction. Due to the time reversal symmetry, back scattering between the two states by a non-magnetic disorder is forbidden.

Experimental observation of the QSH effect in graphene is still lacking, due to the very weak spin-orbit coupling of carbon atoms. Following that, Zhang et al. predicted that the QSH effect can be realized in mercury telluride-cadmium telluride semiconductor quantum wells (*42*). Experimental growth of the quantum well was achieved soon after and quantized edge conductance was indeed observed, which is the first experimental evidence of the QSH state (*43*). Later, the QSH effect was reported in InAs/GaSb quantum wells (*44*).

3.2 Monolayer WTe_2

Layered transition metal dichalcogenide (MX_2) contains 3 atomic layers, M-X-M. For the 1H and 1T structure, the atoms in each atomic layer are arranged in a triangular lattice. Three atomic layers stack together in Bernal (ABA) style for 1H and rhombohedral (ABC) for the 1T structure. Perhaps the most studied MX_2 materials are the semiconductors with M = W or Mo, and X = S or Se, and naturally have 1H stacking. Monolayer WTe_2 is also an MX_2, however, as far as we know, monolayer WTe_2 has the 1T′ structure, a distorted form of 1T. As shown in Fig. 3.2, monolayer 1T′ WTe_2 contains an inversion center (indicated by the red dot), a y-z mirror plane (M), a two-fold glide screw rotational axis (x-axis) and a 1D zigzag tungsten chain along x-axis. The bands near the Fermi level are mainly from tellurium p orbitals and tungsten d orbitals. By introducing spin-orbit coupling, a fundamental gap is opened. Monolayer WTe_2 was predicted to be a QSH

insulator in 2014 (*45*). This attracted great attention to monolayer WTe_2, and several types of experiments evince that monolayer WTe_2 is indeed a QSH insulator (*22–25*, *46*, *47*).

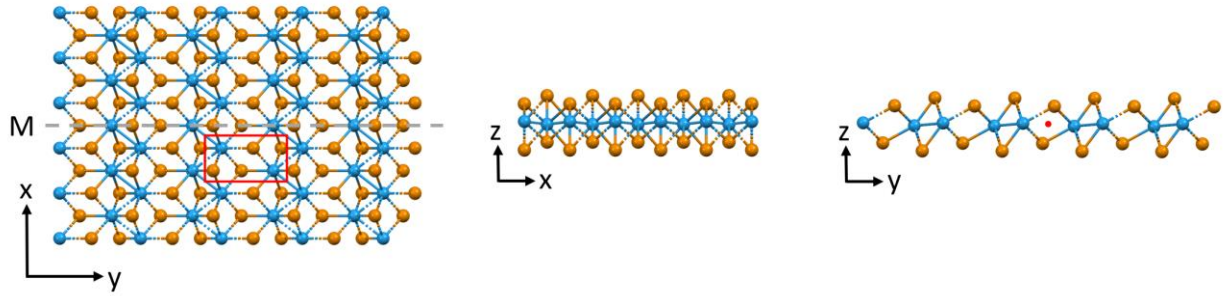

Figure 3.2. Crystal structure of monolayer WTe_2. Dashed grey line in x-y view is the y-z mirror plane. The red box indicates the unit cell. The inversion center is pointed by a red dot. Orange ball: Te atom; Blue ball: W atom.

The edge conduction in monolayer WTe_2 was observed first in Ref. (*22*), as shown in Fig. 3.3. A monolayer WTe_2 device was fabricated by the process described in Section 2.2. Two terminal conductance between adjacent contacts as a function of gate voltage (V_g) was measured at a series of temperatures. In the high doping regime, the conductance increased with cooling down. In the low doping regime, the conductance initially decreased with cooling and then stopped dropping at about 100 K. Below 100 K the minimum broadened with decreasing temperature to form a plateau. To find the origin of the plateau, a special contact geometry shown in Fig. 3.3b was designed and fabricated, which we called pincer contacts. In this geometry, the conductance was always measured by the outer two contacts. In the meantime, the middle contact can be either floated or grounded to either pass or stop any edge current. At low temperatures, the plateau shows up in the low doping regime when the middle contact is floated (black curve in Fig. 3.3b). When the middle contact is grounded, only bulk current can pass and then the plateau drops to 0

conductance (blue curve in Fig. 3.3b). Hence, the insulating bulk and metallic edge of monolayer WTe_2 are distinguished.

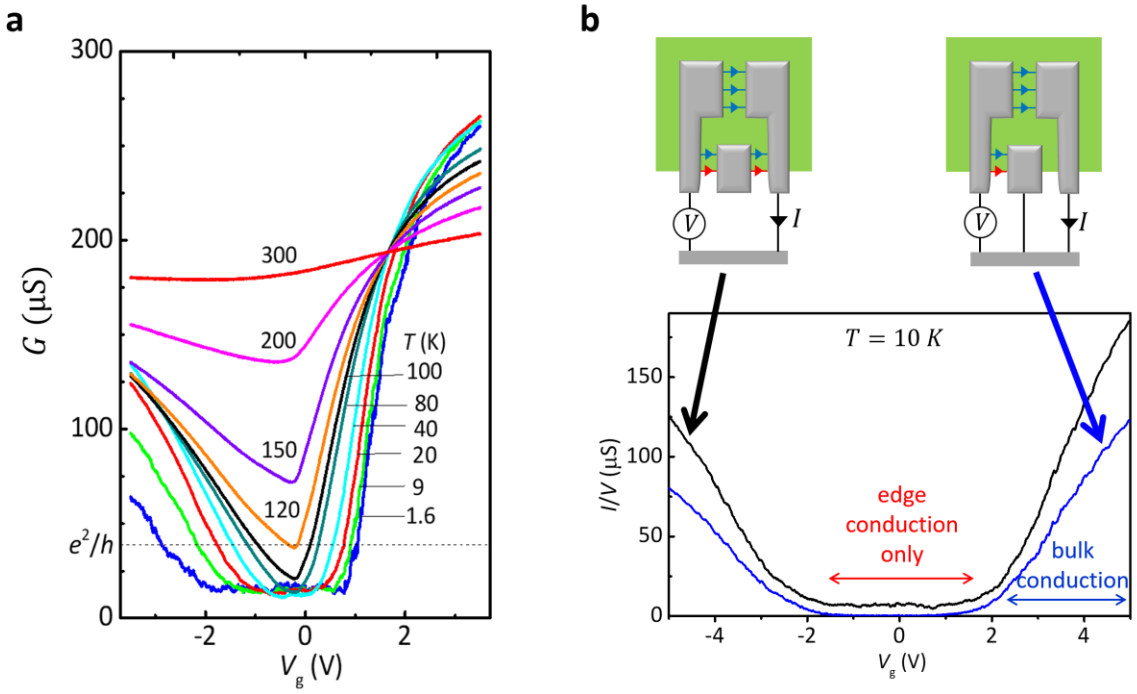

Figure 3.3. Edge conduction in monolayer WTe_2. **a**, Two terminal conductance as a function of gate voltage (V_g) at different temperatures. **b**, Two terminal conductance in a pincer shape contacts device. The bulk and edge current are indicated by blue and red arrows, respectively. Cartoons show the configuration of measurements.

A scanning microwave impedance microscopy (MIM) measurement was performed by the Cui group (*47*). By this technique, a real space, local conductivity map of a monolayer WTe_2 was obtained as shown in Fig. 3.4. Top left panel is the optical image of an unusually big piece of monolayer WTe_2 covered by hBN. In the other panels are three MIM images, where white color means conductive and dark color means insulating. At 4K, it clearly shows the insulating bulk and the conductive edge in monolayer WTe_2.

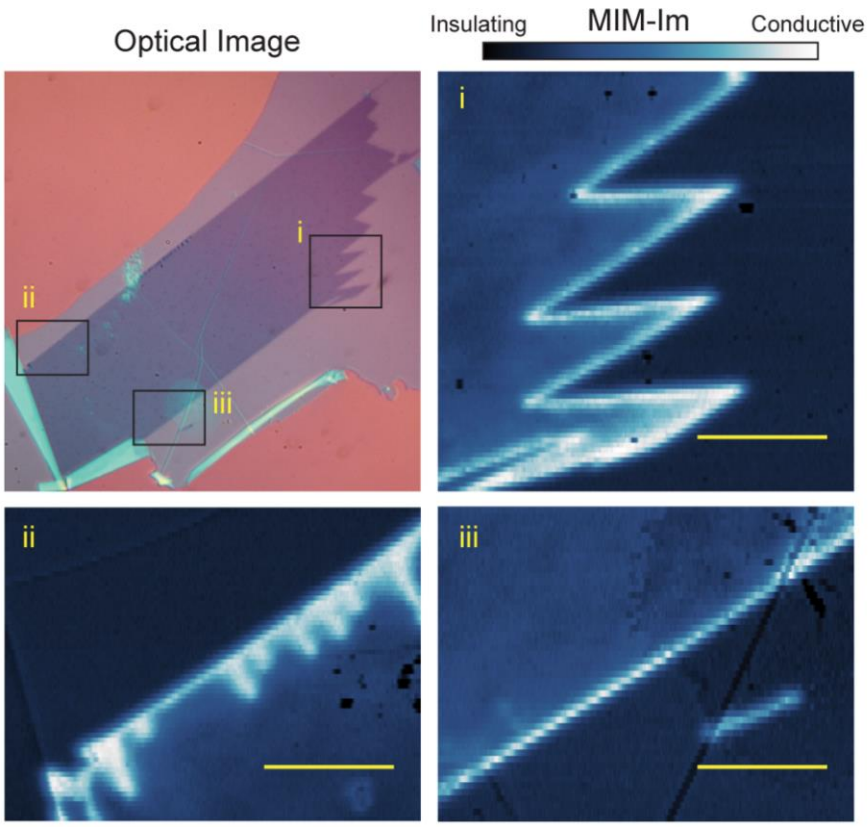

Figure 3.4. Optical and microwave impedance microscopy (MIM) image of a monolayer WTe_2. Optical image of a monolayer WTe_2 covered by hBN is shown on the top left. MIM images of three areas labeled in optical images are plotted in white (conductive) dark (insulating) color scale. Scale bars: 2 μm. (Figure taken from Ref. (*47*)).

Other techniques, such as angle-resolved photoemission spectroscopy (ARPES) (*23*) and scanning tunneling microscopy (STM) (*46*, *48*), were also used to collect the evidence of monolayer WTe_2 being a QSH insulator.

Note that the plateau in Fig. 3.3a is not quantized to e^2/h, where e is the electron charge and h is Planck's constant. Recently, the observation of edge conduction closer to e^2/h up to 100 K was reported (*24*).

3.3 Detection of the spin axis

The spin axis is the direction where the spin of the electron at the QSH edge points. In graphene, the spin axis is restricted to the z-axis by graphene's symmetries. However, the symmetry of monolayer WTe_2 is lower, and does not itself constrain the spin axis to a certain direction. Probing the spin axis of the QSH state is of critical importance for the realization of 2DTI devices, but the spatial resolution of spin- and angle-resolved photoemission spectroscopy is not sufficient for a few-nanometer width QSH edge (*46*). In this section, we will show determination of the spin axis in the edge of monolayer WTe_2 by electronic transport measurement in a vector magnetic field.

First, let us consider a toy model for the QSH state under magnetic field ($\boldsymbol{B}$). The spin axis is assumed to be along the z-axis and the simplest dispersion for the edge state is

$$H_{edge} = ks_z \tag{34}$$

Here, only the Zeeman effect of the magnetic field, $\boldsymbol{B} \cdot \boldsymbol{s}$, is considered. When $\boldsymbol{B}$ is parallel with the spin axis, the Hamiltonian of edge is modified to

$$H_{edge} = (k + B_z)s_z \tag{35}$$

which means that the dispersion is only shifted to the left along k as shown in Fig. 3.5b. When $\boldsymbol{B}$ is perpendicular to the spin axis, the Hamiltonian of edge is modified to

$$H_{edge} = ks_z + B_x s_x + B_y s_y \tag{36}$$

which means that the spin is mixed, and a gap is opened for the QSH edge state as shown in Fig. 3.5c. Hence, magnetoresistance should be minimum/maximum when $\boldsymbol{B}$ is parallel with/perpendicular to the spin axis.

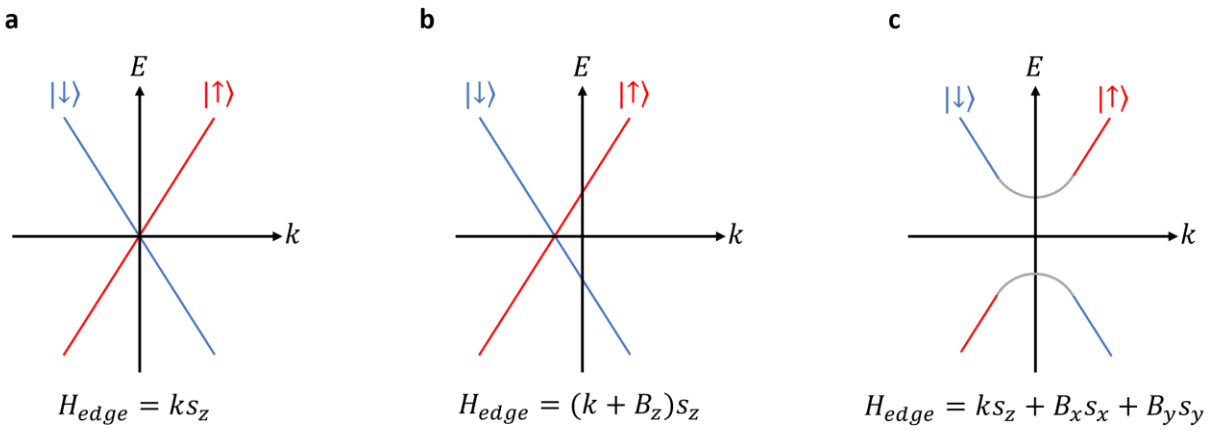

Figure 3.5. Toy model for the QSH state under magnetic field. **a**, Dispersion of the QSH state at zero magnetic field. **b** and **c**, Dispersion of the QSH state when external magnetic field is parallel with the spin axis (panel **b**) or perpendicular to the spin axis (panel **c**).

To determine the spin axis of the QSH state in monolayer WTe_2, devices details such as edge orientation, distribution of cracks, and crystal axes need to be known. After standard device fabrication, MIM imaging and polarized Raman measurements were performed to this end.

The Raman spectroscopy was performed in vacuum at room temperature (*49*). He-Ne laser light at 632.8 nm was focused to a spot size of ~2 μm by an objective at normal incidence. BragNotch™ filters were used to clean the incident scattering and suppress Rayleigh scattering. The reflected light was analyzed by an Andor spectrometer with a 1200 groove/mm diffraction grating. For thick WTe_2, a laser power of 1 mW and an integration time of 30 seconds was adopted, while monolayer flakes were measured with 150 μW and integrated for 3 minutes. In polarization dependence measurements (collinear geometry), a linear polarizer and a half-wave plate were placed right before the objective, shared by the incident and reflected lights. To determine the crystal axes of the monolayers, we used on-chip needle-shaped thick flakes as references, where the W-chain (the x-axis) is known to be along the needle. We can derive the crystal axes of the

monolayer from the relative angle between the polarization patterns of the thick and monolayer flake (Fig. 3.6).

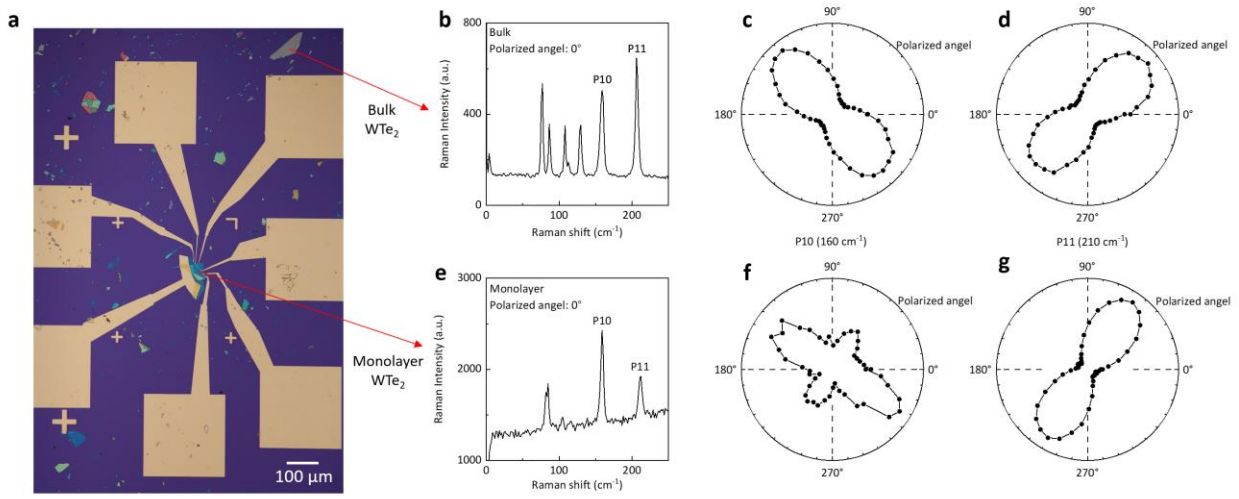

Figure 3.6. Polarized Ramen measurements. **a**, The optical picture of device MW7. **b**, Raman spectrum for bulk WTe_2. **c** and **d**, Raman intensity of bulk WTe_2 as a function of polarized angle for P10 and P11, respectively. **e**, Raman spectrum for monolayer WTe_2. **f** and **g**, Raman intensity of monolayer WTe_2 as a function of polarized angel for P10 and P11, respectively.

The boundary of the monolayer WTe_2 flake is drawn as white dashed line in Fig. 3.7a. Then, a MIM measurement was taken at the center of the device, as shown by black dashed box. In the MIM image, contacts, edges, and cracks can be clearly seen. Between the terminals 1-2 and 2-3, there is only a single edge. Between terminals 3-4 and 4-5, there are an edge and a crack. Between terminals 1-4, there is only a crack. The polarization Raman measurement is plotted in Fig. 3.7b, the x-axis and the y-axis are shown accordingly.

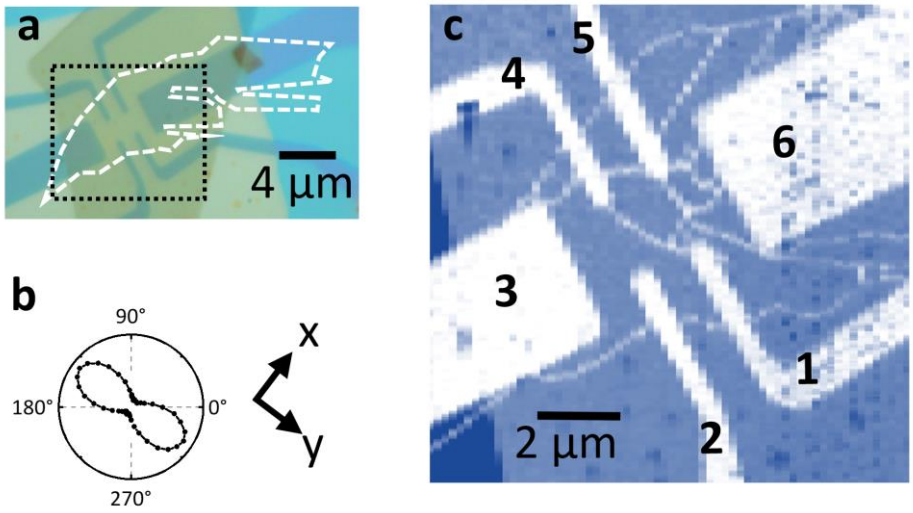

Figure 3.7. Optical and microwave impedance microscopy (MIM) images of monolayer WTe_2 device MW5. **a**, Optical image. The boundary of monolayer WTe_2 is outlined by white dashed line. The MIM scanning area is drawn by a dashed black box. **b**, Polarization Ramen measurement. **c**, MIM image. Edges and cracks are shown by thin white lines and contacts are labelled by number.

After knowing the critical details of the monolayer WTe_2, we use a probe with a two-axis rotator to measure magnetoresistance. In the experiment, the device is rotated and the direction of magnetic field ($\boldsymbol{B}$) is always fixed. Our results are given as a function of the angle of $\boldsymbol{B}$ relative to the device, defined by the polar angle θ' and azimuthal angle φ' as shown in the Fig. 3.8a. We cooled down the device MW5 to 4 K and set $V_g = -2.7$ V to eliminate the bulk conduction. Figure 3.8b shows the raw data for device MW5 when φ' is stepped and θ' is swept at $B = 3$ T and $T = 4$ K. A strong anisotropy of edge conductance in the direction of $\boldsymbol{B}$ is observed. The conductance is maximum when $\boldsymbol{B}$ is in the y-z mirror plane and tilted from the z-axis.

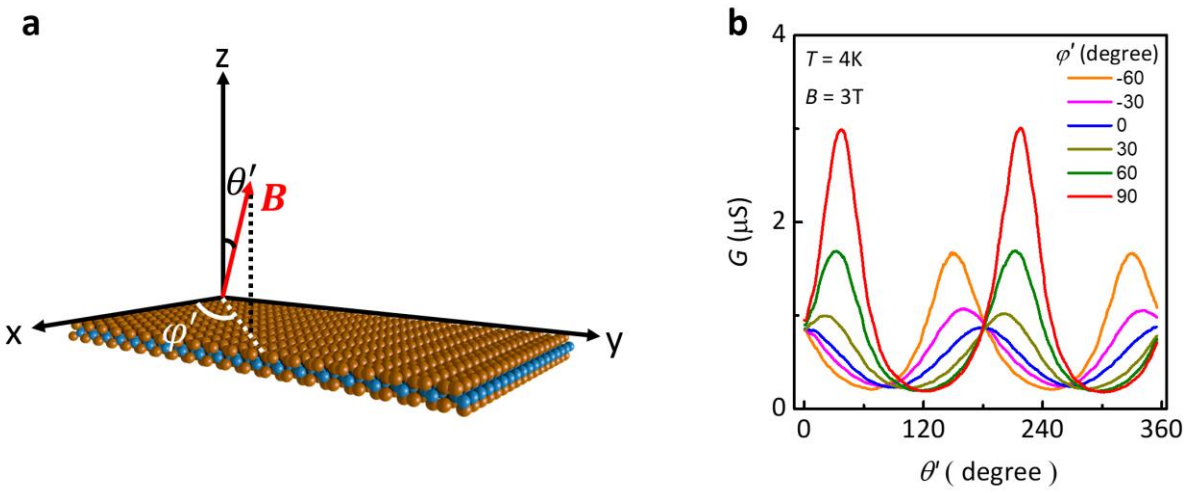

Figure 3.8. Raw data of magnetoresistance of the device MW5. **a**, Illustration of φ' and θ' according to the crystal axes of monolayer WTe_2 (W, blue and Te, orange). **b**, Linear conductance between two adjacent contacts as a function of θ' at different values of φ' at $B = 3$ T.

By considering the symmetry of monolayer WTe_2, the z-axis is not a special axis. In contrast, the x-axis is both the screw axis, and perpendicular to the y-z mirror plane. So, we choose the x-axis as the polar axis to present the result. The direction of $\boldsymbol{B}$ is redefined by polar angle θ and azimuthal angle φ as shown in the Fig. 3.9a. Interpolated data is shown by a color surface plot in Fig. 3.9b. The magenta lines are raw data as shown in Fig.3.8b. Then, by fixing φ, G as a function of θ can be read out followed by smoothing of 20 points. As summarized in Fig. 3.9c, G is maximum at $\varphi = \varphi_s, \theta = 90°$, where in this case $\varphi_s = 38°$, i.e., when $\boldsymbol{B}$ is in the mirror plane at 38° to the z-axis. Onsager symmetry requires $G(\theta, \varphi) = G(\theta + 180°, \varphi)$. Another symmetry which is $G(90° + \theta, \varphi) = G(90° - \theta, \varphi)$ can be found in Fig. 3.9c, i.e. the effect of $\boldsymbol{B}$ is symmetric about the mirror (y-z) plane. Note that the distorted shape of the red curve in Fig. 3.9c is due to uncertainty of the angular measurement in the raw data. We call the special direction of

$\boldsymbol{B}$ in which G is maximum as $\boldsymbol{d_{so}} = (\theta = 90°, \varphi_s)$. As discussed in toy model, $\boldsymbol{d_{so}}$ can be understood as the spin axis of the QSH state of monolayer WTe_2.

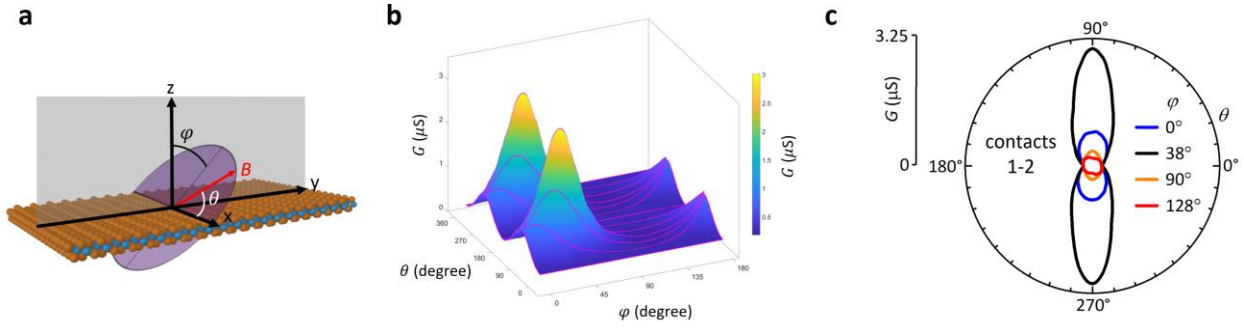

Figure 3.9. Interpolated data of magnetoresistance of device MW5. **a**, Illustration of φ and θ according to the crystal axes of monolayer WTe_2 (W, blue and Te, orange). **b**, Color surface plot of interpolated data. The magenta lines are raw data as shown in Fig. 3.8b. **c**, Two-terminal conductance G as a function of θ at different φ.

3.4 Rigidity of the spin axis

We measured $\boldsymbol{d_{so}}$ for several edges of device MW5 as plotted in Fig. 3.10. From the MIM image (Fig. 3.7c), the shape, length, and orientation of different edges changes dramatically. Because the y-z mirror plane is special for monolayer WTe_2, $\boldsymbol{B}$ is swept in this plane and φ_s is measured for different edges. Edge should almost break spatial symmetry of monolayer WTe_2, and we might expect φ_s to be sensitive to specifics of the edge. Surprisingly, however, φ_s varies only within 1° among the different edges as shown in Fig 3.10b. Very weak dependence of the spin axis suggests that the edge spin orientation is inherited from the bulk band structure.

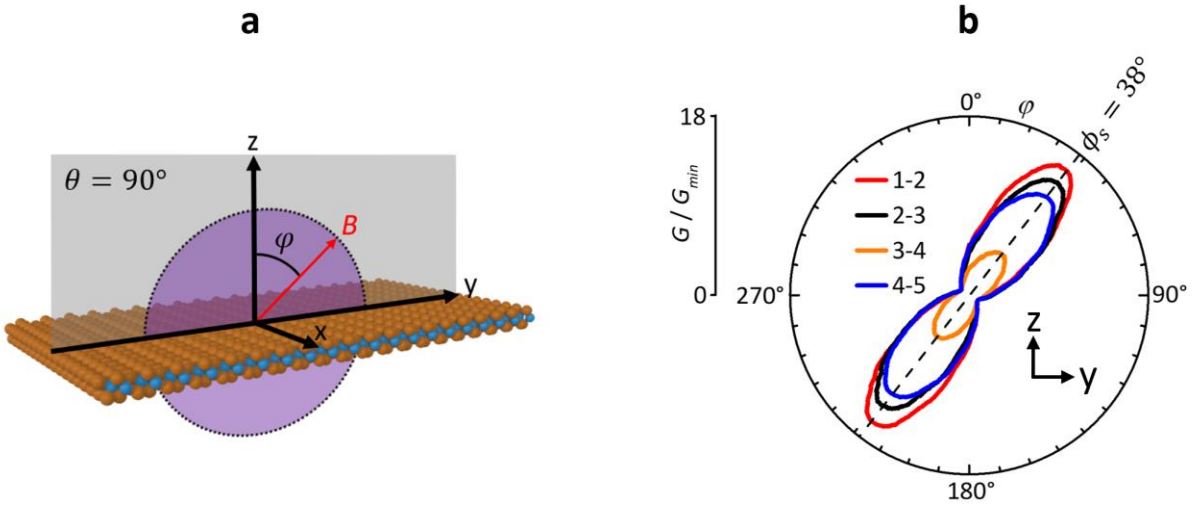

Figure 3.10. Comparison φ_s of different edges. **a**, Schematic of sweeping $\boldsymbol{B}$ in the y-z mirror plane. **b**, Anisotropy of G between different terminals on $\boldsymbol{B}$ in the y-z mirror plane at $|\boldsymbol{B}| = 3$ T and $T = 4$ K. Dashed line indicates the angle maximizing G.

φ_s is also measured at different temperatures, gate voltages (V_g) and magnitude of magnetic field. Figure 3.11 shows G as a function of φ at $B = 3$ T and at a series of temperatures. At 140 K, bulk WTe_2 dominates the conduction and the anisotropy is very weak, indicating that the anisotropy comes from the QSH state, and that the QSH state of monolayer WTe_2 is still present above 100 K. The anisotropy grows on cooling down. As shown in Fig. 3.11b, G drops very slowly with cooling below 50 K at $\varphi = \varphi_s$. In contrast, G drops very fast with cooling at $\varphi = \varphi_s + 90°$. It suggests that a gap opened by $\boldsymbol{B}$ is the largest when $\boldsymbol{B}$ is near perpendicular to $\boldsymbol{d_{so}}$. Figure 3.11c shows the logarithmic plot of G as a function of B at 4 K. G drops much faster when $\boldsymbol{B}$ is perpendicular to $\boldsymbol{d_{so}}$.

It is apparent in Fig. 3.11a that the angular separation, let us call it φ_m, of the minima and maxima of G is not 90° but rather ≈ 85°. This can be understood by including the g-tensor of the edge electrons, which is not constrained by any symmetry. We find that φ_m ranges from 83° to

90° between different devices and contact pairs, consistent with g depending on details of the edge. However, the small variation of $\boldsymbol{d}_{so}$ together with the fact that φ_{m} is close to 90° implies that the g can be treated as a scalar to a first approximation.

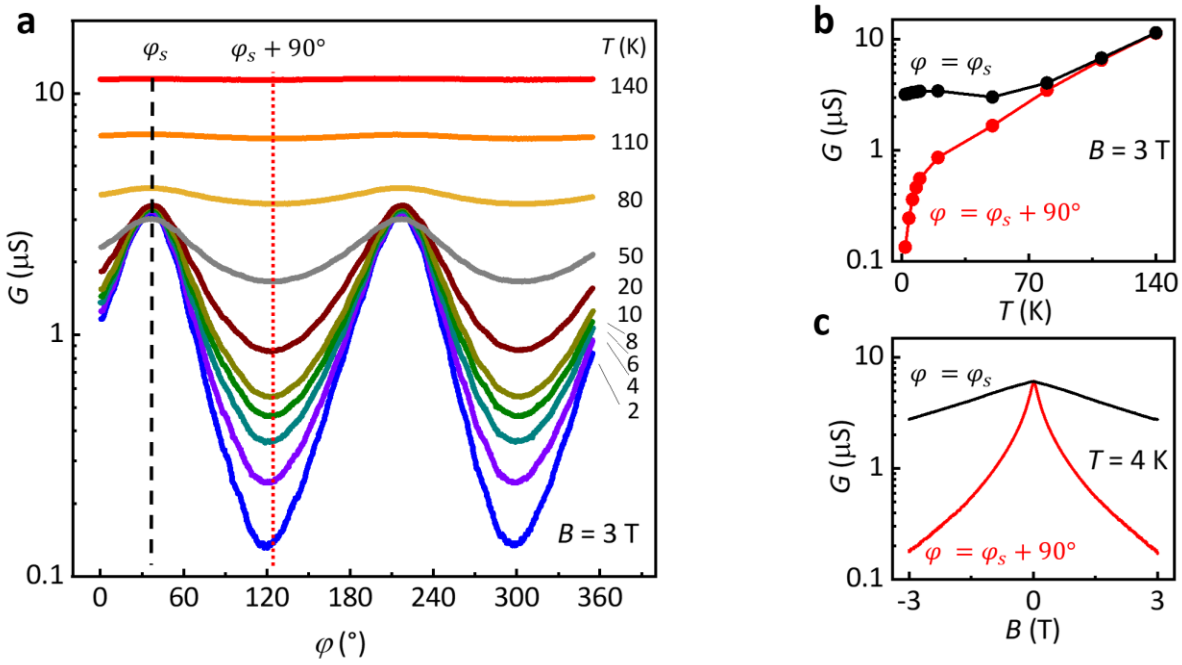

Figure 3.11. Temperature dependence of anisotropy. **a**, Temperature dependence of two-terminal conductance G versus φ in the y-z mirror plane at $B = 3$ T and $V_{\mathrm{g}} = -2.7$ V. **b**, G as a function of T for $\varphi = \varphi_s + 90°$ (red) and $\varphi = \varphi_s$ (black) as reading from panel **a**. **c**, G as a function of B for $\varphi = \varphi_s + 90°$ (red) and $\varphi = \varphi_s$ (black) at $T = 4$ K and $V_{\mathrm{g}} = -2.7$ V.

Figure 3.12a shows G as a function of φ at different V_g. When the bulk is conducting at $V_g =$ 8 V, the anisotropy is the weakest, as expected. Interestingly, the direction of $\boldsymbol{d}_{so}$ changes slightly (within 2°) with V_{g}. Figure 3.12b plots G as a function of φ at different magnitude of $\boldsymbol{B}$. We find that the direction of $\boldsymbol{d}_{so}$ is not changed at all by the magnitude of $\boldsymbol{B}$ in this device.

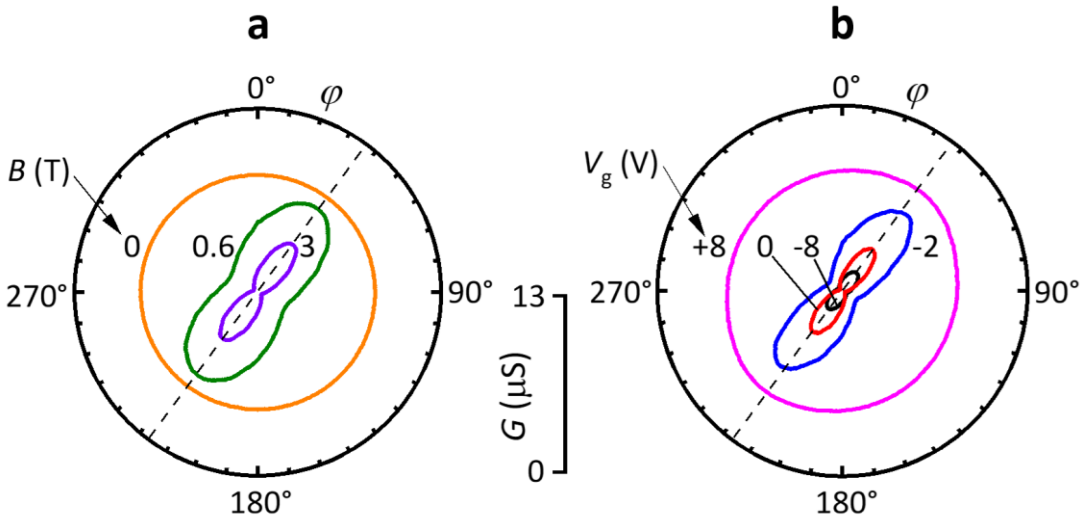

Figure 3.12. Gate and magnitude of $\boldsymbol{B}$ dependence of anisotropy. **a**, Polar plot of G versus φ at $V_g = -2.7$ V and $T = 4$ K for different B. **b**, Polar plot of G versus φ at $B = 3$ T and $T = 4$ K for different V_g. G at $V_g = 8$ V (magenta) is scaled by 1/3.

To find the dominating effect of gate voltage on φ_s, we compare the dependence of φ_s on V_g for two devices MW3 and MW5 as shown in Fig. 3.13. The graphite gate for MW3 is on the top of monolayer WTe_2, whereas the graphite gate for MW5 is on the bottom. Applied voltage on a single gate can change doping and electric field simultaneously. The trends of change of φ_s are opposite for device MW3 and MW5 suggests that φ_s mainly depends on the direction of the electric field. Hence, the dependence of φ_s on V_g can be understood by the Rashba effect induced by the perpendicular electric field.

In summary, we find $\boldsymbol{d_{so}}$ displays little to no dependence on the detail of the edges, temperature, V_g and the magnitude of $\boldsymbol{B}$.

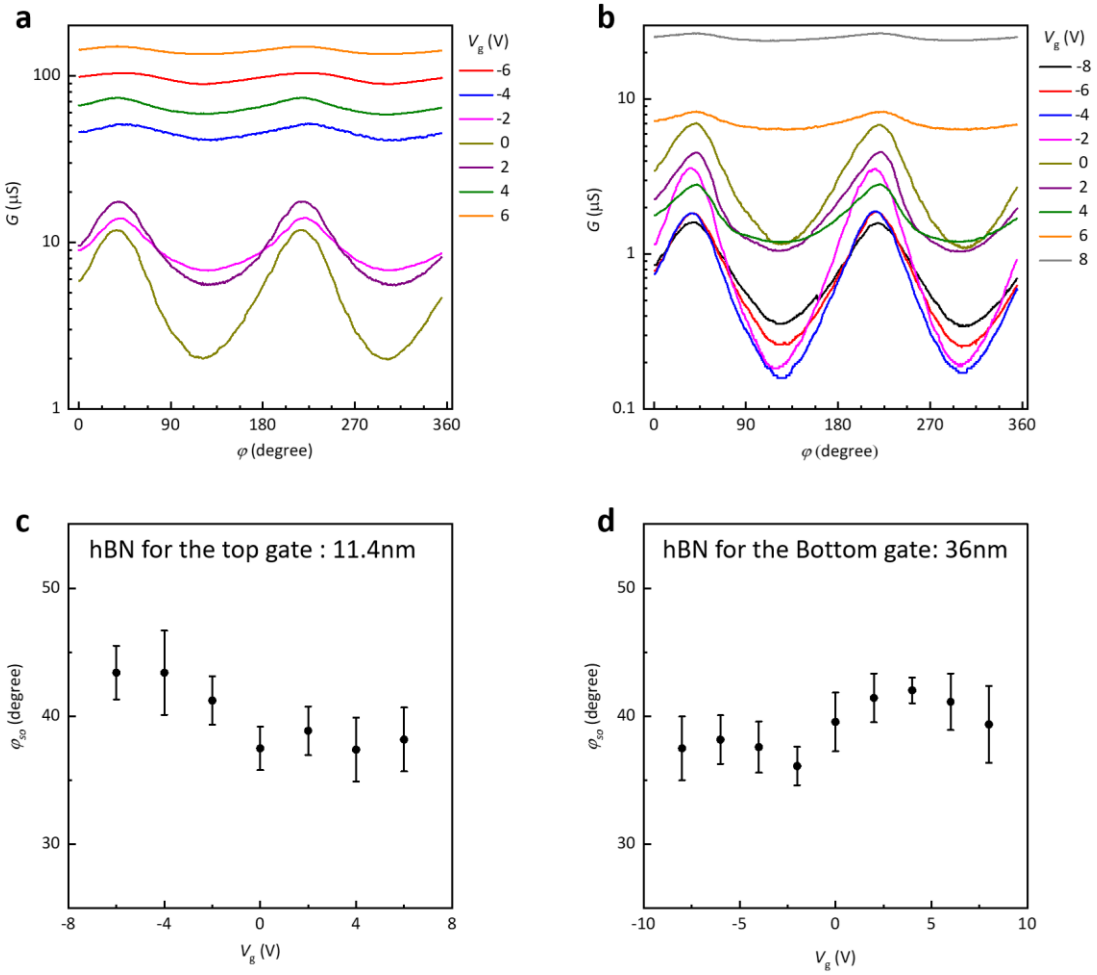

Figure 3.13. The relation of φ_s with gate voltage. **a** and **b**, Linear conductance between two adjacent contacts as a function of φ in the y-z mirror plane for device MW3 and MW5, respectively. $B = 9$ T and $T = 2$ K is used for MW3. $B = 3$ T and $T = 4$ K is used for MW5. **c** and **d**, φ_s as a function of gate voltage V_g for MW3 and MW5, respectively. The gate hBN thickness is labeled in each panel.

3.5 Spin-orbit coupling in monolayer WTe_2

The Hamiltonian of the edge is determined by the boundary conditions and the bulk Hamiltonian of monolayer WTe_2. The bulk spin-orbit coupling plays a fundamental role in the Hamiltonian of a topological insulator. In this section, we show that the leading term in the bulk

spin-orbit coupling in monolayer WTe_2 is of Kane-Mele type, but with the spin axis anywhere in the y-z mirror plane. This direction ends up being $\boldsymbol{d_{so}}$. This way we reproduce the form of the spin-orbit coupling in Ref. (*50*, *51*). This means that the band structure is almost 100% spin polarized, in the sense that one has two interpenetrating band structures with spin orientations along and opposite to $\boldsymbol{d_{so}}$. This immediately implies that the edge states are polarized along and opposite to $\boldsymbol{d_{so}}$.

The unit cell of monolayer WTe_2 is shown in Fig. 3.14. We look at the momentum-independent part of the spin-orbit coupling. If it is non-zero, it dominates the spin physics near the Γ point, but it was also shown in Ref. (*51*) to give a good fit to the first-principle band structure everywhere near the Fermi level. So, we employ the symmetries of the Hamiltonian to deduce the form of the momentum-independent part of the spin-orbit coupling term.

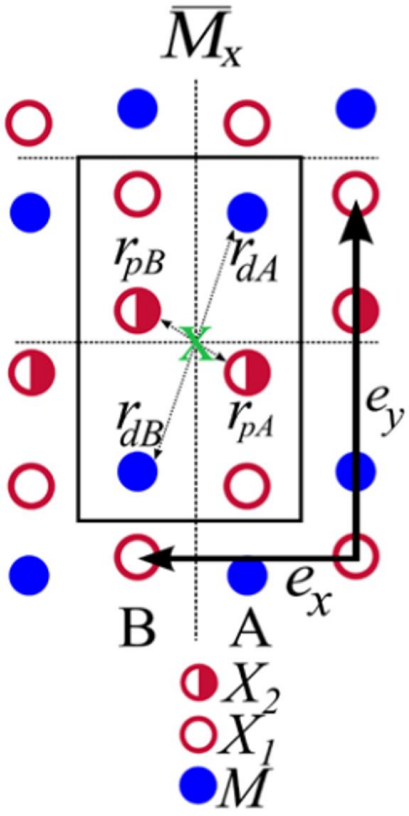

Figure 3.14. Unit cell of monolayer WTe_2.Tungsten atoms are labeled by blue balls. Tellurium atoms are divided in two groups X_1 and X_2. The unit cell is divided into two sublattices labeled by A and B. $\boldsymbol{r}_{l,s}$ is the vector connecting the origin to the center of the X_2 (tellurium atom) or M (tungsten atom), where $l \in \{p, d\}$ band and $s \in \{A, B\}$ sublattice. (Figure taken from Ref. (*51*))

The Hamiltonian must respect time reversal (TR), the glide mirror plane ($\overline{M}_x$), and the screw axis ($\overline{C}_{2x}$) symmetries. Here is what these symmetries do:

- TR: flips spin and momentum, preserves orbital and sublattice indices
- $\overline{M}_x = (x \to -x) + \frac{1}{2}t_x$: flips the sign of the spin component in the y-z plane; preserves the sublattice index, taking the A-site of unit cell (n_x, n_y) into the A-site of cell $(-n_x, n_y)$, and taking the B-site of unit cell (n_x, n_y) into the B-site of cell $(-n_x + 1, n_y)$; flips the sign of the p_x orbital, preserves the sign of the $d_{x^2-y^2}$ orbital.
- $\overline{C}_{2x} = C_{2x} + \frac{1}{2}t_x$: flips the sign of the spin component in the y-z plane; flips the sublattice index, taking the A-site of cell (n_x, n_y) into the B-site of cell $(n_x + 1, -n_y)$, and taking the B-site of cell (n_x, n_y) into the A-site of cell $(n_x, -n_y)$; preserves the orbital index.

If we choose Pauli matrices s, σ, τ to act in the spin, sublattice, and orbital spaces, respectively, the corresponding operators are:

$$TR = s_y \sigma_0 \tau_0 K \tag{37}$$

$$\overline{M}_x = s_x\left[\sigma_0\left(1 + e^{ik_x a}\right) + \sigma_z\left(1 - e^{ik_x a}\right)\right]\tau_z/2$$

$$\overline{C}_{2x} = s_x\left[\sigma_x\left(1 + e^{ik_x a}\right) + i\sigma_y\left(1 - e^{ik_x a}\right)\right]\tau_0/2$$

where K is complex conjugation and a is the length of the unit cell along $\boldsymbol{e_x}$.

The general momentum-independent Hamiltonian can be written as $H_{SO} = \sum_{lmn} \lambda_{lmn} s_l \sigma_m \tau_n$. Demanding that the spin-orbit Hamiltonian must be invariant under these symmetries, $H_{SO} = O^{-1} H_{So} O$ for any operator O from the list of symmetries above, we obtain the following form of the spin-orbit coupling:

$$H_{SO} = \lambda_y s_y \sigma_z \tau_y + \lambda_z s_z \sigma_z \tau_y \tag{38}$$

Note that apart from the spin part, the two terms have identical structure, which means that the entire spin-orbit coupling can be written as

$$H_{SO} = \sqrt{{\lambda_y}^2 + {\lambda_y}^2} (\boldsymbol{d_{so}} \cdot \boldsymbol{s}) \sigma_z \tau_y \tag{39}$$

where $\boldsymbol{d_{so}} = \frac{\lambda_y \boldsymbol{e_y} + \lambda_z \boldsymbol{e_z}}{\sqrt{{\lambda_y}^2 + {\lambda_z}^2}}$ is a vector in the mirror symmetry plane. It is now clear that in the approximation of momentum-independent spin-orbit coupling, all states have a definite spin projection onto $\boldsymbol{d_{so}}$, either along or opposite to it. That means that one really has two anomalous Hall insulators, with the opposite Chern numbers, superimposed in monolayer WTe_2. The two edge states are the corresponding chiral channels, whose spin orientation is inherited from the bulk band structure. The edge Hamiltonian is just

$$H_{edge} = \varepsilon_0(k) s_0 + \varepsilon(k) \boldsymbol{d_{so}} \cdot \boldsymbol{s} \tag{40}$$

which implies edge-independent spin orientation for the helical modes.

The spin axis, which is in the y-z mirror plane, also can be understood by another way. To construct the spin-orbit coupling term, at least 2-orbital base needs to be chosen first. There are two possible ways.

The first choice is that the two orbitals have opposite inversion symmetry (P) at the Γ point (*45*, *52–55*). the leading order allowed SOC terms then have the form

$$H_{so1} = \tau_x(v_x k_y s_x + v_y k_x s_y + v_z k_x s_z) \quad (41)$$

where τ_i and s_i are Pauli matrices for orbital and spin space, and the coefficients v_i have dimensions of velocity. Spin-orbit coupling of this form projected into edge modes will produce an orientation- and momentum-dependent spin axis that is not in the y-z mirror plane.

The second choice is that the two orbitals have the same *P* at the Γ point (*51*, *56–58*). The matrix elements connecting them must then be even under TR and P, and odd under M_x (and C_{2x}). In this case, we find that the leading-order SOC terms have the form

$$H_{so2} = \tau_y(\lambda_y s_y + \lambda_z s_z) \quad (42)$$

which agrees with equation (38).

Therefore, we conclude that our results support the scenario in which the two bands closest to the Fermi level in $1T'$ WTe_2 have the same inversion symmetry.

3.6 Nonreciprocal measurements

Onsager symmetry is required in near-equilibrium conditions but not in the nonlinear regime, where higher order signal can contribute to total response, so nonlinear conductance can yield additional information. We find that the nonlinear edge conductance depends on the direction of magnetic field with respect to $\boldsymbol{d_{so}}$, as well as the polarization of current, i.e. the QSH state of monolayer WTe_2 has unidirectional magnetoresistance (UMR) (*59*, *60*). Figure 3.15a shows two-terminal $I-V$ traces for device MW5 at $T = 5.5$ K. When $\boldsymbol{B}$ is not perpendicular to $\boldsymbol{d_{so}}$ (for example, $B \parallel$ z-axis), the $I-V$ trace is different for $+0.3$ T and -0.3 T. The current has a component that is even in V which changes sign when $\boldsymbol{B}$ is reversed, i.e. with the form of V^2B.

When $\boldsymbol{B}$ is near perpendicular to $\boldsymbol{d_{so}}$, this component is not resolved in our measurement. Figure 3.15b shows the difference between I_{dc} measured with the magnetic field at $+0.3$ T and -0.3 T.

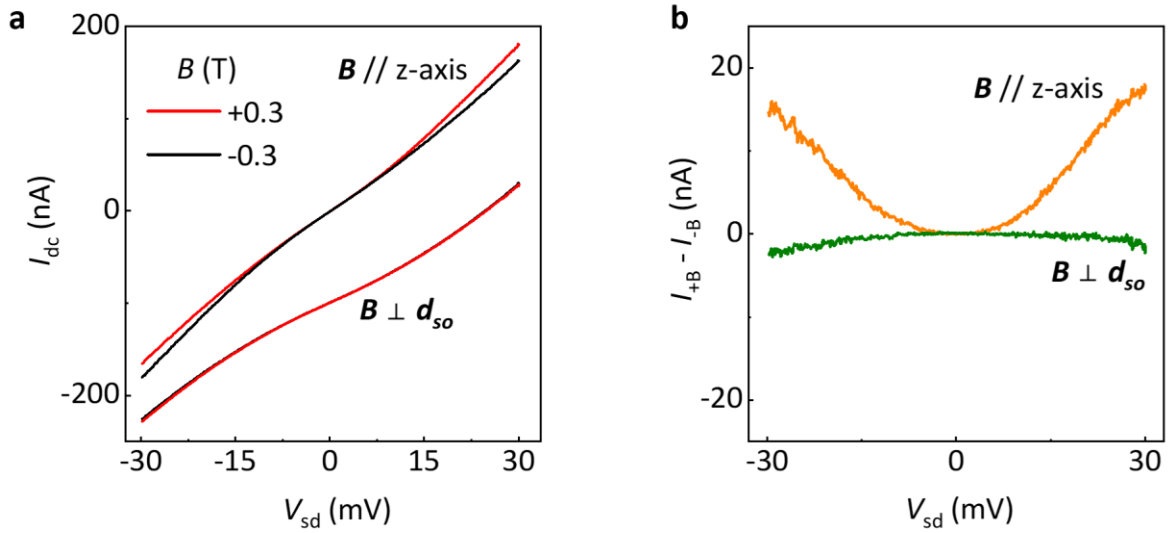

Figure 3.15. $I-V$ traces at positive and negative magnetic field. **a**, $I-V$ traces at $B=\pm 0.3$ T, $T=$ 5.5 K, and $V_{\mathrm{g}}=-2.7$ V for device MW5. Traces are vertically offset for clarity. **b**, The difference between current at $+B$ and $-B$ in panel **a** as a function of bias.

Then we applied an a.c. bias of amplitude V_f at frequency $f=101$ Hz and measured the resulting a.c. current components at f and $2f$, with V_f chosen such that $I_{2f} \ll I_{1f}$. Then we can write $I=GV+\alpha V^2+\cdots$ where $I_{1f}=GV_f$ and $I_{2f}=\alpha V_f^2/2$. The coefficient α parameterizes the conductance asymmetry between positive and negative bias directions. Measurements of G and α vs B when $\boldsymbol{B}$ is parallel to the z-axis for device MW7 is shown in Fig. 3.16a. G is symmetric about $B=0$ and suppressed by B, as expected. α has a heartbeat shape which is antisymmetric about $B=0$ and is almost 0 when B exceeds some value. In the small B regime, α is linear with B. For moderate values of B, α drops as the QSH state is broken by $\boldsymbol{B}$. The MIM image of device MW7, as shown in the inset of Fig. 3.16a, shows a series of edges without cracks from terminal 1

to 4. The bias was applied in the same orientation (clockwise) for each measurement of α. The heartbeat swings the same way. Therefore, the nonlinear behavior is "chiral''. Next, we measured the $\boldsymbol{B}$-odd part of the quadratic coefficient, $\alpha_a = \alpha(\boldsymbol{B}) - \alpha(-\boldsymbol{B})/2$, as a function of φ in the y-z mirror plane and at different temperatures. G is plotted on the top part and α_a is plotted on the bottom part in Fig. 3.16b. Most dramatically, when α_a is 0, I_{1f} is at a minimum which means that $\boldsymbol{B}$ is near perpendicular to $\boldsymbol{d_{so}}$. The magnitude of α_a gets smaller as the temperature increases. At 50 K, α_a is not measurable and anisotropy of G is very weak.

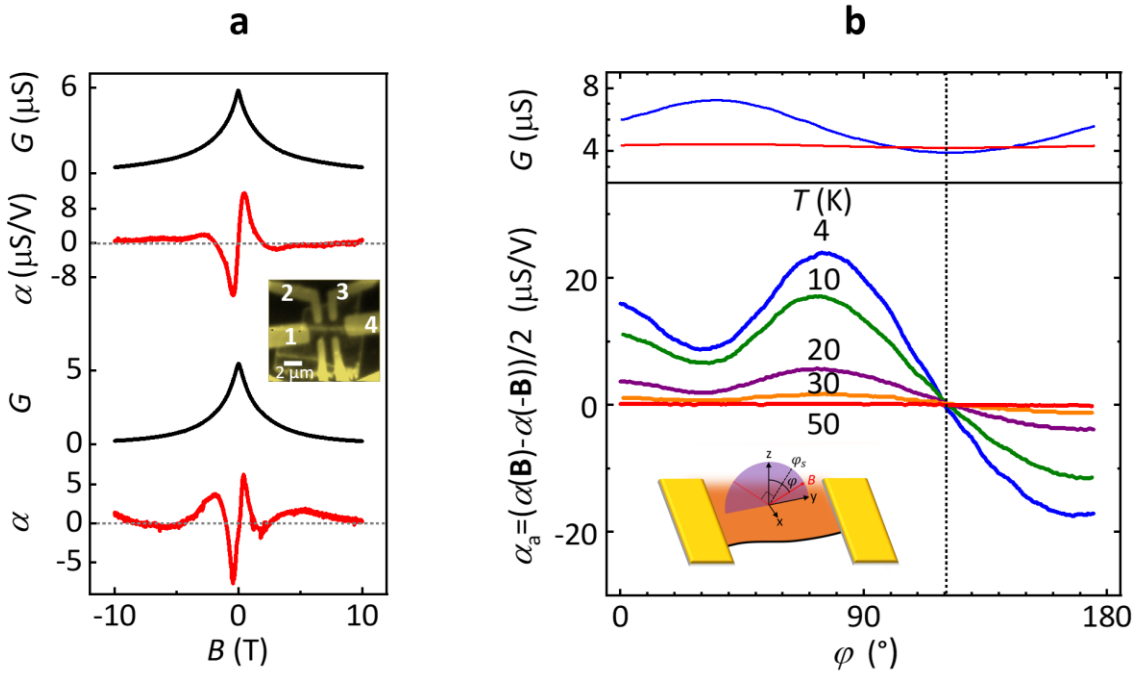

Figure 3.16. Dependence of nonlinear behavior on $\boldsymbol{B}$ and φ. **a**, First-harmonic response G (black traces) and second-harmonic response α (red traces) versus B for $\boldsymbol{B}$//z-axis for terminal 1-2 and 3-4 of device MW7 at $V_g = 0$. Inset shows microwave impedance microscope image of device MW7. The contacts are labeled by number. **b**, G and α_a versus φ in the y-z mirror plane at $V_g = -2.7$ V, $B = 0.3$ T and a series of temperatures for device MW5. Black dashed line indicates the position of the minimum G.

The dependences of G and α_a on the direction of $\boldsymbol{B}$ when $\boldsymbol{B}$ is rotated in other planes are shown in Fig. 3.17. Even though the shape of α_a depends on φ' (θ' and φ' defined by Fig. 3.8a), α_a is always 0 when G is close to its minimum.

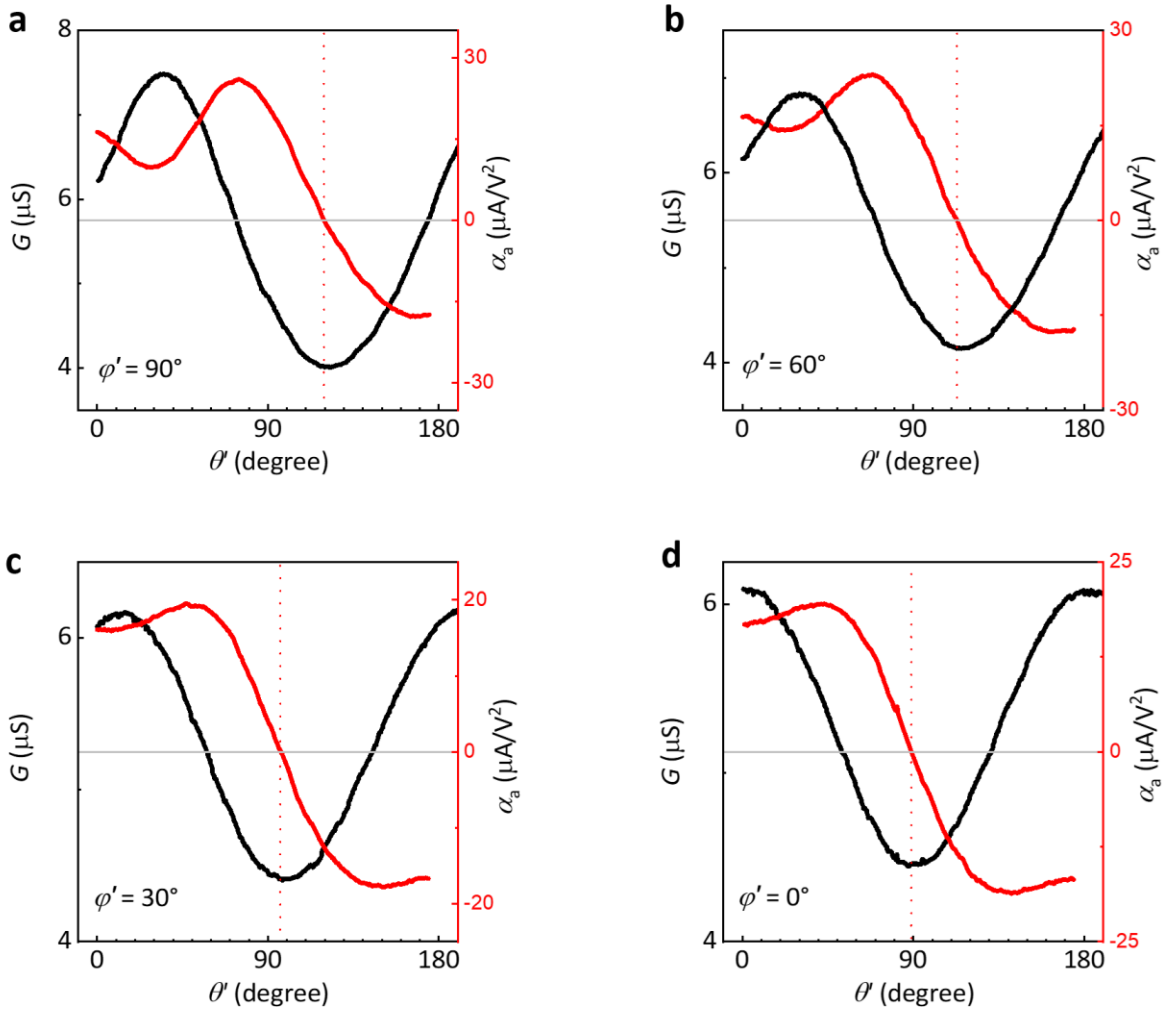

Figure 3.17. Nonlinear measurement at different value of φ' for device MW5. **a-d**, First harmonic response (black) and second harmonic response (red) as a function of θ' when $B = 0.3$ T, at $\varphi' = -90°, -60°, -30°, 0°$, respectively. Red lines indicated zero of γ_a.

The UMR has been previously observed in the surface state of a 3D topological insulator under $\boldsymbol{B}$ (*59*), where it was explained by conversion of a non-equilibrium spin current into a charge current under application of $\boldsymbol{B}$. The fact that I_{2f} is zero when $\boldsymbol{B}$ is perpendicular to $\boldsymbol{d_{so}}$ can be

explained by this scenario, though it cannot explain the two maxima when $\boldsymbol{B}$ is close to $\varphi = 0°$ (the y-axis) and $\varphi = 90°$ (the z-axis) as shown Fig. 3.16b. Another possible explanation considers the exchange field produced by electron-electron correlations, which is called current induced spin polarization effect, as shown by the schematic in Fig. 3.18a. Current flow along the edge induces a spin polarization. Via exchange interaction, this polarization induces an additional Zeeman field ($\boldsymbol{B_{ex}}$), which acts together with the external magnetic field ($\boldsymbol{B}$).

To obtain a model to fit I_{2f} when an arbitrary $\boldsymbol{B}$ is applied in the y-z mirror plane, we need to take a gradient of the linear conductance. We have

$$I(t) = G(\boldsymbol{B} + \boldsymbol{B_{ex}})V_0 \sin(\omega t) \tag{43}$$

$$\approx G(\boldsymbol{B})V_0 \sin(\omega t) + (\frac{\partial G}{\partial B}(\boldsymbol{e_B} \cdot \boldsymbol{B_{ex}}) + \frac{1}{B}\frac{\partial G}{\partial \varphi}(\boldsymbol{e_\varphi} \cdot \boldsymbol{B_{ex}}))V_0 \sin(\omega t)$$

where V_0 and ω are the magnitude and frequency of bias, $\boldsymbol{e_B}$ and $\boldsymbol{e_\varphi}$ are directions shown in Fig. 3.18a. Because we have

$$\boldsymbol{B_{ex}} \propto I_{1f} \sin(\omega t)\, \boldsymbol{d_{so}} = G(\boldsymbol{B})V_0 \sin(\omega t)\boldsymbol{d_{so}} \tag{44}$$

we obtain the following relation for the second harmonic current:

$$I_{2f} \propto -\frac{1}{2}I_{1f}(\frac{\partial I_{1f}}{\partial B}\cos(\varphi - \varphi_s) - \frac{1}{B}\frac{\partial I_{1f}}{\partial \varphi}\sin(\varphi - \varphi_s))\cos(2\omega t)) \tag{45}$$

We can measure the B dependence of conductance at a series of φ to get the value of I_{2f}, $\frac{\partial I_{1f}}{\partial B}$ and $\frac{\partial I_{1f}}{\partial \varphi}$, then calculate I_{2f}. Comparison of calculated I_{2f} (black dashed line) and directly measured I_{2f} (red dots) is shown in Fig. 3.18b and c.

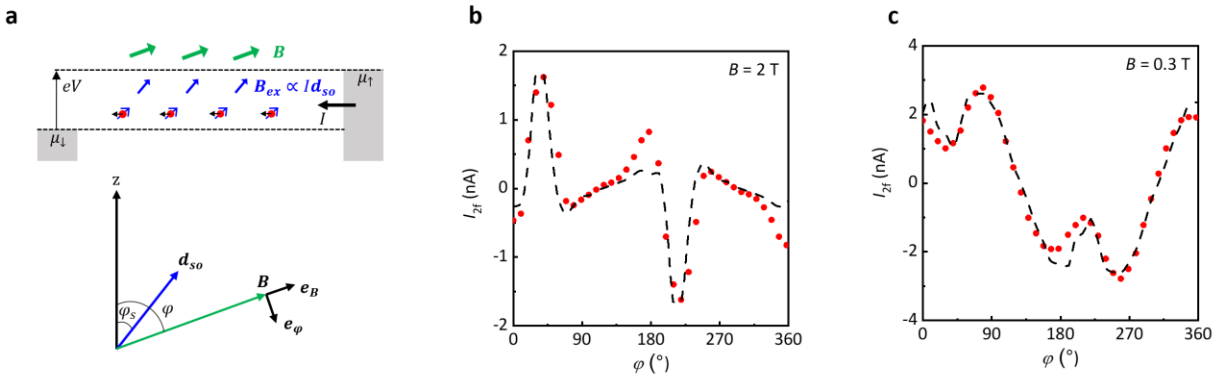

Figure 3.18. Model and fitting of the second harmonic current. **a**, Current induced spin polarization model. Electrons flowing along the QSH edge are drawn as red balls with spin direction and moving direction indicated by blue and black arrows, respectively. The direction of the external magnetic field is shown by the green arrow. **b**, Fitting of the second harmonic current by the equation (45) at $B = 2$ T. **c**, Fitting of the second harmonic current by the first term of equation (45) at $B = 0.3$ T. Black dashed lines are calculated I_{2f} and red points are measured I_{2f}.

While equation (45) fits well to the higher field data in Fig. 3.18b, it fails to capture the lower field behavior. The reason could be that the approximation requires $\boldsymbol{B_{ex}}$ to be much smaller than $\boldsymbol{B}$, or perhaps that two mechanism discussed above mixed up at small magnetic field. But practically we can get a good fitting by the first term ($I_{1f}\frac{\partial I_{1f}}{\partial B}\cos(\varphi - \varphi_s)$) of equation (45), as shown in Fig. 3.18c.

3.7 Control experiment: bilayer WTe_2

To prove that the anisotropy of the magnetoconductance and the nonlinear effect are rooted in the edge of monolayer WTe_2, we conducted similar measurements on bilayer WTe_2, which is topologically trivial and lacks topologically protected edge states. As shown in Fig. 3.19b, first,

the anisotropy of magnetoconductance shows a peak either in $\theta' = 0°$ or $90°$ as the temperature and gate voltage vary, where θ' is the polar angle to the z-axis as shown in Fig. 3.8a. Second, $I - V$ characteristics do not depend on the sign of the magnetic field. There provides the evidence that the topology property of monolayer WTe_2 is the origin of the anisotropy of the magnetoconductance and the nonreciprocal effect.

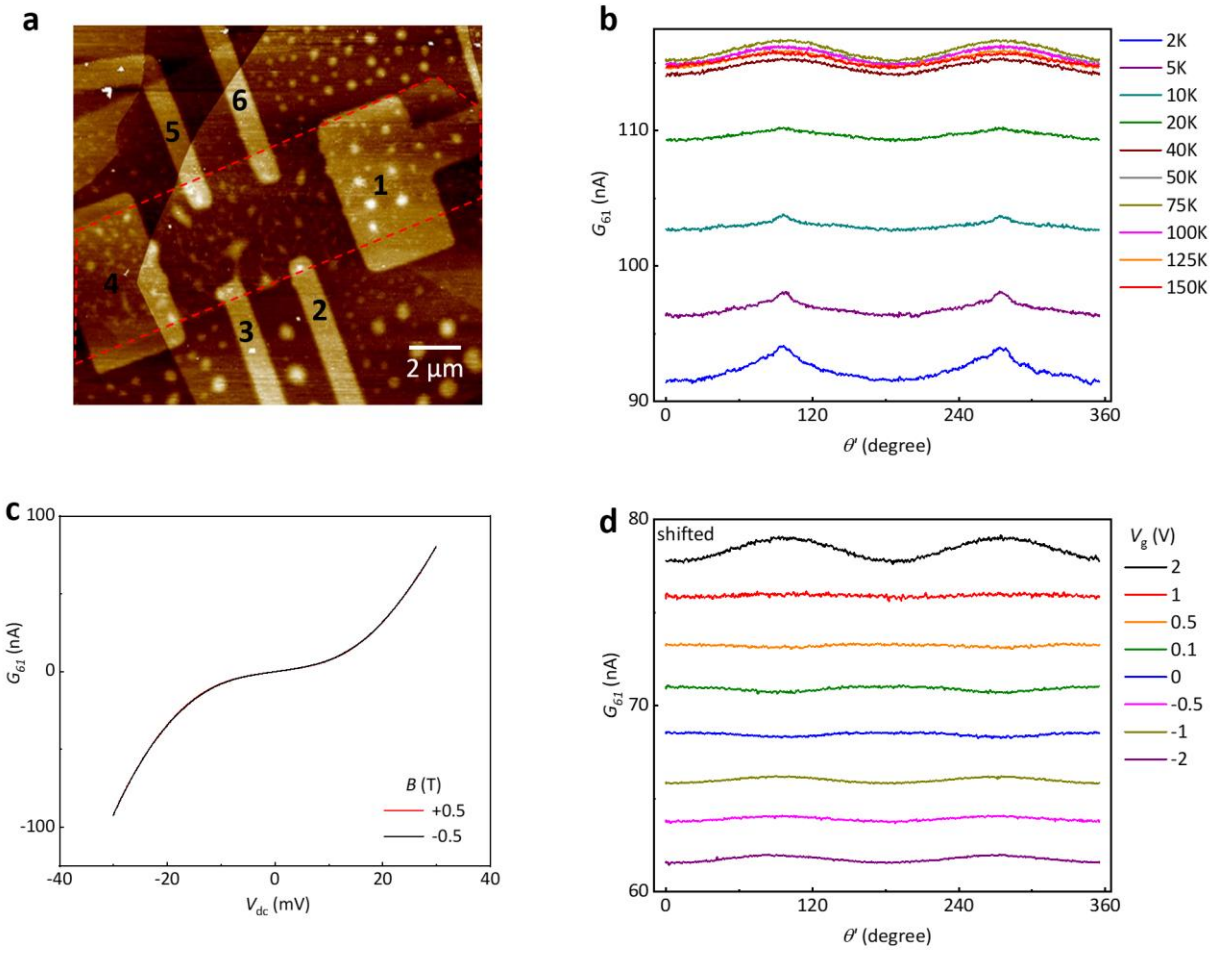

Figure 3.19. Measurement of bilayer WTe_2 device BW7. **a**, AFM image of device BW7. The bilayer WTe_2 flake is outlined by the red dashed line. **b**, Temperature dependence of the two-terminal conductance between contacts 1 and 6, G_{61}, on θ' at arbitrary φ'. The traces are vertically offset for clarity. **c**, $I - V$ characteristics at $T = 2$ K, $B = +0.5$ T (red) and -0.5 T (black). **d**, Gate

dependence of the two-terminal conductance on θ' at arbitrary φ'. The traces are vertically offset for clarity.

3.8 Conclusion and future outlooks

In this chapter, we demonstrated the helical nature of monolayer WTe_2 as the quantum spin Hall (QSH) insulator. Edge conduction was discussed first, with strong anisotropy of edge conductance in a magnetic field indicating a special direction of the QSH edge state. Near-invariance of the special direction to details of the edge, gate voltage, temperature, magnitude of magnetic field can be explained by introducing a momentum independence spin-orbit coupling to the Hamiltonian. A nonreciprocal current was also discussed which is rooted in the topology of monolayer WTe_2. A control experiment with bilayer WTe_2 supports the special direction and nonreciprocity are the properties of edge state of monolayer WTe_2. In summary, we found the spin axis of the QSH edge state in monolayer WTe_2 is in the y-z mirror plane and tilted about $40 \pm 2°$ from the z-axis.

Both anisotropy and tunneling measurements in shorter edges can provide more information. By carefully designing different gate regions, a junction of intrinsically superconducting (*26*, *27*) monolayer WTe_2 and the QSH state of a single flake can be studied in the future.

For theoretical point of view, our findings help to establish the correct form of the low-energy orbital bases and the spin-orbit coupling, which can provide insight in higher order topology(*61–63*), Weyl phenomena(*17*) and unconventional superconductivity(*26*, *27*).

Chapter 4. Magnetic proximity effect in a monolayer WTe_2 helical edge

Magnetism and topology are two important topics in condensed matter physics. Introducing magnetic order into a topology insulator can produce novel phenomena, such as quantum anomalous insulators (*64*) and the nonreciprocal magnetoelectric effect (*60*). In this Chapter, I will discuss the magnetic proximity effect between a 2D magnet and a 2D topological insulator, which is realized by a heterostructure of few-layer CrI_3/monolayer WTe_2.

4.1 CrI_3: 2D magnet

Atomically thin CrI_3 was the first monolayer ferromagnet to be discovered, with its magnetic order probed by the polar magneto-optical Kerr effect (MOKE) (*65*) and reflective magnetic circular dichroism (RMCD) (*66*). Where the monolayer has in-plane ferromagnetic order, its layers couple antiferromagnetically. Figure 4.1 summarizes the out-of-plane magnetic field dependence of MOKE and RMCD for monolayer to four-layer CrI_3 below its critical temperature (about 45 K).

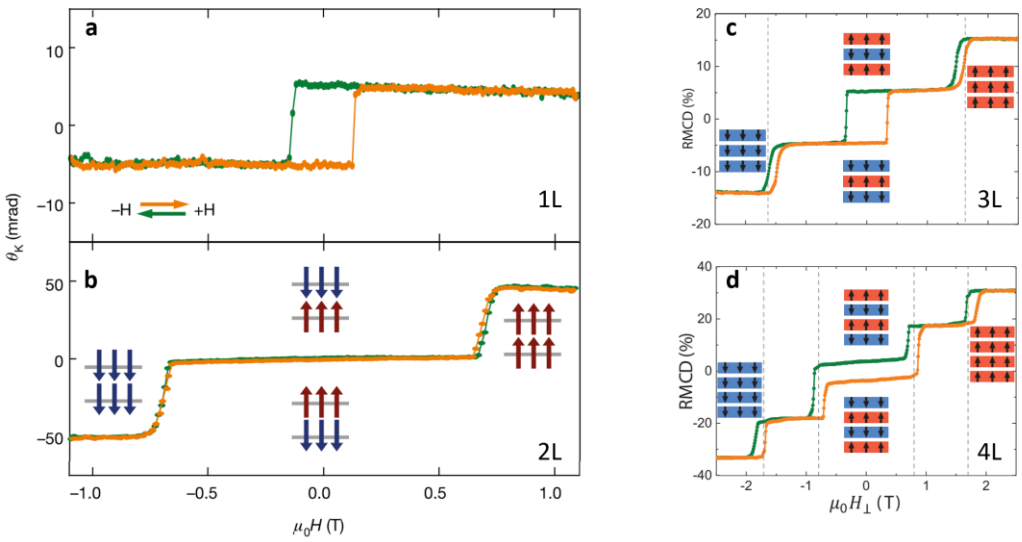

Figure 4.1. Layer-dependence magnetic ordering in 2D CrI_3 .**a** and **b**, MOKE signal of a monolayer and bilayer CrI_3. **c** and **d**, RMCD signal of a trilayer and four-layer CrI_3. Cartoons show the corresponding magnetic states. (Panels **a** and **b** are from Ref. (*65*); panels **c** and **d** are from Ref. (*66*))

The strength of either the MOKE or RMCD signals are proportional to the total out-of-plane magnetization. The hysteresis loop is observed in all thicknesses from monolayer to four-layer CrI_3. In CrI_3 the ferromagnetic moments in each layer align out-of-plane as the cartoons in Fig. 4.1 shown. From bilayer to four-layer CrI_3, adjacent layers are antiferromagnetically coupled. By applying an out-of-plane magnetic field, the magnetic order is reconfigured at a critical field. In the trilayer CrI_3 case for example, while the field sweeps from 2 T to -2 T, the magnetic state first transitions from having ferromagnetic order (↑↑↑) to antiferromagnetic order (↑↓↑) at around 1.8 T, where the arrow represents the direction of magnetic moment in each layer. Then a transition happens around -0.5 T from ↑↓↑ to ↓↑↓. Finally, the state transits from ↓↑↓ to ↓↓↓. The time-reversed process happens when the magnetic field is swept back from -2 T to 2 T.

4.2 Magnetic proximity effect

The proximity effect can occur when two different materials are in intimate contact. When one material is magnetic for example, the other can acquire magnetism by the magnetic proximity effect. The dominant magnetic energies are:

- exchange interaction: $-J_{ij}\boldsymbol{s_i}\cdot\boldsymbol{s_j}$;
- interaction between orbital wave function and the local electric field from neighboring ions (crystal field);
- spin-orbit coupling: $\frac{g}{2}\frac{e}{m^2c^2}\frac{1}{r}\frac{\partial V(r)}{\partial r}\boldsymbol{s}\cdot\boldsymbol{l}$;
- magnetic dipolar interaction: $\sim -\frac{1}{r^3}(3(\boldsymbol{s_1}\cdot\hat{\boldsymbol{r}})(\boldsymbol{s_2}\cdot\hat{\boldsymbol{r}})-(\boldsymbol{s_1}\cdot\boldsymbol{s_1}))$.

where $\boldsymbol{s}$ and $\boldsymbol{l}$ are the spin and angular momentum of the electron. The exchange interaction is short range and magnetic dipolar interaction is long range (*67*).

Previous experiments using thin film deposition of EuS, a ferromagnet, have already demonstrated magnetic proximitization to layered materials, e.g. EuS/Bi_2Se_3 heterostructures successfully showed induced ferromagnetism in a topological insulator (*68, 69*). In terms of the possible magnitude of magnetic energy, a greater than 14 T magnetic exchange field was reported in a EuS/graphene heterostructure (*70*). The emergence of 2D magnets has enabled a new way to study the magnetic proximity effect and induce magnetism into other 2D materials (*65*, *71*, *72*). The experiments with CrI_3/WSe_2 heterostructures demonstrated this new route and realized a magnetic exchange field exceeding 13 T (*73–75*).

The combination of topological materials with magnetism provides a basis for exploring novel phenomena such as the quantum anomalous Hall effect (*64*, *76*, *77*) and the nonreciprocal magnetoelectric effect (*60*, *78–80*). We have already discussed monolayer WTe_2 as a two-

dimensional topological insulator (2D TI) in Chapter 3. In the helical edge modes of a 2D TI, spin is locked to momentum. Interaction with magnets can then yield magnetoelectric coupling (*81*). For example, the spin polarization of the edge can be modified by the magnetism, or a current-induced torque can be produced on the magnetization by the spin current following in the edge (*18*, *82*). Also, the edge modes in a quantum spin Hall insulator are protected by time reversal symmetry, which can be broken by magnetic order. Hence, backscattering is enabled, and the conductivity of the edge modes should be modified by a magnet. Furthermore, the gapping of edge modes by a ferromagnet is a vital part of schemes to produce Majorana modes in the helical edges (*83*).

In this chapter, we study the magnetic proximity effect and nonreciprocal current in few-layer CrI_3/monolayer WTe_2 heterostructures. We find that the CrI_3 suppresses edge conduction consistent with increased backscattering as expected. The linear conductance is highly sensitive to the magnetization state of the CrI_3, which is monitored by RMCD measurements. The conductance changes suddenly when either the nearest or next-nearest CrI_3 layer flips polarization, from which we estimate exchange fields of several Tesla. In the nonlinear regime, current-voltage characteristics have an even component with a sign dependent on the magnetization of the adjacent CrI_3 layer. At low temperatures this can produce a very large nonlinear magnetoresistance. Finally, by comparing linear and nonlinear conduction for different contact combinations, we confirm that the magnetization sensitivity is associated with the current flowing at the edge and not in the bulk of monolayer WTe_2.

4.3 Fabrication process of CrI_3/WTe_2 devices

Due to the extreme sensitivity of few-layer CrI_3 to water and oxygen, the fabrication process of CrI_3/WTe_2 devices differs somewhat from the description in Section 2.2, as follows:

1. After evaporation of Pt metal contacts, another step of electron beam lithography and metal deposition is taken for bond pads (60nm Au/6 nm V).
2. CrI_3 flakes are optical identified from bilayer to four-layer.
3. The whole CrI_3 flake should be encapsulated by top and bottom hBN. And it should avoid touching the gold leads.
4. PC film is removed in chloroform bath for only 1 minute.

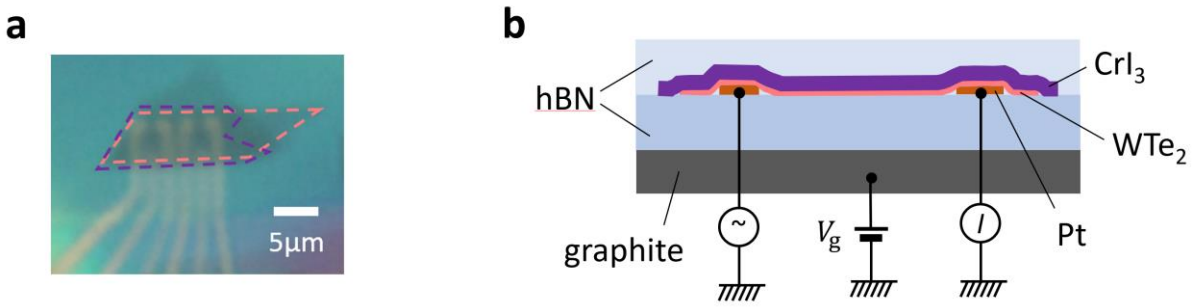

Figure 4.2. Optical image and cross-section of device CW6. **a**, Optical image. The boundary of trilayer CrI_3 and monolayer WTe_2 are depicted by purple and pink dashed lines, respectively. **b**, Schematic device cross-section of a sample with a graphite bottom gate.

An optical image and cross-section of device CW6 are shown in Fig. 4.2. The thicknesses of WTe_2, CrI_3 and hBN in the devices discussed in this chapter are listed in table 4.1.

Device label	WTe_2	CrI_3	Top hBN (nm)	Bottom hBN (nm)
MW3	Monolayer	NA	11.4	25
CW2	Monolayer	Bilayer	12	23.5
CW5	Monolayer	Bilayer	16	37
CW6	Monolayer	Trilayer	20.9	18.3
CW8	Monolayer	Four-layer	17.2	7

Table 4.1. Thickness of WTe_2, CrI_3 and hBN dielectrics.

4.3 Gate dependence with no applied magnetic field

Figure 4.3a shows measurements of the linear conductance G between two adjacent contacts in device CW6, which has trilayer CrI_3 covering most of the monolayer WTe_2 (see optical image in Fig 4.2a). G passes through a minimum near $V_g = 0$ that initially grows deeper on cooling from room temperature, as in bare monolayer WTe_2. However, the minimum conductance, plotted vs temperature T in Fig. 4.3b (black circles), continues to drop steadily down to the lowest T (here 5.6 K). This is fitted to the form $G \propto e^{-\frac{E_a}{k_B T}}$ for $T < T_c$, plotted as the blue dashed line, where k_B is Boltzmann's constant, yielding an activation energy $E_a = 2.5 \pm 0.3$ meV. This differs from the behavior of a typical bare WTe_2 monolayer, plotted in the same figure (red circles), in which G stops dropping below ~40 K once bulk conduction is frozen out and edge conduction dominates.

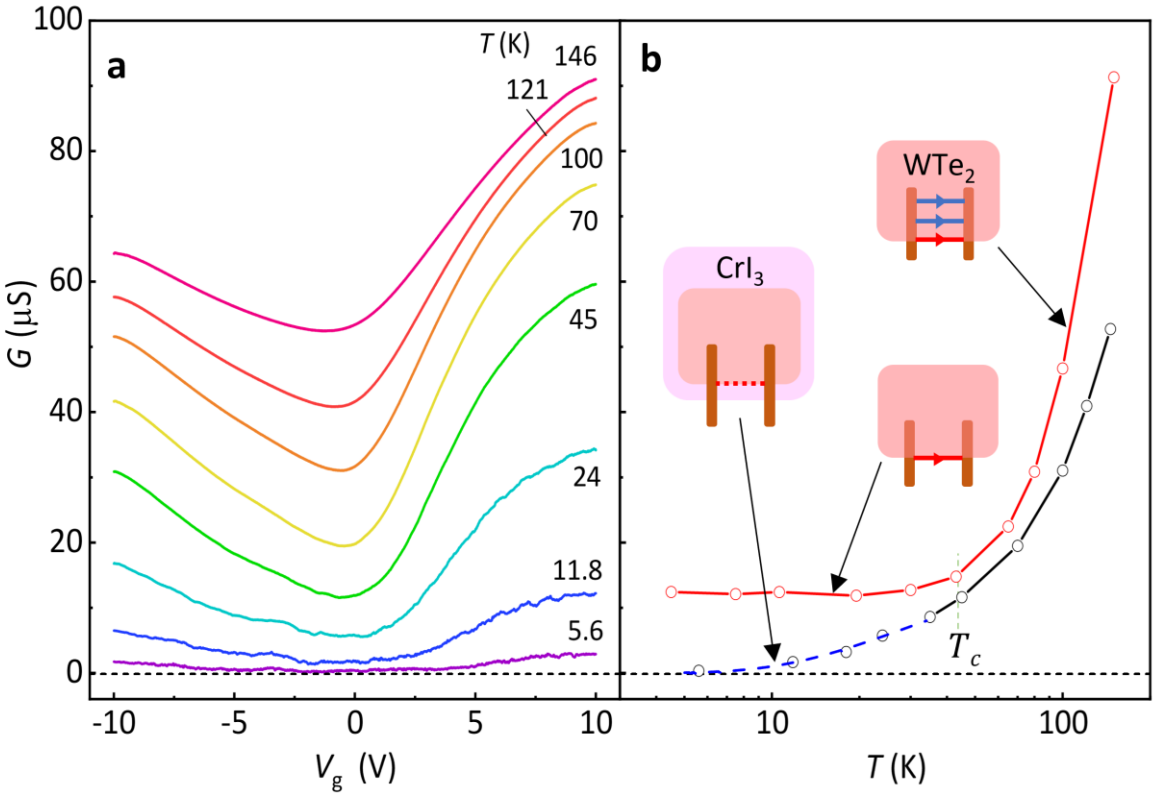

Figure 4.3. Gate dependence with no applied magnetic field. **a**, Gate dependence of the conductance G between a pair of adjacent contacts (L = 0.8 μm, W = 5 μm) at different temperatures for device CW6, which has a trilayer CrI_3. The electron density $n_e = \frac{c_g V_g}{e} = 1.21 \times 10^{12}\ \mathrm{cm}^{-2} * V_g$. **b**, Comparison of the temperature dependence of the minimum G for device CW6 (black) and for a bare (no CrI_3) monolayer WTe_2 device MW3 (red). The insets show bulk and edge currents in each case.

Qualitatively similar behavior was seen in all CrI_3/WTe_2 devices, including device CW2 which has the monolayer WTe_2 only partially covered by a bilayer CrI_3, as shown in Fig. 4.4a. Only edge 14 is not covered by CrI_3 and all other edges are at least partially covered by CrI_3. Above the T_c ($\approx$ 45 K) of bilayer CrI_3, $I-V$ characteristics are similar for all the edges. Edge 14 and 23 have a higher current due to their shorter channel lengths. Below T_c, the current for the uncovered edge, pair 14, is much higher than it for the other three edges.

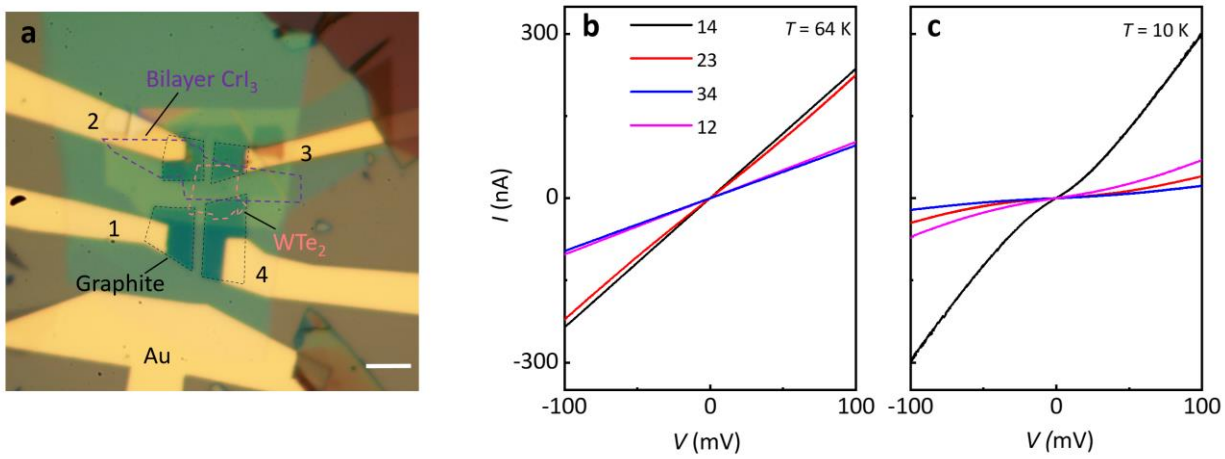

Figure 4.4. Comparison of $I-V$ characteristics for channels with and without CrI_3. **a**, An optical microscopy image of device CW2. Etched graphite contacts, monolayer WTe_2 and bilayer CrI_3 are outlined by black, pink, and purple dashed lines, respectively. Scale bar: 10 μm. **b**, $I-V$ characteristics for each channel at 64 K. **c**, $I-V$ characteristics for each channel at 10 K.

These results suggest that, as anticipated, the magnetization of the CrI_3 suppresses the edge conduction, presumably by breaking the time-reversal symmetry that strongly inhibits backscattering in the helical edge states. A quantitative understanding of this suppression should consider the combined effects of disorder, magnetism, and electron-electron interactions.

4.4 Characteristics in an applied magnetic field

In this section, we focus on the effects of switching the magnetization state of the CrI_3 using a perpendicular magnetic field B. Figure 4.5a shows the linear conductance of CW6 as a function of B and temperature at $V_g = -0.5$ V where edge conduction dominates. B is swept upwards and downwards at each temperature. The upwards traces behave simply as reflections in $B = 0$ of the downwards traces, consistent with time-reversal considerations. At temperatures above T_C~45 K,

G decreases smoothly with increasing B, similarly to the edge conduction in bare WTe_2 (*22*). Below 45 K a jump shows up in the vicinity of 1.8 T. A second jump appears at around 0.5 T at lower temperatures. The positions of these jumps are not affected by gate voltage due to the screening effect of monolayer WTe_2.

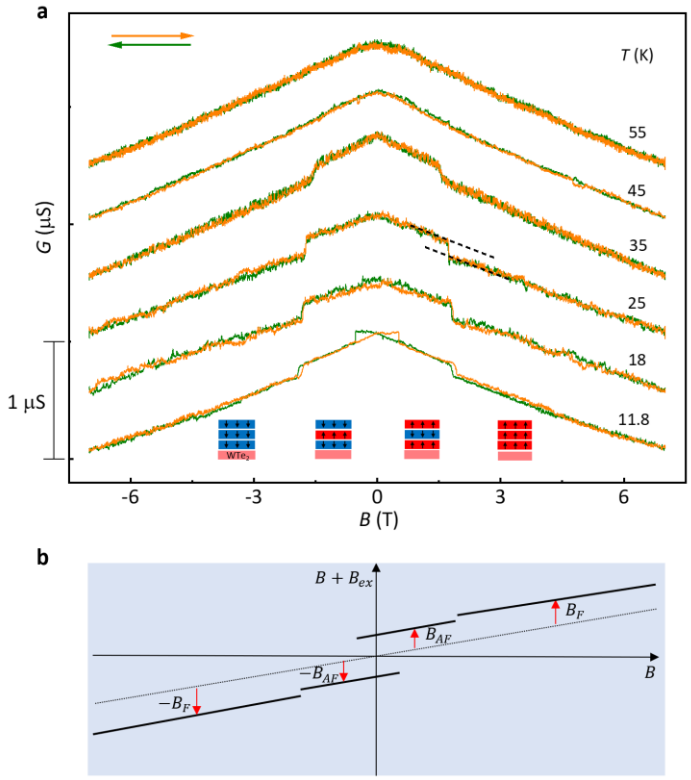

Figure 4.5. Conductance jumps associated with layered magnetic state changes. **a**, The linear conductance as a function of an out-of-plane magnetic field at $V_g = -0.5$ V for device CW6. The dashed black lines indicate the effective shift of G at one of the jumps. Traces are vertically offset for clarity. Schematic shows the corresponding magnetic states of trilayer CrI_3 (red and blue for up and down polarization) on top of monolayer WTe_2 (pink). **b**, Schematic dependence of the sum of real and exchanged magnetic fields on B.

To confirm the jumps in G are due to the magnetization switching of CrI_3, RMCD measurements were done on the same device at a series of temperatures as shown in Fig. 4.6. The

strength of the RMCD signal is proportional to the total out-of-plane magnetization and so the four plateaus in the signal correspond to four distinct magnetic states of trilayer CrI_3 (*66*).

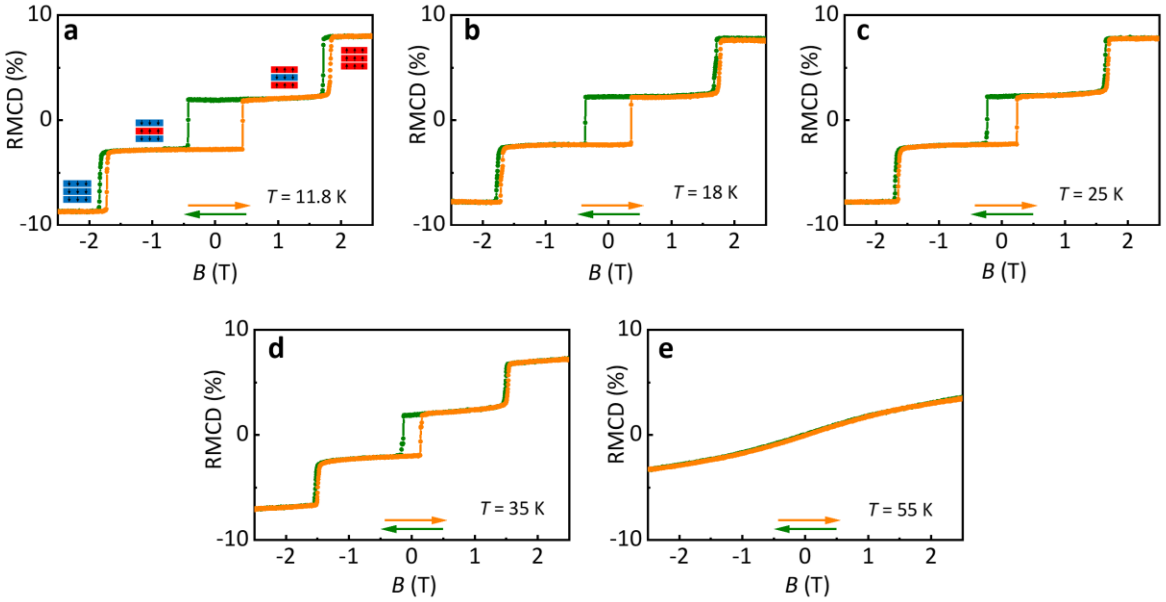

Figure 4.6. Temperature dependence of RMCD traces. **a-e**, RMCD signal as a function of an out-of-plane magnetic field for device CW6 (trilayer CrI_3) at different temperatures as indicated. Schematics in panel **a** show the corresponding magnetic states of trilayer CrI_3.By comparison of the conductance jumps' positions and the RMCD signal, it is clear that the jumps of edge conductance in Fig. 4.5a happen whenever the magnetic state of the CrI_3 changes. The higher-field jumps accompany transitions from antiferromagnetic (AF) to fully polarized (F) states, that is, between ↓↓↓ and ↓↑↓ or ↑↑↑ and ↑↓↑ (using the intuitive notation with the highest layer first). These transitions involve only the spin-flip of the middle CrI_3 layer and so show little hysteresis. The lower-field jumps however accompany transitions between the two antiferromagnetic states, ↓↑↓ and ↑↓↑. This involves a more drastic reconfiguration and so shows large hysteresis.

To explain the conductance jump, we use a simple model in which the WTe_2 experiences an exchange magnetic field B_{ex} that adds to the external magnetic field. So, the conductance of monolayer WTe_2 becomes $G_0(B + B_{ex})$, where $G_0(B)$ is the conductance without CrI_3. The value of B_{ex} is $\pm B_F$ for $\uparrow\uparrow\uparrow$ and $\downarrow\downarrow\downarrow$, and $\pm B_{AF}$ for $\uparrow\downarrow\uparrow$ and $\downarrow\uparrow\downarrow$, respectively. The total field $B + B_{ex}$ then changes B as sketched in Fig. 4.5b. Because $G_0(B)$ is roughly linear with a similar slope before and after the higher-field jump, the value of $B_F - B_{AF}$ can be estimated by the horizontal displacement indicated by the black dotted line for the $T = 25$ K data. Here, we estimate $B_F - B_{AF} \approx +1$ T. The lower-field jump is between $G(B - B_{AF})$ and $G(B + B_{AF})$ and is less clear-cut to analyze. But if we associate the activation energy E_a at zero external field with B_{AF} by $E_a \approx g\mu_B B_{AF}$, where μ_B is Bohr magneton and use a g-factor of $g = 4$, which is estimated from the magnetoresistance of a bare monolayer WTe_2, we can get B_{AF} of ~10 T.

We conclude that the sign of B_{ex} is determined by the polarization of the lowest, proximal layer, while its magnitude is larger or smaller depending on whether the second, next nearest layer has the same (in the F state) or the opposite (in the AF state) polarization.

4.5 Nonreciprocal measurements

In this section, we focus on nonlinear measurements which can provide additional information because nonlinear conductance is not constrained by the Onsager symmetry, as argued in section 3.6. Also, it can be measured at low temperatures when the linear conductance vanishes. For example, Fig. 4.7a shows two-terminal $I - V$ traces at 1.6 K for a bilayer CrI_3 device (CW5), measured with no applied field. No current flows below a threshold bias of ~70 mV in either direction. Above this bias, the current is detectable and depends strongly on B. As shown in the

upper inset to Fig. 4.7a, with 100 mV d.c. bias applied, current exhibits hysteresis with two stable states at low field. At zero magnetic field, two types of $I - V$ traces can be obtained (red and blue), which correspond to the two states shown by blue and red circles. RMCD measurements (lower inset) were measured in the same condition, which connects these to the two antiferromagnetic states, ↑↓ or ↓↑, of the bilayer CrI_3, with a transition to full polarization (↑↑ or ↓↓) occurring above $B \approx 0.9$ T. The sensitivity of I to those two states (↑↓ and ↓↑) is much higher than that of the measured RMCD. The small difference in the RMCD signal between ↑↓ and ↓↑ seen here is typical for CrI_3 bilayers (*84*, *85*) and implies an imbalance in the magnetization density between the two layers, perhaps due to moderate oxidation of one side, or in this case by contact with the WTe_2 on one side. An RMCD spatial map taken at $B = 0$ during a downwards sweep of B shows that there is a single magnetic domain over most of the WTe_2.

Inspection of Fig. 4.7a shows that in the ↑↓ state (blue) the current is larger for positive bias than for negative bias, whereas in the ↓↑ state (red) the opposite is true. In other words, the nonlinear resistance depends on relative orientation of magnetization of the lower CrI_3 layer to the current direction. Such a nonlinear resistance change on magnetization reversal at zero applied magnetic field has been seen in magnetic and nonmagnetic topological insulator heterostructures (e.g. CBST/BST) (*78, 79*). It may also relate to the nonreciprocal effect of the QSH edge state of monolayer WTe_2 in an external magnetic field as discussed in Section 3.6. Note that the change here, of order 100%, is orders of magnitude larger than seen before.

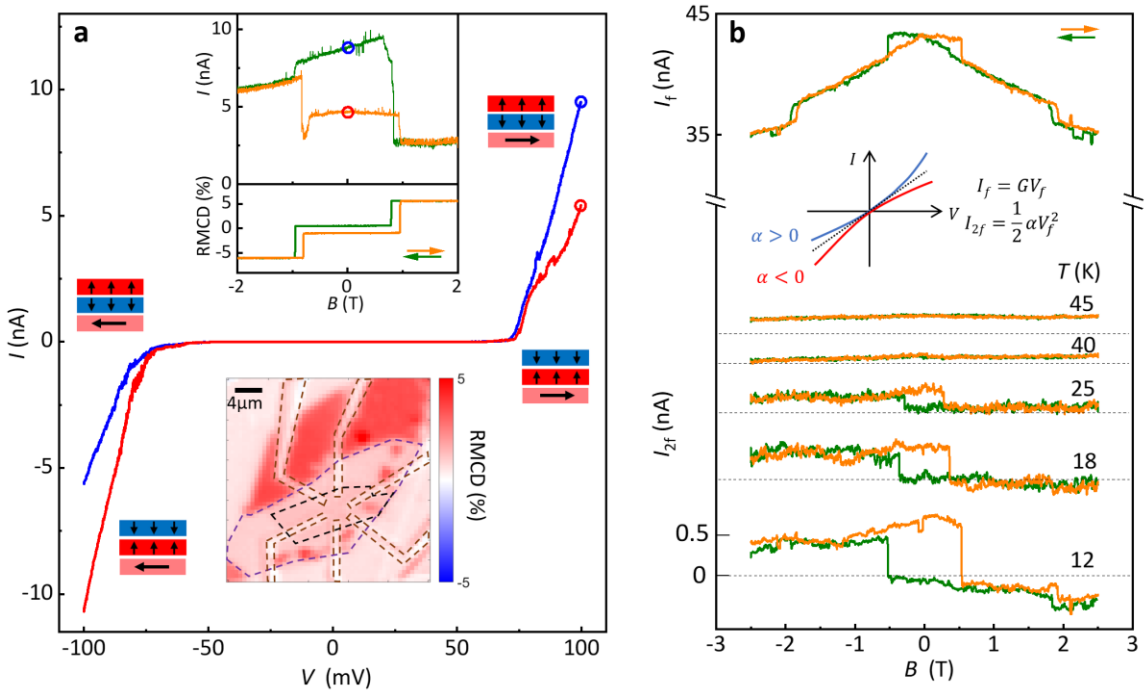

Figure 4.7. Nonlinear measurements. **a**, $I-V$ curve at zero magnetic field at 1.6 K for bilayer device CW5. The cartoons show the magnetization state of the bilayer CrI_3 and the current flow direction of the monolayer WTe_2. The upper inset plots the current at $V = +100$ mV d.c. bias and RMCD signal as a function of an out-of-plane magnetic field. The lower inset shows the spatial map of the RMCD signal at 0 T scanning from +2.5 T. The boundary of Pt contacts, bilayer CrI_3 and monolayer WTe_2 are drawn as dark yellow, purple, and black dash lines, respectively. **b**, The first (I_{1f}) and second (I_{2f}) harmonic response as a function of an out-of-plane magnetic field of device CW6. The blue and red lines in the inset are the exaggerated $I-V$ curves when magnetization of the interface layer CrI_3 points down and up, respectively. The black line is the exaggerated $I-V$ curves without CrI_3. The second harmonic response as a function of an out-of-plane magnetic field at different temperatures at $V_g = -0.5$ V.

We investigate this asymmetry further in the regime of weak nonlinearity at higher temperatures where the linear conductance G is finite. An a.c. bias of amplitude V_f is applied at

frequency f and the resulting a.c. current components at f and $2f$ are recorded. We can write $I = GV + \alpha V^2 + \cdots$ then $I_f = GV_f$, and $I_{2f} = \alpha V_f^2/2$. The measured $2f$ component is proportional to the coefficient α which parameterizes the conductance asymmetry between positive and negative bias directions as indicated in the inset to Fig. 4.7b. At the top of Fig. 4.7b, we plot I_f vs B for device CW6, which matches the a.c. linear conductance measurements in Fig. 4.5a, exhibiting four jumps. Measurements of I_{2f} vs B at selected temperatures are plotted below. Unlike I_f vs B, only a large jump which corresponds to the transition $\uparrow\downarrow\uparrow - \downarrow\uparrow\downarrow$ is observed up to 40 K. When trilayer CrI_3 transitions $\downarrow\downarrow\downarrow - \downarrow\uparrow\downarrow$ or $\uparrow\uparrow\uparrow - \uparrow\downarrow\uparrow$, no discernable features are shown. We conclude that the asymmetry parameter α is controlled by the magnetization of only the lowest layer of CrI_3.

We also use differential conductance (G_{diff}) of a trilayer CrI_3 device CW6 to detect the nonreciprocal effect. As shown in Fig. 4.8a, with either $+15$ mV or -15 mV d.c. bias, G_{diff} shows four jumps as expected. The difference between differential conductance (ΔG_{diff}) at +15 mV and -15 mV d.c. bias as a function of B is plotted in Fig. 4.8b, which only shows two jumps when the transitions between $\uparrow\downarrow\uparrow$ and $\downarrow\uparrow\downarrow$ happen. ΔG_{diff} has a similar dependence of B with I_{2f} in Fig. 4.7b, suggesting that ΔG_{diff} is also mainly controlled by the magnetization of the lowest layer of CrI_3. Indeed, both I_{2f} and ΔG_{diff} measure the asymmetry parameter α.

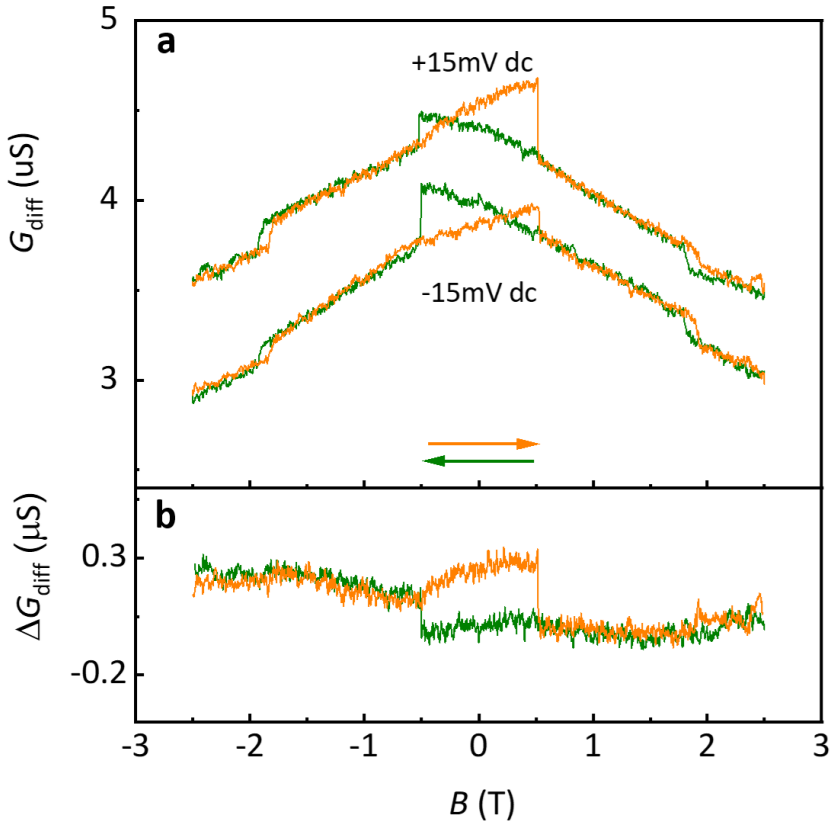

Figure 4.8. Differential conductance for opposite signs of the d.c. bias for device CW6. **a**, Differential conductance (G_{diff}) as a function of B at +15 mV and -15 mV d.c. bias, respectively. The -15 mV traces are offset vertically for clarity. **b**, Difference between the differential conductance (ΔG_{diff}) at +15 mV and -15 mV d.c. bias as a function of B.

In the nonlinear measurements, the larger bias may drive some current through the weakly insulating WTe_2 bulk (*23*), so we performed additional two experiments to distinguish the nonlinear effect of bulk and edge of monolayer WTe_2. First, Fig. 4.9 shows I_f (left panel) and I_{2f} (right panel) vs B for a large a.c. bias of $V_f = 100$ mV applied to a 4-layer CrI_3 device, CW8. The pincer shape contact is used as shown in the sketch on the left. When the middle contact is floated on the top row, edge current can pass and large jumps in both I_f and I_{2f} are observed. However, when the middle contact is grounded to block edge current, I_f is almost independent on B and I_{2f}

is almost zero. This indicates that the sensitivity of I_f and I_{2f} to the magnetic state of the CrI_3 comes from the edge current. Second, Fig. 4.9e&f compare two-terminal measurements of the current in device CW5 for different contact configurations and a large d.c. bias of 100 mV. There is large asymmetry and hysteresis around $B = 0$ for adjacent contacts, whereas the asymmetry and hysteresis are almost gone for contacts on opposite edges. The latter can be explained by the approximate cancellation of nonlinear edge effects on opposite edges of the sample. We conclude that even in the nonlinear regime the sensitivity to the magnetic state of the CrI_3 is dominated by the sample edges.

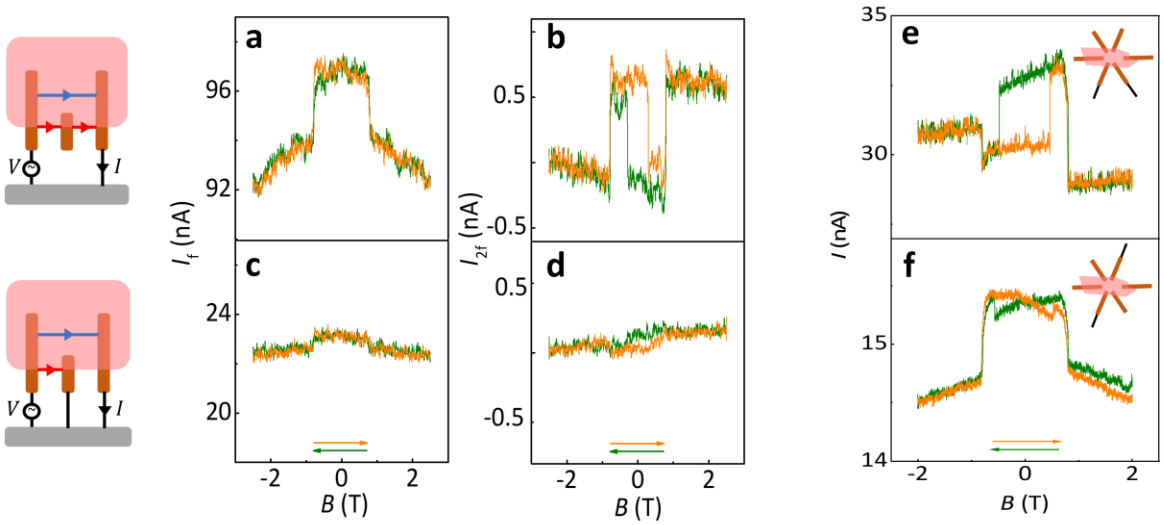

Figure 4.9. Evidence that the magnetic coupling is to the helical edge states. **a-d**, The first harmonic (**a** and **c**) and the second harmonic (**b** and **d**) responses as a function of out-of-plane magnetic field of 4-layer CrI_3 device CW8 at $V_g = 0.1$ V and $T = 27$ K. As shown on the left of panels **a** and **b**, the edge is floated for panels **a** and **b** and grounded for panels **c** and **d**. **e-f**, The current as a function of out-of-plane magnetic field at $V = 100$ mV d.c. bias of device CW5 at $T = 28$ K. The insets show the measurement configuration.

4.6 Inner jump of bilayer CrI_3

When B is swept from $+2.5$ T to -2.5 T, bilayer CrI_3 should transition from ↑↑ to one of the antiferromagnetic states and then to ↓↓. However, in bilayer CrI_3 device CW5, three jumps are observed between 25 K to 45 K. Figure 4.10 shows adjacent two-terminal measurement of monolayer WTe_2 at ± 100 mV d.c. bias, where asymmetry is due to the nonreciprocal effect. Besides the left and right jumps, an inner jump is visible at 28 K but absent at 22 K. The coercive fields of the three jumps are plotted as a function of T in Fig. 4.10e. At a critical temperature, the inner jump merges into one of the outer jumps.

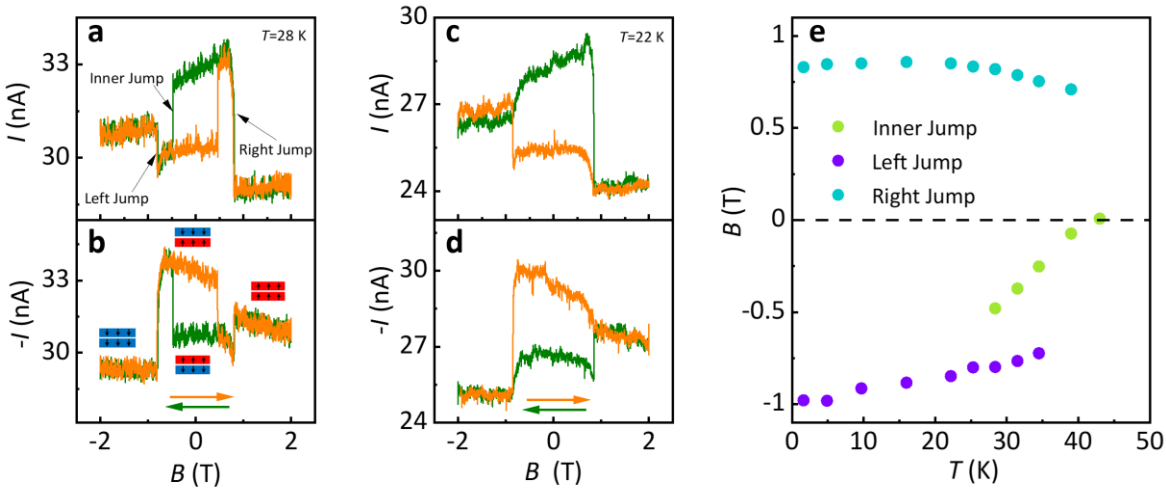

Figure 4.10. Inner jump of bilayer CrI_3 in device CW5. **a** and **b**, Two-terminal current as a function of B at $T = 28$ K for $+100$ mV and -100 mV d.c. bias. Schematic shows the corresponding magnetic states of bilayer CrI_3. **c** and **d**, Two-terminal current as a function of B at $T = 22$ K for $+100$ mV and -100 mV d.c. bias. **e**, Coercive field of the three jumps as a function of T.

RMCD measurements were done on the same device at a series of temperatures as shown in Fig. 4.11. It also shows two jumps at lower temperatures and three jumps at higher temperatures

when B is swept from $+2.5$ T to -2.5 T. In the antiferromagnetic state, if magnetization of the two layers compensate perfectly, the two states ($\uparrow\downarrow$ and $\downarrow\uparrow$) are degenerate. However, the symmetry of two layers CrI_3 can be easily broken by the fabrication process, especially in device CW5, where one side of bilayer CrI_3 is capped by hBN and the other by monolayer WTe_2. At lower temperature, bilayer CrI_3 transitions following $\uparrow\uparrow \Rightarrow \uparrow\downarrow \Rightarrow \downarrow\downarrow$ as B is swept from $+2.5$ T to -2.5 T. At higher temperature, it instead transitions following $\uparrow\uparrow \Rightarrow \uparrow\downarrow \Rightarrow \downarrow\uparrow \Rightarrow \downarrow\downarrow$.

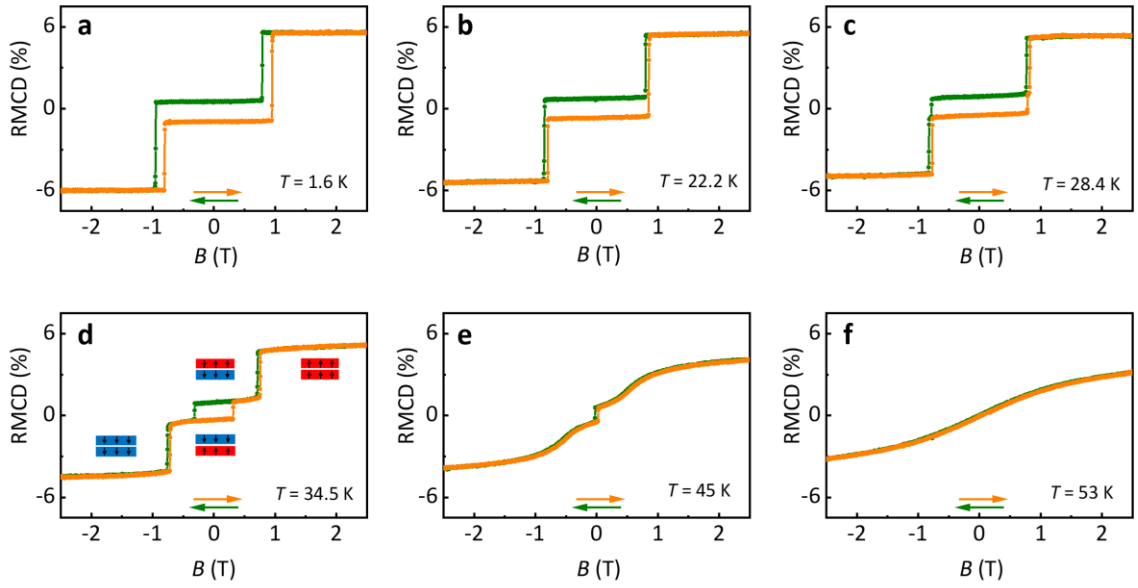

Figure 4.11. Temperature dependence of RMCD traces. **a-f**, RMCD signal as a function of an out-of-plane magnetic field for device CW6 (bilayer CrI_3) at different temperatures as indicated. Schematic shows the corresponding magnetic states of bilayer CrI_3.

4.7 Conclusion and future outlooks

In this chapter, we showed magnetic proximity control of topological (quantum spin Hall) edge conduction. The electrons in the WTe_2 edge states experience an magnetic exchange field of the order of 10 T that is determined by the magnetization of both the adjacent and the next nearest

CrI_3 layer. The exchange field opens a gap in the edge spectrum wherever the edge is adjacent to CrI_3. In nonlinear transport of the edge, we observed a nonreciprocal current flow (i.e., different resistances for opposite bias directions) that is controlled by the magnetization of the adjacent CrI_3 layer. Moreover, the nonreciprocal effect is orders of magnitude larger than observed elsewhere, such as in magnetically doped topological insulator surface states(*78*, *79*). This can be attributed to the special one-dimensional helical nature of the edge channel and the absence of parasitic bulk current flow.

In the future, using the van der Waals assembly techniques, the magnetic proximity effect can be studied in more systems, such as magnet/superconductor, magnet/topological insulator/magnet, and magnet/superconductor/topological insulator. In particular, the quantum anomalous Hall could be achieved by replacing monolayer WTe_2 by another quantum spin Hall insulator with a small inverted gap (*86*).

Chapter 5. Injecting spin current into monolayer WTe_2

In Chapter 3 we established the helical nature of quantum spin Hall state in monolayer WTe_2, where spin-momentum locking ensures that the spin of the left moving electron is polarized along one direction of the spin axis and that of the right moving electron is polarized in the opposite direction. A net electron current in the QSH edge should also be spin polarized. Then, a question that is crucial for spintronic device application is how injected spin current would propagate along the QSH edge. In the simplest theoretical model, if the injected spin current is fully polarized along one direction of the spin axis of the QSH edge, the spin current should flow along the direction determined by spin-momentum locking effect (*87*). In this chapter, we study monolayer WTe_2 devices with a spin current injection contact to try to demonstrate this.

5.1 2D magnet as a spin filter

The discovery of 2D magnets has not only enabled a novel avenue to study the magnetic proximity effect as discussed in Chapter 4, but also to study tunneling magnetoresistance (TMR). Quantum mechanics tells us electrons have the possibility to tunnel through an insulating barrier between two conducting parts. This tunneling effect has lots of applications, such as scanning tunneling microscopy. The tunneling rate is determined by the height of the tunneling barrier and the relative Fermi energy of two conducting parts. Using 2D materials, TMR can be achieved using in two device geometries: 1) conductor/2D magnetic insulator/conductor and 2) 2D magnetic conductor/insulator/2D magnetic conductor. The first structure utilizes the difference barrier heights of spin up and down states of 2D magnet insulators. The second structure utilizes the

increased difference between the lowest subbands for the same-spin states in the magnetic conductors when the magnets are magnetized antiparallel instead of parallel.

Figure 5.1 shows experimental results demonstrating each avenue for TMR, using structures comprising graphene/CrI_3/graphene (*66*, *88*) and Fe_3GeTe_2/hBN/Fe_3GeTe_2 (*89*). Giant TMR is observed in both experiments. The tunneling current and RMCD for graphite/bilayer CrI_3/graphite as a function of magnetic field are depicted in Fig. 5.1a. When bilayer CrI_3 is in an antiferromagnetic state, the tunneling barriers for both spin up and down electrons are relatively high which produces low tunneling current. After bilayer CrI_3 is changed to ferromagnetic state, for example ↑↑, by the applied magnetic field, the tunneling barrier is reduced for spin up and increased for spin down electrons. The net effect is higher tunneling current which mainly contains spin up electrons. This demonstrates that CrI_3 is a good spin filter in its ferromagnetic state.

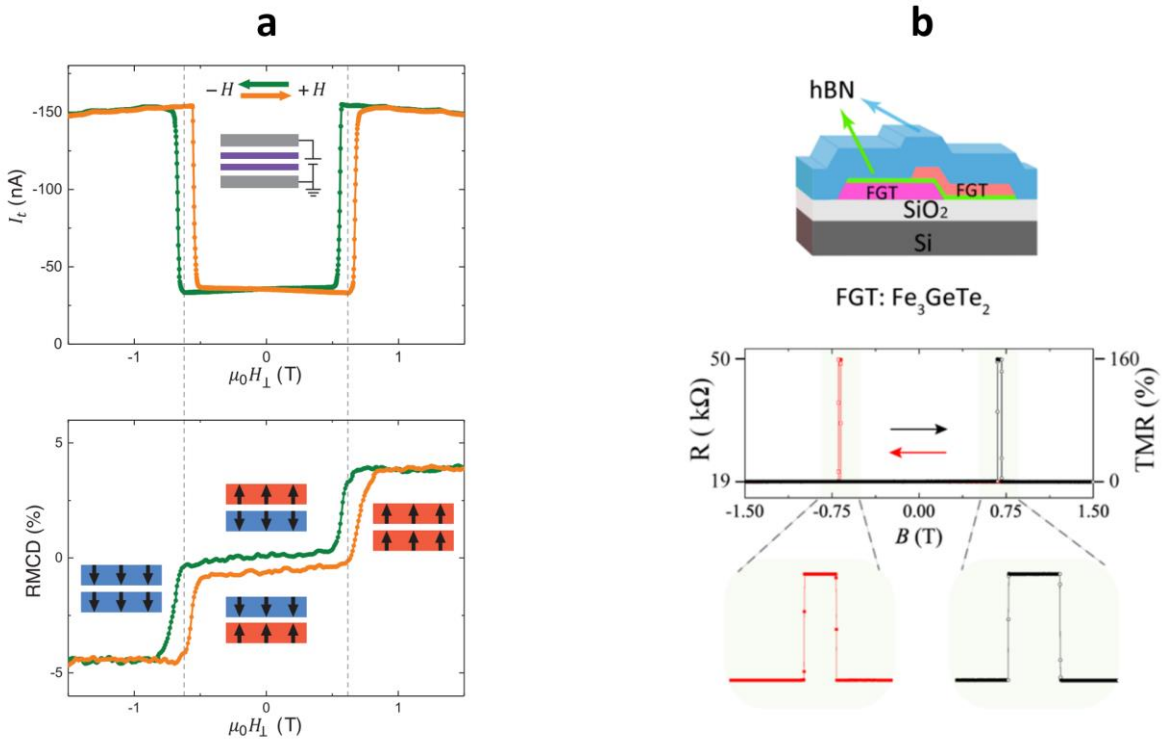

Figure 5. 1. Two realizations of tunneling magnetoresistance. **a**, Tunneling current (I_t) and reflective magnetic circular dichroism (RMCD) signal in graphite/bilayer CrI_3/graphite device as a function of

out-of-plane magnetic field. Four possible magnetic states of bilayer CrI_3 are labeled on the lower panel. **b**, Tunneling resistance in Fe_3GeTe_2/hBN/ Fe_3GeTe_2 device as a function of out-of-plane magnetic field. Device structure is drawn on the top. The zoom-in views of the vicinity when two Fe_3GeTe_2 contacts have different magnetization are shown on the bottom. (Panels **a** and **b** taken from Ref. (*66*) and Ref. (*89*), respectively)

The tunneling resistance for Fe_3GeTe_2/hBN/ Fe_3GeTe_2 is shown in Fig. 5.1b. Fe_3GeTe_2 is a 2D ferromagnetic metal below 200 K (*90*, *91*). When two Fe_3GeTe_2 contacts have opposite magnetization, the tunneling resistance is bigger because the difference between the lowest subbands for same-spin states on different contacts is bigger.

5.2 Tunneling measurements through a bilayer CrI_3 barrier

To inject spin current into monolayer WTe_2, we first made device CTW1, shown in Figure 5.2a. Besides two normal platinum contacts underneath the monolayer WTe_2, there is a center graphite contact on the top of monolayer and separated from the WTe_2 by a bilayer of CrI_3 and a bilayer of hBN, as shown schematically in Fig. 5.2b. The bilayer CrI_3 serves as a spin filter and the bilayer hBN reduces the magnetic coupling between the bilayer CrI_3 and the monolayer WTe_2.

$I-V$ traces were obtained at $T = 5.6$ K as shown in Fig. 5.2b. The bulk part of the monolayer WTe_2 was turned on by setting $V_g = 10$ V and it dominated the tunneling current. A d.c. bias V_{center} was applied on the center contact and the currents draining at the left contact (I_{left}) and right contact (I_{right}) were recorded simultaneously. The total tunneling current I_{t} is the sum of I_{left} and I_{right}. No current was detected below a threshold bias and it increased quickly past the threshold, indicating that a good tunneling barrier was formed by the bilayer CrI_3 and bilayer hBN. Another feature is that both the threshold and current depended strongly on the magnetization state

of the bilayer CrI_3. At 0 T, bilayer CrI_3 is at ↑↓ or ↓↑ state, where the arrows represent the magnetization of each layer and the tunneling barrier of bilayer CrI_3 for both spin up and down electrons is relatively high. At 1.5 T, the state of the bilayer CrI_3 changed to ↑↑. In this ferromagnetic state, the tunneling barrier for spin up electrons was reduced. Hence, the threshold of bias was lower and tunneling current was higher for ferromagnetic state of CrI_3.

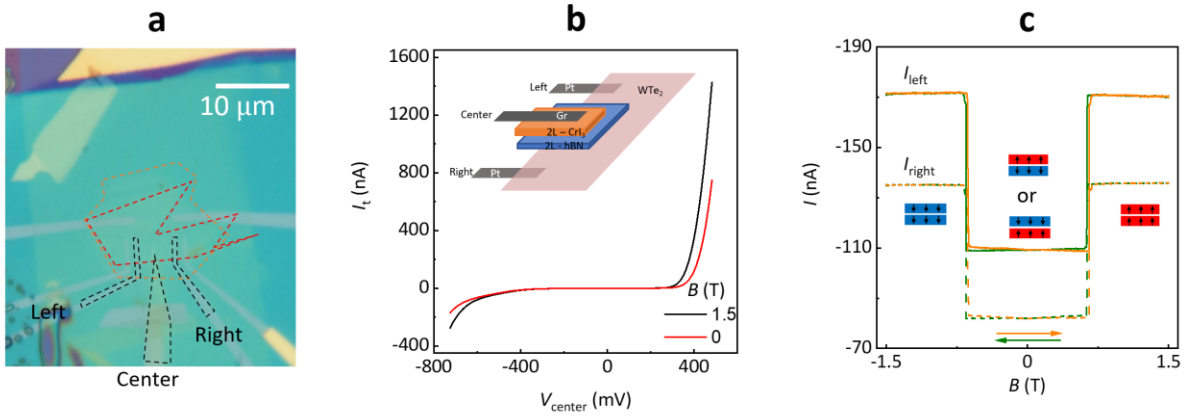

Figure 5. 2. Characterization of CTW1 device. **a**, Optical image of device CTW1. Left, center and right contacts are drawn by black dashed lines. The boundary of monolayer WTe_2 and bilayer CrI_3 are drawn by red and orange dashed lines, respectively. The edge length between the left to the center contact and the right to the center contact are about 1.7 μm and 2.5 μm, respectively. **b**, $I-V$ characteristics at $T = 5.6$ K and $V_g = 10$ V. Red and black traces are taken at $B = 0$ and 1.5 T. Inset shows the cartoon of device structure. **c**, Tunneling currents I_{left} (solid traces) and I_{right} (dashed traces) as a function of out-of-plane magnetic field at $T = 12$ K and $V_g = 10$ V. A -600 mV d.c. bias is applied on the center contact and currents drain at the left and the right contacts, which are recorded simultaneously. The magnetization states of bilayer CrI_3 are labeled by red and blue layers, where arrows show the direction of magnetization of each layer.

Next, the bias on the center contact was fixed at -600 mV. Due to both the left and the right contacts being grounded, tunneling current which is injected into monolayer WTe_2 should split to

two paths and drain at either the left or the right contact. Figure 5.2c shows I_{left} and I_{right} as a function of out-of-plane magnetic field B at $T = 12$ K and $V_g = 10$ V. The magnetization states of CrI_3 are labeled in the inset of Fig. 5.3c. Tunneling current should be strongly spin polarized up or down when CrI_3 is at ↑↑ or ↓↓ state, respectively. Both I_{left} and I_{right} were symmetric about $B = 0$, which indicates that the bulk of monolayer WTe_2 is insensitive to the sign of B and the spin polarization of the tunneling current. The ratio of $\frac{I_{\text{left}}}{I_{\text{right}}}$ is roughly equal to the ratio of the distances from the center to the right contact and to the left contact.

After verification of the quality of the tunneling contact, the gate voltage V_g was set to -2 V and the edge of monolayer WTe_2 should dominate the conductance. The bias on the center contact was again set at -600 mV and I_{left} and I_{right} were measured at the same time. The B dependence of I_{left} and I_{right} are shown in Fig. 5.3a. I_{left} is always higher I_{right} because the left contact is closer to the center contact than the right contact. One significant feature is that both I_{left} and I_{right} are asymmetric about $B = 0$. When B was higher than 0.8 T, the bilayer CrI_3 is polarized to the ↑↑ state and the tunneling current was highly spin up polarized. More current flowed to the left contact. When B became lower than -0.8 T, the magnetization state of the bilayer CrI_3 flipped to ↓↓ and the tunneling current was highly spin down polarized. Thus, more current flowed to the right contact. The current distribution function ρ is defined by $\frac{I_{\text{left}} - I_{\text{right}}}{I_{\text{left}} + I_{\text{right}}}$. As shown in Fig. 5.3b, ρ is also asymmetric about $B = 0$ and the difference at $+1.5$ T and -1.5 T is about 12%.

To prove that this asymmetric current distribution is rooted in edge transport, we measured $\Delta\rho$ at different V_g, where $\Delta\rho = \rho(+1.5\text{ T}) - \rho(-1.5\text{ T})$. First, the center contact was grounded and a 1 mV a.c. bias was applied between the left and the right contacts. The conductance $G_{\text{left-right}}$ between the left and the right contacts as a function of V_g is shown by the red trace in

Fig. 5.3c. The plateau region at low gate voltage indicates the edge of monolayer WTe_2 dominated $G_{\text{left-right}}$. Values of $\Delta\rho$ at select V_g are plotted by black dots with an error bar, which is the difference in the traces when sweeping B up vs down. It is clear that $\Delta\rho$ was much larger when the edge dominated $G_{\text{left-right}}$. Figure 5.3d plots the temperature dependence of $\Delta\rho$ at $V_g = -12, -2, 10$ V. When the monolayer WTe_2 was doped, $\Delta\rho$ was close to 0 down to 5 K. But when the edge dominated the conductance, $\Delta\rho$ increased monotonically with cooling down.

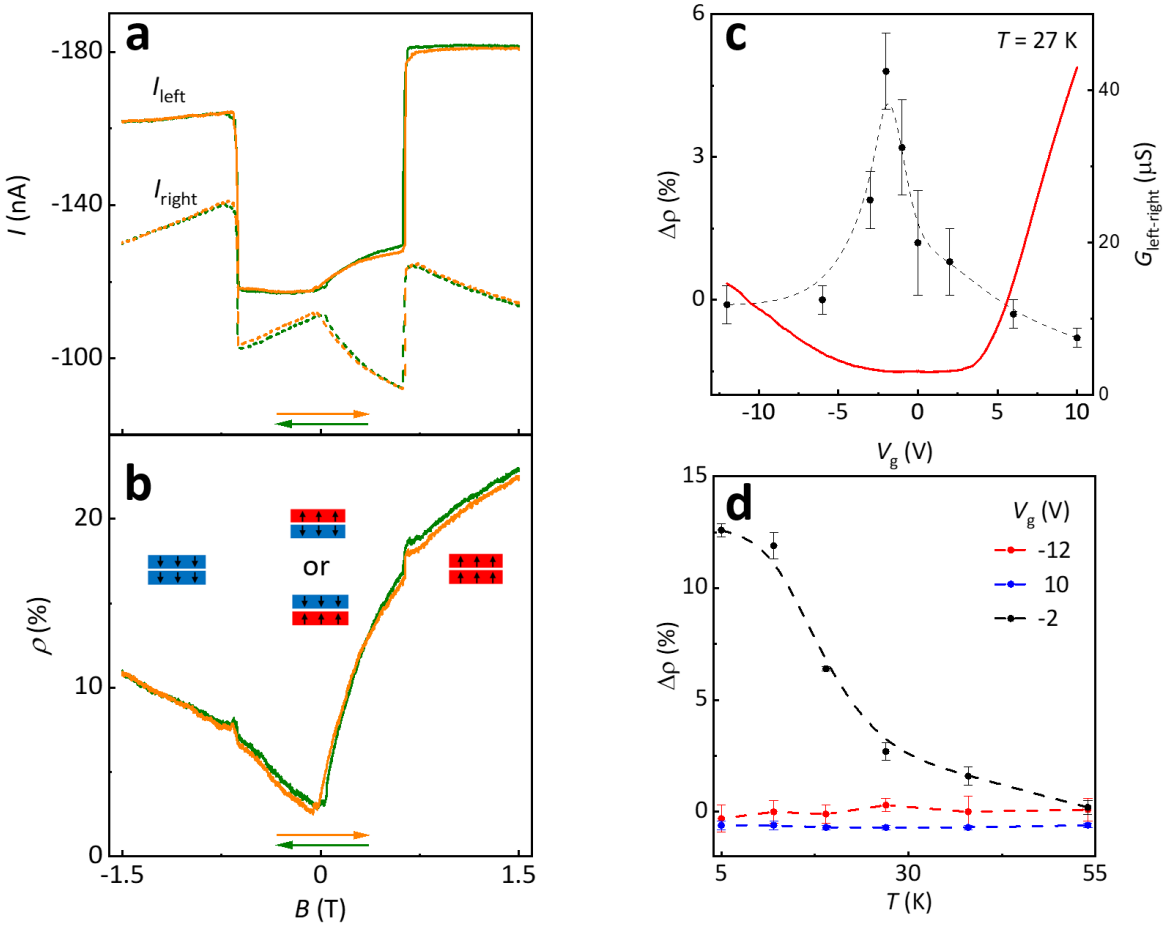

Figure 5. 3. Injecting spin polarized current into the edge of monolayer WTe_2. **a**, Tunneling current drained the left contact (I_{left}, solid traces) and the right contact (I_{right}, dashed traces) as a function of B at $V_g = -2\ V$ and $T = 12$ K. **b**, Current distribution parameter ρ calculated from panel **a** as a function of B . The magnetic state of bilayer CrI_3 is labelled in the inset. **c**, $\Delta\rho$ (black dots) and

$G_{\mathrm{left-right}}$ (red trace) as a function of V_g at $T = 27$ K. $G_{\mathrm{left-right}}$ is measured at $B = 0$ and with 1 mV a.c. bias applied between the left and the right contact. **d**, $\Delta\rho$ as a function of T at difference V_g.

In summary, in the edge-dominated regime, more tunneling current flows to the left contact when current is spin up polarized at $B > 0.8$ T. When both the sign of B and spin polarization of current reverse, more tunneling current flows to the right contact. This asymmetric current distribution affected by the sign of B and spin polarization of current has two possible origins. One is the nonlinear effect of the QSH edge itself which is related to the sign of B, as discussed in Section 3.6. The other is the spin selection effect of the QSH edge. When spin current is injected into monolayer WTe_2, it needs to be projected either the spin up or down state along the spin axis of monolayer WTe_2 ($\boldsymbol{d_{so}}$). Due to the spin-momentum locking effect, electrons with spin up must flow in one direction and electron with spin down flow in the other. Then the different spin polarization of injected current should have different probabilities to be projected on the spin up and down state of the edge, which can produce asymmetric current distribution.

5.3 Polarized spin current to the spin axis of monolayer WTe_2

Although asymmetric current distribution is observed by applying a constant bias at positive and negative out-of-plane magnetic field, it is still hard to tell whether it is dominated by the nonlinear effect of the edge itself or a spin polarized tunneling current. The anisotropy axis of CrI_3 is perpendicular to the 2D sheet, which is the z-axis. But the spin axis ($\boldsymbol{d_{so}}$) of monolayer WTe_2 has a $\sim 40°$ angle with the z-axis. In this section, I will discuss our experiment of aligning the magnetization of CrI_3 to $\boldsymbol{d_{so}}$ by a vector magnetic field.

The conductance between the left and the right contacts was measured first to find the y-z mirror plane of monolayer WTe_2. As discussed in Section 3.3, $G_{\mathrm{left-right}}$ is maximized when $\boldsymbol{B}$ is along $\boldsymbol{d_{so}}$. Figure 5.4a shows $G_{\mathrm{left-right}}$ as a function of φ at different temperatures and $V_g = 0$ V when $\boldsymbol{B}$ was rotated in the y-z plane, where θ is the polar angle between $\boldsymbol{B}$ and the x-axis and φ is the azimuthal angle relative to the z-axis. Anisotropy was very weak at 150 K due to the bulk of monolayer dominating the conductance. When the bulk of monolayer WTe_2 was frozen out below 100 K, anisotropy was stronger and $G_{\mathrm{left-right}}$ peaks at $\varphi_s = 38°$. Then φ was set to 90 ° where $\boldsymbol{B}$ was aligned with the y-axis to find when the magnetization of bilayer CrI_3 becomes fully polarized along $\boldsymbol{B}$. Figure 5.4b shows $I_{\mathrm{left}} + I_{\mathrm{right}}$ as a function of B at $T = 12$ K and $V_g = 10$ V. $I_{\mathrm{left}} + I_{\mathrm{right}}$ was the smallest at $B = 0$, at the antiferromagnetic state of the bilayer CrI_3, and increased smoothly with the magnitude of B. It changed slowly after the magnitude of B exceeds about 4.5 T. This behavior is consistent with Ref. (*66*) and can be explained by a spin-canting effect. Hence, bilayer CrI_3 magnetization became aligned with $\boldsymbol{B}$ when B exceeded 4.5 T.

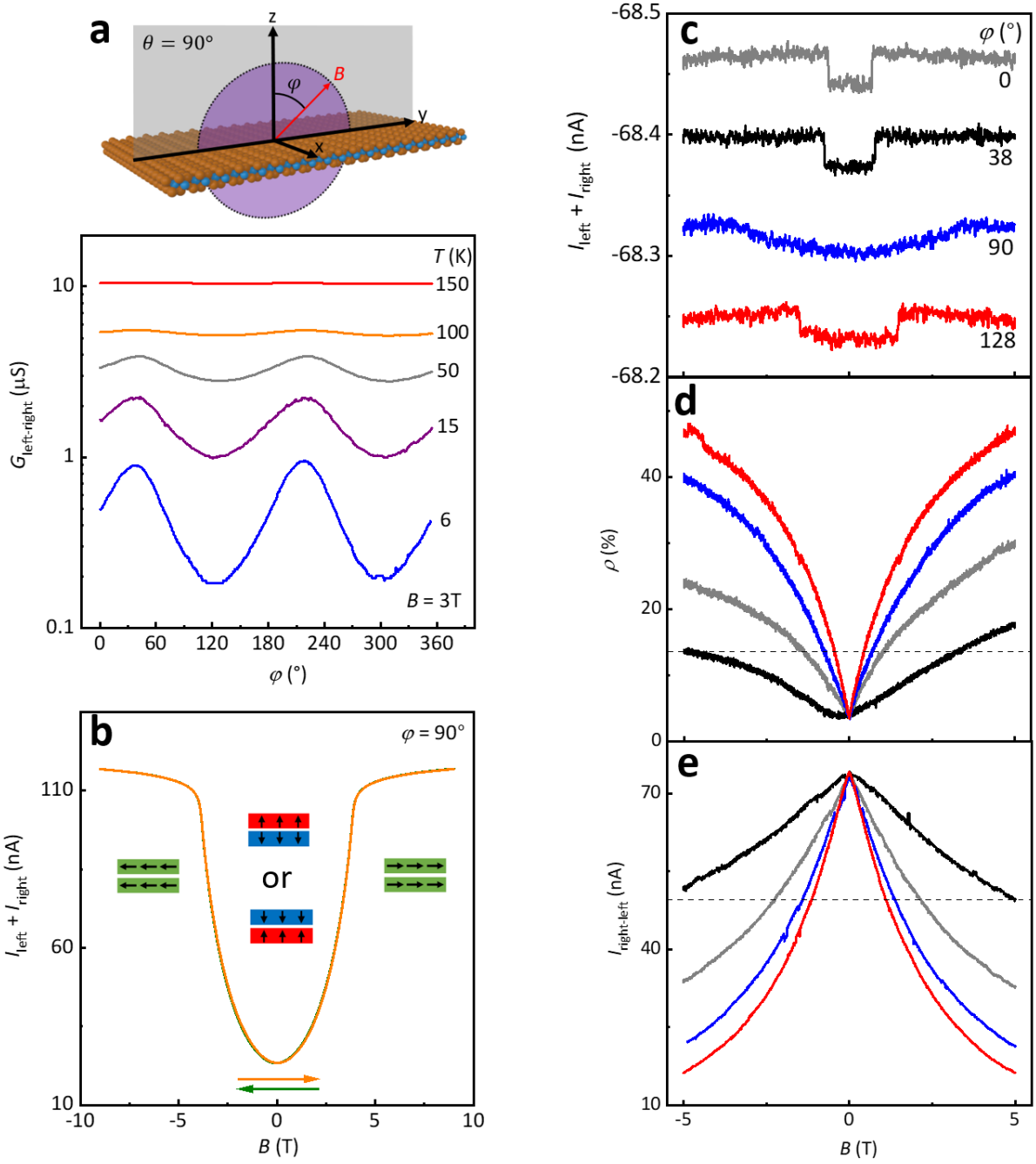

Figure 5. 4. Polarizing the magnetization of CrI_3 to $\boldsymbol{d_{so}}$. **a**. $G_{\text{left}-\text{right}}$ as a function of φ at different T at $B = 3$ T, $V_g = 0$ and $\theta = 90°$. Definition of θ and φ relative to crystal structure of monolayer WTe_2 is shown in the inset. Gray plane shows the y-z mirror plane. **b**, Total tunneling current $I_{\text{left}} + I_{\text{right}}$ as a function of B at $T = 12$ K, $V_g = 10V$, $\theta = 90°$ and $\varphi = 90°$. The inset shows the magnetization states of bilayer CrI_3. **c-e**, $I_{\text{left}} + I_{\text{right}}$ (panel **c**), current distribution function ρ (panel

d) and $I_{\text{right}-\text{left}}$ (panel **e**) as a function of B at $T = 12$ K and $V_g = 0$. The values of φ are labeled in (**c**) and the same color coding is used for (**d**) and (**e**). The dashed lines indicate the difference between positive and negative field. A -68 nA d.c. current source is used for (**c**) and (**d**). A 20 mV d.c. bias is applied on the right contact for (**e**).

Then a d.c. current source of about -68 nA, was applied on the center contact. Figure 5.4c plots $I_{\text{left}} + I_{\text{right}}$ as a function of B at different φ. Jumps, which happened at increasing magnitudes of B as $|\cos(\varphi)|$ decreased, are clearly seen when φ is not $90°$. The current distribution function ρ as a function of B at different φ is plotted in Fig. 5.4d. Clearly, ρ was asymmetric about $B = 0$ for $\varphi = 0°$ and $38°$. $\Delta\rho = \rho(+5\text{ T}) - \rho(-5\text{ T})$ was about 5.9% and 4% for $\varphi = 0°$ and 38°, respectively. Then the current from the right contact to the left contact as a function of B was directly measured by applying 20 mV d.c. bias on the right contact when V_{center} and V_g were set to 0. The magnitude of the current though the edge ($I_{\text{right}-\text{left}}$) was chosen to be comparable with the current used for Fig. 5.4c. As shown in Fig. 5.4e, $\frac{\Delta I}{I} = \frac{I_{\text{right}-\text{left}}(+5\text{ T}) - I_{\text{right}-\text{left}}(-5\text{ T})}{I_{\text{right}-\text{left}}(-5\text{ T})}$ was about -3.7% and -4%, which means that nonlinear effect of the QSH edge itself could have made current flowing from the right contact smaller than from the left contact to the part of monolayer WTe_2 under the center contact at positive magnetic field. This should have contributed a positive value to $\rho(+5\text{ T}) - \rho(-5\text{ T})$ because the current source had a negative value. $\Delta\rho$ had a similar value with $\frac{\Delta I}{I}$ at $\varphi = 38°$ and a bigger value than $\frac{\Delta I}{I}$ at $\varphi = 0°$, which indicates that the nonlinear effect of the QSH edge itself dominated the asymmetric current distribution.

5.4 Spin current injection from Fe_3GeTe_2 tunneling contact

The amount of current flow through the edge of monolayer WTe_2 needs to be decreased to the linear regime to eliminate the nonlinear effect. A potential solution is to replace the CrI_3/BN tunneling contact with Fe_3GeTe_2\hBN, where Fe_3GeTe_2 is a 2D ferromagnetic metal with an out-of-plane anisotropy axis (*90*, *91*).

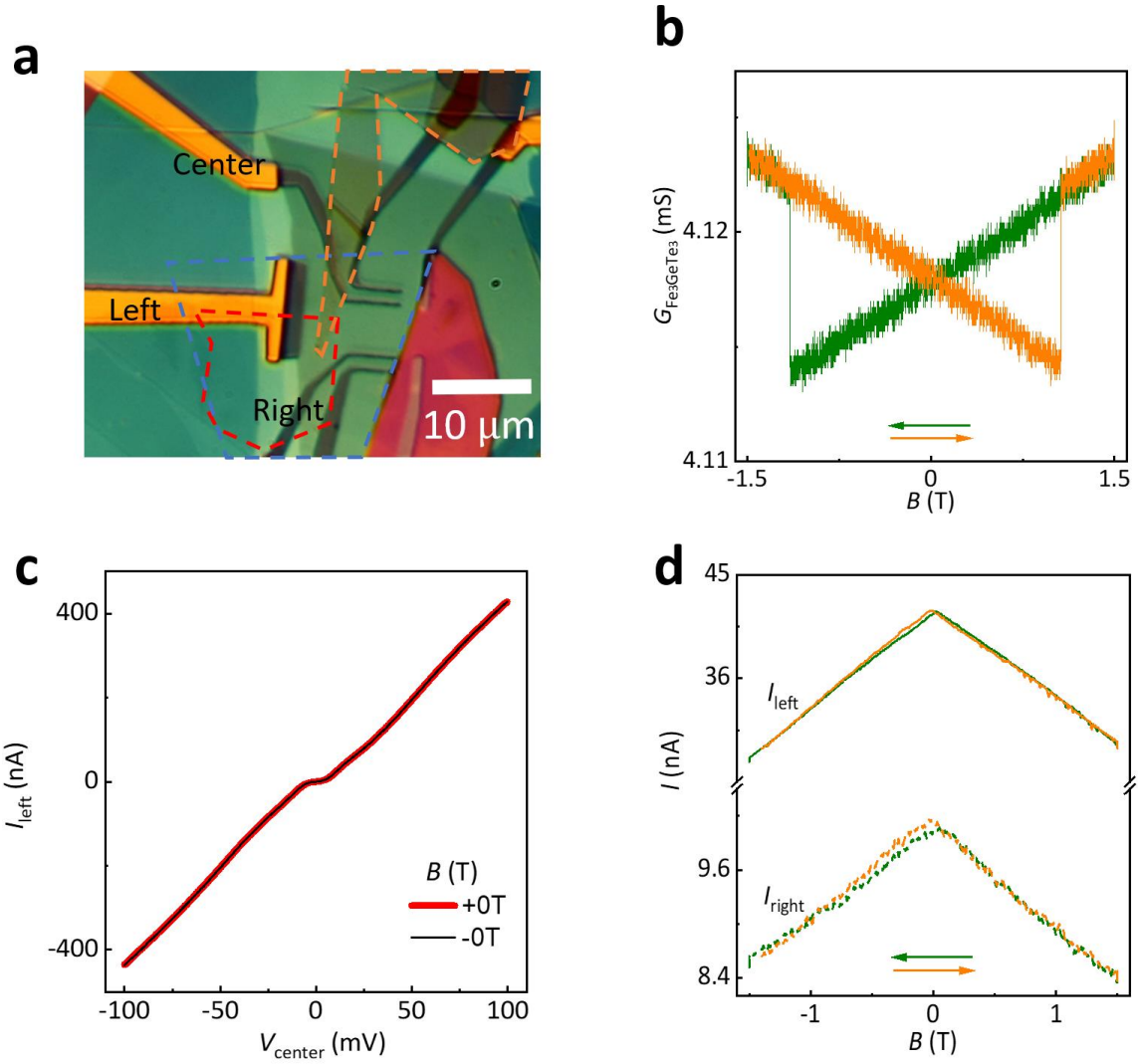

Figure 5.5. Fe_3GeTe_2 tunneling device CTW3. **a**, Optical microscope image of device CTW3. Fe_3GeTe_2, bilayer hBN and monolayer WTe_2 are outlined by orange, blue and red dashed lines, respectively. **b**, Conductance of Fe_3GeTe_2 ($G_{Fe_3GeTe_2}$) as a function of B at 5 K. **c**, $I_{left} - V_{center}$

characteristics at $T = 5$ K and $V_g = 0$. Inset shows $G_{Fe_3GeTe_2}$ as a function of B. **d**, I_{left} and I_{right} as a function of B at $T = 5$ K, $V_{\text{center}} = 15$ mV and $V_g = 0$.

Figure 5.5a shows the optical image of device CTW3 with two normal platinum contacts and one Fe_3GeTe_2 tunneling contact. Fe_3GeTe_2 which is outlined by orange dashed lines touches with the center contact and another two Pt contacts. The bilayer hBN, outlined by blue dashed lines, separates the Fe_3GeTe_2 from the monolayer WTe_2. Figure 5.5b shows the conductance of Fe_3GeTe_2 as a function of out-of-plane magnetic field at 5 K. The hysteresis feature shows that Fe_3GeTe_2 contact works as expected. Then V_{center} was applied to the center contact and current was measured at the left and the right contacts, simultaneously. I_{left} as a function of V_{center} where Fe_3GeTe_2 has two different magnetizations are shown in Fig. 5.5c. ± 0 T means B was reduced from ± 1.5 T to 0 T. Although the Fe_3GeTe_2 had opposite magnetization, the difference between the two $I - V$ traces cannot be resolved. I_{left} and I_{right} were also measured as functions of B at $T = 5$ K, $V_{\text{center}} = 15$ mV and $V_g = 0$, as shown in Fig. 5.5d. A small asymmetric feature can be explained by the nonlinear effect of the QSH edge itself.

5.5 Conclusion and future outlooks

Measurements of monolayer WTe_2 devices with one tunneling contact were discussed in this chapter. Different asymmetric current distributions were observed at positive and negative magnetic field. After carefully studying the contribution of the nonlinear effect of the QSH edge itself and the spin selection effect of the QSH edge, we conclude that the first effect dominates the current distribution.

There are several possibilities to explain why spin selection effect remains unresolved. First, the tunneling electrons enter at high energy and can lose their spin polarization while relaxing. Second, the spin-orbit coupling is too strong for monolayer WTe_2 which can mess up spin transport. Third, tunneling could happen between the tunneling contact and the monolayer WTe_2 bulk; the current then flows from the bulk to the edge, which can cause loss of spin polarization.

To prove that the current along the QSH edge is fully spin polarized, another device geometry should be employed. One possible geometry is demonstrated in Ref. (*92*) where they study spin-momentum locking in three-dimensional topological insulators. A chemical potential difference between spin up and down states can be generated by the injection of spin current. Instead of making spin current flow along the QSH edge, a drain contact can be fabricated just below the tunneling junction. Then, the two QSH edges are used as spin selective potential sensors.

Bibliography

1. K. S. Novoselov et al., Electric field effect in atomically thin carbon films. *Science* **306**, 666–669 (2004).
2. K. S. Novoselov et al., Two-dimensional gas of massless Dirac fermions in graphene. *Nature* **438**, 197–200 (2005).
3. Y. Zhang et al., Experimental observation of the quantum Hall effect and Berry's phase in graphene. *Nature* **438**, 201–204 (2005).
4. K. I. Bolotin et al., Observation of the fractional quantum Hall effect in graphene. *Nature* **462**, 196–199 (2009).
5. A. H. C. Neto et al., The electronic properties of graphene. *Rev. Mod. Phys.* **81**, 109-162 (2009).
6. Y. Oreg, Graphene.
7. Y. Cao et al, Correlated insulator behaviour at half-filling in magic-angle graphene superlattices. *Nature* **556**, 80–84 (2018).
8. Y. Cao et al, Unconventional superconductivity in magic-angle graphene superlattices. *Nature* **556**, 43–50 (2018).
9. T. V. Ramakrishnan, Nobel Prize in Physics 2016. *Resonance*. **22**, 781–785 (2017).
10. K. V. Klitzing et al, New method for high-accuracy determination of the fine-structure constant based on quantized Hall resistance. *Phys. Rev. Lett.* **45**, 494–497 (1980).
11. M. Berry, Quantal phase factors accompanying adiabatic changes. *Proc. R. Soc. Lond. A* **392**, 45–57 (1984).
12. D. J. Thouless et al., Quantized Hall conductance in a two-dimensional periodic potential.

Phys. Rev. Lett. **49**, 405–408 (1982).

13. M. Sato and Y. Ando, Topological superconductors: A review. *Rep. Prog. Phys.* **80** (2017).
14. C. L. Kane and E. J. Mele, Quantum spin Hall effect in graphene. *Phys. Rev. Lett.* **95**, 226801 (2005).
15. C. L. Kane and E. J. Mele, Z_2 topological order and the quantum spin Hall effect. *Phys. Rev. Lett.* **95**, 146802 (2005).
16. M. N. Ali et al., Large, non-saturating magnetoresistance in WTe_2. *Nature* **514**, 205–208 (2014).
17. A. A. Soluyanov et al., Type-II Weyl semimetals. *Nature* **527**, 495–498 (2015).
18. D. MacNeill et al., Control of spin-orbit torques through crystal symmetry in WTe_2 /ferromagnet bilayers. *Nat. Phys.* **13**, 300–305 (2017).
19. Q. Ma et al., Observation of the nonlinear Hall effect under time-reversal-symmetric conditions. *Nature* **565**, 337-342 (2019).
20. K. Kang et al., Nonlinear anomalous Hall effect in few-layer WTe_2. *Nat. Mater.* **18**, 324–328 (2019).
21. Z. Fei et al., Ferroelectric switching of a two-dimensional metal. *Nature* **560**, 336-339 (2018).
22. Z. Fei et al., Edge conduction in monolayer WTe_2. *Nat. Phys.* **13**, 677–682 (2017).
23. S. Tang et al., Quantum spin Hall state in monolayer 1T'-WTe_2. *Nat. Phys.* **13**, 683–687 (2017).
24. S. Wu et al., Observation of the quantum spin Hall effect up to 100 kelvin in a monolayer crystal. *Science* **359**, 76–79 (2018).

25. W. Zhao et al., Magnetic proximity and nonreciprocal current switching in a monolayer WTe_2 helical edge. *Nat. Mater.* **19**, 503-507 (2020).

26. E. Sajadi et al., Gate-induced superconductivity in a monolayer topological insulator. *Science* **362**, 922–925 (2018).

27. V. Fatemi et al., Electrically tunable low-density superconductivity in a monolayer topological insulator. *Science* **362**, 926–929 (2018).

28. M. Dawber et al., Physics of thin-film ferroelectric oxides. *Rev. Mod. Phys.* **77**, 1083–1130 (2005).

29. J. F. Scott, Applications of modern ferroelectrics. *Science* **315**, 954–959 (2007).

30. P. W. Anderson and E. I. Blount, Symmetry considerations on martensitic transformations: "ferroelectric" metals? *Phys. Rev. Lett.* **14**, 217-219 (1965).

31. Y. Shi et al., A ferroelectric-like structural transition in a metal. *Nat. Mater.* **12**, 1024–1027 (2013).

32. N. A. Benedek and T. Birol, "Ferroelectric" metals reexamined: fundamental mechanisms and design considerations for new materials. *J. Mater. Chem. C* **4**, 4000–4015 (2016).

33. T. H. Kim et al., Polar metals by geometric design. *Nature* **533**, 68–72 (2016).

34. H. Sakai et al., Critical enhancement of thermopower in a chemically tuned polar semimetal $MoTe_2$. *Sci. Adv.* **2**, e1601378 (2016).

35. Y. Wu et al., Temperature-induced Lifshitz transition in WTe_2. *Phys. Rev. Lett.* **115**, 166602 (2015).

36. P. J. Zomer et al., Fast pick up technique for high quality heterostructures of bilayer graphene and hexagonal boron nitride. *Appl. Phys. Lett.* **105**, 013101 (2014).

37. C. R. Dean et al., Boron nitride substrates for high-quality graphene electronics. *Nat.*

Nanotechnol. **5**, 722–726 (2010).

38. V. Fatemi et al., Magnetoresistance and quantum oscillations of an electrostatically tuned semimetal-to-metal transition in ultrathin WTe_2. *Phys. Rev. B* **95**, 041410(R) (2017).

39. P. Sharma et al., A room-temperature ferroelectric semimetal. *Sci. Adv.* **5**, eaax5080 (2019).

40. Q. Yang et al., Origin of two-dimensional vertical ferroelectricity in WTe_2 bilayer and multilayer. *J. Phys. Chem. Lett.* **9**, 7160–7164 (2018).

41. F. D. M. Haldane, Model for a quantum Hall effect without Landau levels: condensed-matter realization of the "parity anomaly". *Phys. Rev. Lett.* **61**, 2015–2018 (1988).

42. B. A. Bernevig et al., Quantum spin Hall effect and topological phase transition in HgTe quantum wells. *Science* **314**, 1757–1761 (2006).

43. M. König et al., Quantum spin Hall insulator state in HgTe quantum wells. *Science* **318**, 766–770 (2007).

44. I. Knez et al., Evidence for helical edge modes in inverted InAs/GaSb quantum wells. *Phys. Rev. Lett.* **107**, 136603 (2011).

45. X. Qian et al., Quantum spin Hall effect in two-dimensional transition metal dichalcogenides. **346**, 1344–1347 (2014).

46. F. Lüpke et al., Proximity-induced superconducting gap in the quantum spin Hall edge state of monolayer WTe_2. *Nat. Phys.* **16**, 526–530 (2020).

47. Y. Shi et al., Imaging quantum spin Hall edges in monolayer WTe_2. *Sci. Adv.* **5**, eaat8799 (2019).

48. L. Peng et al., Observation of topological states residing at step edges of WTe_2. *Nat. Commun.* **8**, 659 (2017).

49. M. Kim et al., Determination of the thickness and orientation of few-layer tungsten ditelluride using polarized Raman spectroscopy. *2D Mater.* **3**, 034004 (2016).

50. S. Ok et al., Custodial glide symmetry of quantum spin Hall edge modes in monolayer WTe_2. *Phys. Rev. B* **99**, 121105(R) (2019).

51. L. Muechler et al., Topological nonsymmorphic metals from band inversion. *Phys. Rev. X.* **6**, 041069 (2016).

52. L. Shi and J. C. W. Song, Symmetry, spin-texture, and tunable quantum geometry in a WTe_2 monolayer. *Phys. Rev. B* **99**, 035403 (2019).

53. Y.-M. Xie et al., Spin-orbit-parity coupled superconductivity in topological monolayer WTe_2. *arXiv*, 2005.08007 (2020).

54. J. H. Garcia et al., Canted spin texture and quantum spin Hall effect in WTe_2, *arXiv*, 2007.05626 (2020).

55. A. Arora et al., Cooperative orbital moments and edge magnetoresistance in monolayer WTe_2. *arXiv*, 2005.08986 (2020).

56. D. H. Choe et al., Understanding topological phase transition in monolayer transition metal dichalcogenides. *Phys. Rev. B* **93**, 125109 (2016).

57. X. Lin and J. Ni, Topological phase transition due to strain-controlled evolution of the inverted bands in 1*T′*-MX_2. *Phys. Rev. B* **95**, 245436 (2017).

58. A. Lau et al., Influence of lattice termination on the edge states of the quantum spin Hall insulator monolayer 1*T′*-WTe_2. *Phys. Rev. Mater.* **3**, 054206 (2019).

59. P. He et al., Bilinear magnetoelectric resistance as a probe of three-dimensional spin texture in topological surface states. *Nat. Phys.* **14**, 495-599 (2018).

60. Y. Tokura and N. Nagaosa, Nonreciprocal responses from non-centrosymmetric quantum

materials. *Nat. Commun.* **9**, 3740(2018).

61. Y.-B. Choi et al., Evidence of higher order topology in multilayer WTe_2 from Josephson coupling through anisotropic hinge states. *Nat. Mater*. (2020).

62. A. Kononov et al., One-dimensional edge transport in few-layer WTe_2. *Nano Lett.* **20**, 4228–4233 (2020).

63. C. Huang et al., Edge superconductivity in multilayer WTe_2 Josephson junction. *Natl. Sci. Rev.*, nwaa114 (2020).

64. C.-Z. Chang et al., Experimental observation of the quantum anomalous Hall effect in a magnetic topological insulator. *Science* **340**, 167–170 (2013).

65. B. Huang et al., Layer-dependent ferromagnetism in a van der Waals crystal down to the monolayer limit. *Nature* **546**, 270–273 (2017).

66. T. Song et al., Giant tunneling magnetoresistance in spin-filter van der Waals heterostructures. *Science* **360**, 1214-1218 (2018).

67. F. Hellman et al., Interface-induced phenomena in magnetism. **89**, 025006 (2017).

68. P. Wei et al., Exchange-coupling-induced symmetry breaking in topological insulators. *Phys. Rev. Lett*. **110**, 186807 (2013).

69. F. Katmis et al., A higherature ferromagnetic topological insulating phase by proximity coupling. *Nature*. **533**, 513–516 (2016).

70. P. Wei et al., Strong interfacial exchange field in the graphene/EuS heterostructure. *Nat. Mater.* **15**, 711-716 (2016).

71. C. Gong et al., Discovery of intrinsic ferromagnetism in two-dimensional van der Waals crystals. *Nature* **546**, 265–269 (2017).

72. C. Gong and X. Zhang, Two-dimensional magnetic crystals and emergent heterostructure

devices. *Science* **363**, eaav4550 (2019).

73. D. Zhong et al., Van der Waals engineering of ferromagnetic semiconductor heterostructures for spin and valleytronics. *Sci. Adv.* **3**, e1603113 (2017).

74. K. L. Seyler et al., Valley manipulation by optically tuning the magnetic proximity effect in WSe_2/CrI_3 heterostructures. *Nano lett.* **18**, 3823-3228 (2018).

75. D. Zhong et al., Layer-resolved magnetic proximity effect in van der Waals heterostructures. *Nat. Nanotechnol.* **15**, 187–191 (2020).

76. Y. Deng et al., Quantum anomalous Hall effect in intrinsic magnetic topological insulator $MnBi_2Te_4$. *Science* **367**, 895-900 (2020).

77. C. Liu et al., Robust axion insulator and Chern insulator phases in a two-dimensional antiferromagnetic topological insulator. *Nat. Mater.* **19**, 522–527 (2020).

78. K. Yasuda et al., Large unidirectional magnetoresistance in a magnetic topological insulator. *Phy. Rev. Lett.* **117**, 127202 (2016).

79. Y. Fan et al., Unidirectional magneto-resistance in modulation-doped magnetic topological insulators. *Nano Lett.* **19**, 692–698 (2019).

80. Y. Lv et al., Unidirectional spin-Hall and Rashba-Edelstein magnetoresistance in topological insulator-ferromagnet layer heterostructures. *Nat. Commun.* **9**, 111 (2018).

81. C. Liu et al., The quantum anomalous Hall effect : theory and experiment. *Annu. Rev. Condens. Matter Phys.* **7**, 301–321 (2016).

82. L. Liu et al., Spin-torque switching with the giant spin hall effect of tantalum. *Science* **336**, 555–558 (2012).

83. L. Fu and C. L. Kane, Josephson current and noise at a superconductor/quantum-spin-Hall-insulator/superconductor junction. *Phys. Rev. B* **79**, 161408(R) (2009).

84. B. Huang et al., Electrical control of 2D magnetism in bilayer CrI_3. *Nat. Nanotechnol.* **13**, 544-548 (2018).

85. S. Jiang et al., Controlling magnetism in 2D CrI_3 by electrostatic doping. *Nat. Nanotechnol.* **13**, 549-553 (2018).

86. C.-Z. Chang, Marriage of topology and magnetism. *Nat. Mater.* **19**, 484–485 (2020).

87. C. Brüne et al., Spin polarization of the quantum spin Hall edge states. *Nat. Phys.* **8**, 485–490 (2012).

88. D. R. Klein et al., Probing magnetism in 2D van der Waals crystalline insulators via electron tunneling. *Science* **360**, 1218–1222 (2018).

89. Z. Wang et al, Tunneling spin valves based on Fe_3GeTe_2 /hBN/ Fe_3GeTe_2 van der Waals Heterostructures. *Nano Lett.* **18**, 4303-4308 (2018).

90. Y. Deng et al., Gate-tunable room-temperature ferromagnetism in two-dimensional Fe_3GeTe_2. *Nature* **563**, 94-99 (2018).

91. Z. Fei et al., Two-dimensional itinerant ferromagnetism in atomically thin Fe_3GeTe_2. *Nat. Mater.* **17**, 778-782 (2018).

92. L. Liu et al., Spin-polarized tunneling study of spin-momentum locking in topological insulators. *Phys. Rev. B* **91**, 235437 (2015).